ALGERIAN PEOPLE'S DEMOCRATIC REPUBLIC

MINISTRY OF HIGHER EDUCATION AND SCIENTIFIC RESEARCH

MOHAMED BOUDIAF UNIVERSITY - M'sila

FACULTY OF SCIENCES

PHYSICS DEPARTEMENT

Order N°:

THESIS

To obtain the degree of:

Sciences DOCTORATE

Field: Physics

Option: Physics of Materials

Presented by:

ZIKEM Afifa

Theme

Contribution to the study of the physical properties of some double perovskite crystals via first principles methods

On 10/ 10/ 2024, with the board of examiners:

MAIRECHE Abdelmadjid	Professor	U. M'sila	President
BAAZIZ Hakim	Professor	U. M'sila	Supervisor
CHARIFI Zoulikha	Professor	U. M'sila	Co-supervisor
SENGOUGA Nouredine	Professor	U. Biskra	Examiner
MEFTAH Afak	Professor	U. Biskra	Examiner
BENNACER Badis	Professor	U. Guelma	Examiner
GHELLAB Torkia	MCA	U. M'sila	Invited

Acknowledgements

This research was conducted at "The laboratory of physics and chemistry of materials" in the Faculty of Sciences of Mohamed Boudiaf University of M'sila. I would like to express my sincerest thanks to everyone who has supported and accompanied me throughout this project.

First and foremost, I deeply thank Professor BAAZIZ Hakim and Professor CHARIFI Zoulikha, my two thesis supervisors who agreed to direct this study and who have shared their experiences and advice with me throughout this work. May they find here all the expression of my gratitude for their respective scientific and human support.

I express my recognition to Professor MAIRECHE Abdelmadjid , who kindly agreed to preside over the jury of this thesis. I would also like to thank all the members of the jury for having accepted to examine my research work: Professors SENGOUGA Nouredine, MEFTAH Afak, BENNACER Badis, and GHELLAB Torkia.

I am infinitely grateful to Mr SOYALP Fethi, from the Theoretical Physics Research Laboratory of the Faculty of Education in Turkey , for the considerable computing resources he has provided to me.

My sincere thanks go to my parents, my husband and my children, who supported me without fail. Without them, I would never have been able to complete my thesis.

Dedications

To Ahmed and Zineb my dear parents

To Smail my husband

To Younes, Abderrahmen, Akram, Ryadh my children

Abstract

Currently, there is significant interest in finding efficient materials with favorable optoelectronic and thermoelectric properties for power generation.

This study employs first-principles computations to investigate the structural, thermodynamic, optoelectronic, and thermoelectric characteristics of potassium tin halide vacancy-ordered double perovskites K_2SnX_6 (X = Cl, Br, I). Using the density functional theory (DFT) method and Boltzmann transport theory, we conduct a thorough analysis. We utilize the Perdew-Burke-Ernzerhof functional for bulk solids and their surface for generalized gradient approximation (PBESol- GGA) with and without the mBJ correction, employing a LAPW base-set.

Our electronic analysis indicates that the electronic band structures depicts direct band gaps for K_2SnCl_6 and K_2SnBr_6, while K_2SnI_6 exhibits an indirect band gap., with band gaps ranging from 1.70 eV to 4.126 eV (utilizing PBESol-mBJGGA), suggesting their potential for solar cells and optoelectronic applications.

Analysis of dielectric functions, absorption coefficients, and refractive indices calculations of the investigated compounds show excellent agreement with theoretical band gaps, validating their precise prediction. K_2SnI_6 demonstrates superior light absorption in the visible range compared to K_2SnCl_6, owing to its narrower band gap, rendering it suitable for solar cells. Refractive index analysis further confirms their applicability for solar applications.

Thermoelectric properties, including electronic and lattice thermal conductivities, Seebeck coefficients, and power factors, are evaluated. The studied compounds exhibit p-type conductivity, and their power factor values indicate promise as efficient thermoelectric materials. At 500 K, maximum ZT values of 0.58, 0.69, and 0.65 are achieved for K_2SnCl_6, K_2SnBr_6, and K_2SnI_6, respectively.

These results underscore the promise of these materials for use in solar cells and thermoelectric devices, particularly noting their efficacy even under high-temperature conditions.

Keywords: Vacancy ordered double perovskites; Solar cell; Figure of merit; Seebeck coefficient; Power factor.

Resumé

Actuellement, il existe un intérêt considérable à la recherche des matériaux avec des propriétés optoélectroniques et thermoelectriques favorables pour la production de l'énergie.

Cette étude utilise des calculs de premiers principes pour étudier les caractéristiques structurales, thermodynamiques, optoélectroniques et thermoelectriques des double pérovskites ordonnées par des lacunes de potassium étain halogénure K_2SnX_6 (X= Cl, Br, I). En utilisant la méthode de la théorie de la fonctionnelle de la densité (DFT) et la théorie du transport de Boltzmann, nous menons une analyse approfondie. Nous utilisons la fonctionelle de Perdew-Burke-Ernzerhof et l'approximation de gradient généralisé (PBEsol-GGA) avec et sans la correction mBJ, en employant l'ensemble de base LAPW.

Notre analyse électronique indique que les structures de bandes électroniques étudiées révèlent des gaps directes pour K_2SnCl_6 et K_2SnBr_6, tandis que K_2SnI_6 présente un gap énergétique indirecte, avec des bandes interdites de largeurs allant de 1,70 eV à 4,126 eV (en utilisant PBESol-mBJGGA), suggérant leur potentiel pour les cellules solaires ainsi que pour d'autres applications optoélectroniques.

L'analyse des fonctions diélectriques, des coefficients d'absorption et des calculs des indices de réfraction montre un excellent accord avec les gaps d'énergie théoriques, validant leur prédiction précise. En raison de son gap plus étroit, K_2SnI_6 démontre une absorption lumineuse supérieure dans la gamme visible par rapport à K_2SnCl_6, le rendant approprié pour les cellules solaires. L'analyse de l'indice de réfraction confirme leur applicabilité pour les applications solaires.

Les propriétés thermoélectriques, y compris la conductivité thermique électronique et celle du réseau, les coefficients de Seebeck et les facteurs de puissance, sont évaluées. Ces composés présentent une conductivité de type p, et leurs valeurs du facteur de merit indiquent un potentiel prometteur en tant que matériaux thermoélectriques efficaces. À 500 K, des valeurs maximales de ZT de 0,58, 0,69 et 0,65 sont obtenues pour K_2SnCl_6, K_2SnBr_6 et K_2SnI_6, respectivement.

Ces résultats montrent que les matériaux étudiés sont prometteurs pour une utilisation dans les cellules solaires et les dispositifs thermoélectriques, en notant en particulier leur efficacité même dans des conditions de haute température.

Mots clés : Pérovskites doubles ordonnées par lacunes; Cellule solaire; Figure de mérite; Coefficient de Seebeck; Facteur de puissance.

الملخص

في الوقت الحالي، هناك اهتمام كبير بالبحث عن مواد فعالة ذات خصائص بصرية-إلكترونية وحرارية مواتية لتوليد الطاقة. أثارت البيروفسكيتات المزدوجة المرتبة بالفجوات اهتماماً كبيراً في الأوساط البحثية بسبب إمكانية استخدامها كمواد امتصاص الضوء في خلايا الطاقة الشمسية البيروفسكيتية. ومع ذلك، لا يزال هناك نقص في الفهم الشامل لخصائصها المادية على المستوى الذري.

تستخدم هذه الدراسة طرق (Ab-initio) المعتمدة على طريقة الأمواج المستوية المتزايدة خطيا (FP-LAPW) لدراسة الخصائص البنيوية و الالكترونية والبصرية والحرارية و الديناميكية للبيروفسكيتات المزدوجة K_2SnX_6 (X= Cl, Br, I) باستخدام طريقة نظرية كثافة الدالة (DFT) و نظرية النقل لبولتزمان. نقوم بتنفيذ تحليل شامل نستخدم فيه التدرج المعمم (GGA)مع وبدون تعديل mBJ.

يشير تحليلنا الإلكتروني إلى أن الهياكل الإلكترونية (band structure) تكشف عن فجوات باند مباشرة لـ K_2SnCl_6 وK_2SnBr_6، بينما يظهر K_2SnI_6 فجوة باند غير مباشرة، مع فجوات باند تتراوح بين 1.70 إلكترون فولت إلى 4.126 إلكترون فولت باستخدام(PBESol-mBJGGA)، مما يشير إلى إمكانية استخدامها في الخلايا الشمسية والتطبيقات البصرية-الإلكترونية.

يظهر تحليل الدوال الكهروبصرية، ومعاملات الامتصاص، وحسابات معامل الانكسار اتفاقًا ممتازًا مع الفجوات الطاقوية النظرية، مما يؤكد التنبؤ الدقيق بها. يظهر K_2SnI_6 امتصاصًا للضوء متفوقًا في النطاق المرئي مقارنة بـK_2SnCl_6 ، نظرًا لأن لفجوة الطاقوية أضيقة لديه، مما يجعله مناسبًا للخلايا الشمسية.

قيمت الخصائص الكهروحرارية، بما في ذلك الناقلية الحرارية الإلكترونية والشبكية، ومعاملات سيبيك، ومعاملات القوة. يزيد استبدال اليود من القدرة الكهربائية، بينما يقل نقل الحرارة الفونونية مع ارتفاع الحرارة. تظهر هذه المركبات توصيلًا من نوع p، وتشير قيم معامل القوة ZT إلى الوعد كمواد حرارية-كهرو حرارية. فعالة. في درجة حرارة 500 كلفن، تتحقق قيم ZT القصوى لـ 0.58، 0.69، و 0.65 لـK_2SnCl_6 ، K_2SnBr_6، و K_2SnI_6 على التوالي.

تؤكد هذه النتائج أن المواد المدروسة واعدة للاستخدام في الخلايا الشمسية وأجهزة التحويل الحراري، مع الإشارة بشكل خاص إلى كفاءتها حتى في ظروف درجات الحرارة العالية.

كلمات مفتاحية : البيروفسكايتات المزدوجة المرتبة بالفراغات, الخلية الشمسية, معامل الجدارة, معامل سيبيك, عامل القدرة.

List of figures

List of tables

Contents

Chapter III : Density functional theory (DFT) and FP-LAPW method

Chapter IV : Results and discussion41

General introduction

General introduction

The scientists are actively exploring alternative power generation methods in response to the escalating global energy demand. While photovoltaic modules play a crucial role in harnessing renewable energy, there is a growing interest in the field of thermoelectricity as an efficient alternative power generation method. The quest for more efficient materials with suitable optoelectronic and thermoelectric characteristics holds significant promise.

In the field of optoelectronics, perovskite solar cells have garnered significant interest since 2009 due to their exceptional power conversion efficiency, affordability, and simple manufacturing techniques. **[1-4]**.

The popularity of hybrid organic-inorganic Pb-based halide perovskites, featuring the prototype $CH_3NH_3PbI_3$, has been increasing, with perovskite solar cells achieving a certified power conversion efficiency of 25.2%. However, two major challenges currently impede the commercialization of large-scale devices: material instability and the environmental toxicity associated with lead. **[5,6]**. Consequently, there is a notable research focus on exploring novel, stable, and lead-free perovskites **[7]**.

In 2014, Lee et al. conducted a study **[8]** highlighting the optical and electrical suitability of cesium tin (IV) iodide (Cs_2SnI_6) for photovoltaics, reigniting interest in the vacancy-ordered double perovskite family A_2BX_6. Cs_2SnI_6 possesses a direct optical gap of 1.3 eV, and Lee et al. demonstrated its application in constructing a solar cell with a 7.8% power conversion efficiency. Additionally, research by Chen et al. **[9]** emphasized the exceptional intrinsic and environmental stability, as well as long and balanced carrier-diffusion lengths of Cs_2TiBr_6 thin films, with a favorable bandgap of 1.8 eV. They reported an initial power conversion efficiency of 3.3% for Cs_2TiBr_6 thin films-based perovskite solar cells **[9].** Cs_2TeI_6 **[10]**, Cs_2PdBr_6 **[11],** and Cs_2TiBr_6 **[12]** are also recognized as potential perovskite materials due to their acceptable optical bandgaps and stability. However, the limited availability of cesium in the Earth's crust poses a drawback.

In the field of thermoelectronics, thermoelectric generators (TEGs) hold promise for extracting usable energy from diverse sources, including industrial operations, power production, and transportation systems. Extensive research has been conducted on various thermoelectric materials such as tin selenide **[13]**, chalcogenides **[14-16]**, Half-Heusler alloys **[17**,**18]**, Zintl phases **[19]**, perovskites **[20-22]**, and other materials **[23-25]**. The extensive industrial

application of these materials has been hindered by issues like as high working temperatures, cost per watt, and structural complexity, despite notable advancements in their efficiency..

Next, focus turns to halide perovskites, which have garnered attention because of their advantageous phononic and electronic transport characteristics **[26–28]**. Furthermore, theoretical investigations have demonstrated their robust Seebeck coefficients **[32]** and very low lattice thermal conductivity **[28–31]**. However, the challenges of lead toxicity and structural instabilities of $CsMX_3$ (M = Pb, Sn, and X = halide) in ambient air pose significant obstacles, limiting their commercial viability.

Recently, vacancy-ordered double perovskites with the formula A_2BX_6 have attracted considerable interest due to their numerous advantages over lead halide perovskites, including enhanced stability, scalability, and non-toxicity **[33]**. Their tunable band gaps, long carrier diffusion lengths, air stability **[34]**, and flat band structure **[35]** make them ideal candidates for efficient solar cells and thermoelectric power generation. Researchers have investigated specific compounds within the vacancy-ordered double perovskite family, such as: Cs_2GeCl/Br_6 **[36]**, Cs_2SnI_6, Rb_2SnI_6 **[37]**, K_2OsCl_6, K_2OsBr_6 **[38]**, and Cs_2NbI_6 **[39]**, reporting promising optoelectronic and thermoelectric capabilities based on experimental evidence or theoretical calculations.

For thermoelectric applications. Despite the existing comprehensive research, there is an unavoidable necessity for an enhanced comprehension of the factors influencing the figure of merit (ZT).

The present study underscores the ongoing dedication to advancing research and development in the progression of photovoltaic cells and thermoelectric materials, signalling a hopeful trajectory for the future of sustainable energy.

Regarding VODPs, defined by the formula A_2BX_6, their vacancy-ordered structure, stemming from the conventional perovskite archetype, provides substantial adjustability in composition, presenting opportunities to modify structural, compositional, and dynamic attributes. Elements like the halogen choice at the X-site, interactions with the B-site cation, and the orbital nature at the band edges collectively impact the band gap and optical characteristics of VODPs.

The thermoelectric and optoelectronic properties of the K_2SnX_6 (X=I, Br, and Cl) vacancy ordered double perovskite compounds, which fall under the K_2PtCl_6-type category, have not

been substantially investigated. When K_2SnBr_6 and K_2SnCl_6 were first described in 1970, very few studies had concentrated on their structural characteristics **[40, 41]**. Notably, neither theoretical nor experimental research has been done on the thermoelectric and associated uses of these substances. For the potassium tin halide vacancy-ordered double perovskites K_2SnX_6 (X=I, Br, and Cl), more research is therefore required.

By providing essential thermoelectric and optoelectronic parameters for vacancy-ordered double perovskites K_2SnX_6 (X=I, Br, and Cl), this work seeks to close this gap. Thermal conductivity, electrical conductivity, power factor (PF), figure of merit, dielectric function, absorption coefficient, reflectivity, refractive index, and optical conductivity are all included in this set of characteristics. Moreover, the full potential linearized technique based on density functional theory (DFT) and Boltzmann transport theory implemented in Wien2k code are used to determine a number of additional key parameters, including structural and thermal properties as well as band-related characteristics. The anticipated results of these calculations are expected to lay the foundation for extended research on K_2SnX_6 (X=I, Br, and Cl) perovskites, with the ultimate objective of fostering their future industrial applications.

The thesis is organized into four chapters: the initial chapter offers an overview of the fundamental physical effects exploited in the functioning of solar cells, thermoelectric generators, and hybrid systems. It also traces significant historical milestones in their development. Moreover, this first chapter discusses the properties of the materials which provides the best functioning solar cells or thermoelectric generators. In the second chapter, a comprehensive literature review is presented, providing insights into the structural, optoelectronic, and thermoelectric features of the studied compounds. Then, the first section of the third chapter delves into the theory of density functional theory (DFT), introducing the Kohn-Sham equations and discussing two widely recognized approximations for the exchange-correlation potential: local density approximation (LDA) and generalized gradient approximation (GGA). The latter part of the third chapter introduces the ab-initio method (FP-LAPW) and the Wien2k code. The fourth chapter is dedicated to showcasing and analyzing the obtained results concerning the structural, electronic, optical, thermoelectric, and thermodynamic properties of the K_2SnX_6 compounds (X= Cl, Br, I). Lastly, a comprehensive summary of the key findings is provided in the general conclusion.

References

[1] M. Cheng *Chuantian Zuo b,, Yongzhen Wu,, Zhongan Li, Baomin Xu, Yong Hua, Liming Ding.*, "Charge-transport layer engineering in perovskite solar cells," *Science Bulletin*, vol. 65, no. 15, pp. 1237–1241, Aug. 2020, doi: 10.1016/j.scib.2020.04.021.

[2] X. Jia, *Chuantian Zuo, Shuxia Tao , Kuan Sun, Yixin Zhao , Shangfeng Yang , Ming Cheng,, Mingkui Wang, Yongbo Yuan, Junliang Yang, Feng Gao, Guichuan Xing, Zhanhua Wei, Lijun Zhang, Hin-Lap Yip, Mingzhen Liu, Qing Shen, Longwei Yin, Liyuan Han, Shengzhong Liu, Lianzhou Wang, Jingshan Luo , Hairen Tan w, Zhiwen Jin x, Liming Ding* "CsPb(I Br1−)3 solar cells," *Science Bulletin*, vol. 64, no. 20, pp. 1532–1539, Oct. 2019, doi: 10.1016/j.scib.2019.08.017.

[3] A. Kojima, K. Teshima, Y. Shirai, and T. Miyasaka, "Organometal Halide Perovskites as Visible-Light Sensitizers for Photovoltaic Cells," *J. Am. Chem. Soc.*, vol. 131, no. 17, pp. 6050–6051, May 2009, doi: 10.1021/ja809598r.

[4] Yaoguang Rong, Yue Hu, Anyi Mei, Hairen Tan, Makhsud I. Saidaminov, Sang Il Seok, Michael D. McGehee, Edward H. Sargent, Hongwei Han "Challenges for commercializing perovskite solar cells," *Science*, vol. 361, no. 6408, p. eaat8235, Sep. 2018, doi: 10.1126/science.aat8235.

[5] Bertrand Philippe, Byung-Wook Park, Rebecka Lindblad, Johan Oscarsson, Sareh Ahmadi, Erik M. J. Johansson, and Hakan Rensmo, "Chemical and Electronic Structure Characterization of Lead Halide Perovskites and Stability Behavior under Different Exposures—A Photoelectron Spectroscopy Investigation," *Chem. Mater.*, vol. 27, no. 5, pp. 1720–1731, Mar. 2015, doi: 10.1021/acs.chemmater.5b00348.

[6] Yue-Yu Zhang , Shiyou Chen, Peng Xu, Hongjun Xiang, Xin-Gao Gong, Aron Walsh , Su-Huai Wei, "Intrinsic Instability of the Hybrid Halide Perovskite Semiconductor $CH_3NH_3PbI_3$ *," *Chinese Phys. Lett.*, vol. 35, no. 3, p. 036104, Mar. 2018, doi: 10.1088/0256-307X/35/3/036104.

[7] Ming-Gang Ju, Min Chen, Yuanyuan Zhou, Jun Dai, Liang Ma, Nitin P. Padture, and Xiao Cheng Zeng., "Toward Eco-friendly and Stable Perovskite Materials for Photovoltaics," *Joule*, vol. 2, no. 7, pp. 1231–1241, Jul. 2018, doi: 10.1016/j.joule.2018.04.026.

[8] Byunghong Lee, Constantinos C. Stoumpos, Nanjia Zhou, Feng Hao, Christos Malliakas, Chen-Yu Yeh, Tobin J. Marks, Mercouri G. Kanatzidis, and Robert P. H. Chang, "Air-Stable Molecular Semiconducting Iodosalts for Solar Cell Applications: Cs_2SnI_6 as a Hole

Conductor," *J. Am. Chem. Soc.*, vol. 136, no. 43, pp. 15379–15385, Oct. 2014, doi: 10.1021/ja508464w.

[9] M. Chen *et al.*, "Cesium Titanium(IV) Bromide Thin Films Based Stable Lead-free Perovskite Solar Cells," *Joule*, vol. 2, no. 3, pp. 558–570, Mar. 2018, doi: 10.1016/j.joule.2018.01.009.

[10] A. E. Maughan, A. M. Ganose, M. M. Bordelon, E. M. Miller, D. O. Scanlon, and J. R. Neilson, "Defect Tolerance to Intolerance in the Vacancy-Ordered Double Perovskite Semiconductors Cs_2SnI_6 and Cs_2TeI_6," *J. Am. Chem. Soc.*, vol. 138, no. 27, pp. 8453–8464, Jul. 2016, doi: 10.1021/jacs.6b03207.

[11] K. C. Bhamu, A. Soni, and J. Sahariya, "Revealing optoelectronic and transport properties of potential perovskites Cs2PdX6 (X = Cl, Br): A probe from density functional theory (DFT)," *Solar Energy*, vol. 162, pp. 336–343, Mar. 2018, doi: 10.1016/j.solener.2018.01.059.

[12] T. Ghrib *et al.*, "A new lead free double perovskites K2Ti(Cl/Br)6; a promising materials for optoelectronic and transport properties; probed by DFT," *Materials Chemistry and Physics*, vol. 264, p. 124435, May 2021, doi: 10.1016/j.matchemphys.2021.124435.

[13] Y. Sun, Z. Shuai, and D. Wang, "Reducing Lattice Thermal Conductivity of the Thermoelectric SnSe Monolayer: Role of Phonon–Electron Coupling," *J. Phys. Chem. C*, vol. 123, no. 18, pp. 12001–12006, May 2019, doi: 10.1021/acs.jpcc.9b02344.

[14] Y. Shi, C. Sturm, and H. Kleinke, "Chalcogenides as thermoelectric materials," *Journal of Solid State Chemistry*, vol. 270, pp. 273–279, Feb. 2019, doi: 10.1016/j.jssc.2018.10.049.

[15] G. García, P. Palacios, A. Cabot, and P. Wahnón, "Thermoelectric Properties of Doped-Cu_3SbSe_4 Compounds: A First-Principles Insight," *Inorg. Chem.*, vol. 57, no. 12, pp. 7321–7333, Jun. 2018, doi: 10.1021/acs.inorgchem.8b00980.

[16] W. Khan and S. Goumri-Said, "Exploring the optoelectronic structure and thermoelectricity of recent photoconductive chalcogenides compounds, $CsCdInQ_3$ (Q = Se, Te)," *RSC Adv.*, vol. 5, no. 13, pp. 9455–9461, 2015, doi: 10.1039/C4RA13426E.

[17] F. Bendahma, M. Mana, S. Terkhi, S. Cherid, B. Bestani, and S. Bentata, "Investigation of high figure of merit in semiconductor XHfGe (X = Ni and Pd) half-Heusler alloys: Ab-initio study," *Computational Condensed Matter*, vol. 21, p. e00407, Dec. 2019, doi: 10.1016/j.cocom.2019.e00407.

[18] Guodong Li , Qi An , Umut Aydemir, Sergey I. Morozov , Bo Duan, Pengcheng Zhai , Qingjie Zhang, and William A. Goddard., "Intrinsic mechanical behavior of MgAgSb

thermoelectric material: An ab initio study," *Journal of Materiomics*, vol. 6, no. 1, pp. 24–32, Mar. 2020, doi: 10.1016/j.jmat.2019.11.002.

[19] M. B. Maccioni, R. Farris, and V. Fiorentini, "*Ab initio* thermal conductivity of thermoelectric Mg 3 Sb 2 : Evidence for dominant extrinsic effects," *Phys. Rev. B*, vol. 98, no. 22, p. 220301, Dec. 2018, doi: 10.1103/PhysRevB.98.220301.

[20] S. Ahmad Mir and D. C. Gupta, "Understanding the origin of semiconducting ferromagnetic character along with the high figure of merit in Cs2NaMCl6 (M = Cr, Fe) double perovskites," *Journal of Magnetism and Magnetic Materials*, vol. 519, p. 167431, Feb. 2021, doi: 10.1016/j.jmmm.2020.167431.

[21] W. F. Goh and W. E. Pickett, "Topological and thermoelectric properties of double antiperovskite pnictides," *J. Phys.: Condens. Matter*, vol. 32, no. 34, p. 345502, Aug. 2020, doi: 10.1088/1361-648X/ab86f1.

[22] Amjid Mahmood, Sikander Azam, Muhammad Irfan, Muhammad Arshad Kamran, Thamer Alharbi , Abdul Majid, Muhammad Waqas Iqbal, Shabbir Muhammad, Abdullah G. Al-Sehemi, Saleem Ayaz Khan, Souraya Goumri-Said, "Cation effect on electronic, optical and thermoelectric properties of perovskite oxynitrides: Density functional theory," *Materials Science in Semiconductor Processing*, vol. 107, p. 104800, Mar. 2020, doi: 10.1016/j.mssp.2019.104800.

[23] D. Li, S. Li, X. Li, B. Yang, and H. Zhong, "Efficiently synthesized n-type CoSb3 thermoelectric alloys under TGZM effect," *Materials Science in Semiconductor Processing*, vol. 123, p. 105542, Mar. 2021, doi: 10.1016/j.mssp.2020.105542.

[24] A. Shafique and Y.-H. Shin, "Thermoelectric and phonon transport properties of two-dimensional IV–VI compounds," *Sci Rep*, vol. 7, no. 1, p. 506, Mar. 2017, doi: 10.1038/s41598-017-00598-7.

[25] C. Sheng, D. Fan, and H. Liu, "High thermoelectric performance can be achieved in two-dimensional (PbTe)2 layer," *Physics Letters A*, vol. 384, no. 2, p. 126044, Jan. 2020, doi: 10.1016/j.physleta.2019.126044.

[26] M. A. Haque, S. Kee, D. R. Villalva, W. Ong, and D. Baran, "Halide Perovskites: Thermal Transport and Prospects for Thermoelectricity," *Adv. Sci.*, vol. 7, no. 10, p. 1903389, May 2020, doi: 10.1002/advs.201903389.

[27] Y. Zhang, Q. Yao, J. Qian, X. Zhao, D. Li, and Q. Mi, "Thermoelectric properties of all-inorganic perovskite CsSnBr3: A combined experimental and theoretical study," *Chemical Physics Letters*, vol. 754, p. 137637, Sep. 2020, doi: 10.1016/j.cplett.2020.137637.

[28] X. Qian, X. Gu, and R. Yang, "Lattice thermal conductivity of organic-inorganic hybrid perovskite $CH_3NH_3PbI_3$," *Appl. Phys. Lett.*, vol. 108, no. 6, p. 063902, Feb. 2016, doi: 10.1063/1.4941921.

[29] S.-D. Guo and J.-L. Wang, "Potential thermoelectric materials $CsMI_3$ (M = Sn and Pb) in perovskite structures from first-principles calculations," *RSC Adv.*, vol. 6, no. 103, pp. 101552–101559, 2016, doi: 10.1039/C6RA14144G.

[30] T. K. Joshi, Pravesh, G. Sharma, and A. S. Verma, "Investigation of structural, electronic, optical and thermoelectric properties of Ethylammonium tin iodide (CH3CH2NH3SnI3): An appropriate hybrid material for photovoltaic application," *Materials Science in Semiconductor Processing*, vol. 115, p. 105111, Aug. 2020, doi: 10.1016/j.mssp.2020.105111.

[31] T. Wu and P. Gao, "Development of Perovskite-Type Materials for Thermoelectric Application," *Materials*, vol. 11, no. 6, p. 999, Jun. 2018, doi: 10.3390/ma11060999.

[32] T. Ye, X. Wang, X. Li, A. Q. Yan, S. Ramakrishna, and J. Xu, "Ultra-high Seebeck coefficient and low thermal conductivity of a centimeter-sized perovskite single crystal acquired by a modified fast growth method," *J. Mater. Chem. C*, vol. 5, no. 5, pp. 1255–1260, 2017, doi: 10.1039/C6TC04594D.

[33] A. E. Fedorovskiy, N. A. Drigo, and M. K. Nazeeruddin, "The Role of Goldschmidt's Tolerance Factor in the Formation of A_2BX_6 Double Halide Perovskites and its Optimal Range," *Small Methods*, vol. 4, no. 5, p. 1900426, May 2020, doi: 10.1002/smtd.201900426.

[34] Dianxing Ju, Xiaopeng Zheng, Jun Yin, Zhiwen Qiu, Bekir Turedi, Xiaolong Liu, Yangyang Dang, Bingqiang Cao, Omar F. Mohammed, Osman M. Bakr, and Xutang Tao, "Tellurium-Based Double Perovskites A_2TeX_6 with Tunable Band Gap and Long Carrier Diffusion Length for Optoelectronic Applications," *ACS Energy Lett.*, vol. 4, no. 1, pp. 228–234, Jan. 2019, doi: 10.1021/acsenergylett.8b02113.

[35] Malak Azmat Ali, Sajad Ahmad Dar, Abeer A. AlObaid, Tahani I. Al-Muhimeed, H. H. Hegazy, Ghazanfar Nazir, G. Murtaza., "Appealing perspectives of structural, electronic, mechanical, and thermoelectric properties of Tl2(Se, Te)Cl6 vacancy-ordered double perovskites," *Journal of Physics and Chemistry of Solids*, vol. 159, p. 110258, Dec. 2021, doi: 10.1016/j.jpcs.2021.110258.

[36] Q. Mahmood, T. Ghrib, A. Rached, A. Laref, and M. A. Kamran, "Probing of mechanical, optical and thermoelectric characteristics of double perovskites Cs2GeCl/Br6

by DFT method," *Materials Science in Semiconductor Processing*, vol. 112, p. 105009, Jun. 2020, doi: 10.1016/j.mssp.2020.105009.

[37] Muniba Huma, Muhammad Rashid, Q. Mahmood, Eman Algrafy, Nessrin A. Kattan, A. Laref, A.S. Bhatti, "Physical properties of lead-free double perovskites A2SnI6 (A= Cs, Rb) using ab-initio calculations for solar cell applications," *Materials Science in Semiconductor Processing*, vol. 121, p. 105313, Jan. 2021, doi: 10.1016/j.mssp.2020.105313.

[38] R. Ullah, M. A. Ali, G. Murtaza, A. Khan, and A. Mahmood, "Ab initio study for the structural, electronic, magnetic, optical, and thermoelectric properties of K_2OsX_6 (X = Cl, Br) compounds," *Int J Energy Res*, vol. 44, no. 11, pp. 9035–9049, Sep. 2020, doi: 10.1002/er.5613.

[39] R. Ullah, M. A. Ali, G. Murtaza, A. Mahmood, and S. M. Ramay, "The significance of anti-fluorite Cs_2NBI_6 via its structural, electronic, magnetic, optical and thermoelectric properties," *Int J Energy Res*, vol. 44, no. 13, pp. 10179–10191, Oct. 2020, doi: 10.1002/er.5638.

[40] H. Boysen and A. W. Hewat, "A neutron powder investigation of the structural changes in K_2SnCl_6," *Acta Crystallogr B Struct Sci*, vol. 34, no. 5, pp. 1412–1418, May 1978, doi: 10.1107/S0567740878005816.

[41] T. Higashi, S. Syoyama, and K. Osaki, "Structure of potassium hexabromostannate(IV) at room temperature," *Acta Crystallogr B Struct Sci*, vol. 35, no. 1, pp. 144–146, Jan. 1979, doi: 10.1107/S0567740879002776.

Chapter I: Solar cells and Thermoelectricity

I.1. Introduction

Because of the recent decades' sharp increase in energy use, scientists have been actively looking for fossil fuel substitutes. Because sunlight is a clean, endless energy source, it has become a vital replacement **[1]**. As a result, considerable efforts are being made to create ecologically benign and economically viable technological systems that utilize the sun spectrum to power thermoelectric generators and photovoltaic cells. It is considered necessary to investigate mechanisms like photovoltaic and the thermal electric conversion processes of Seebeck and Peltier. **[2,3]**. At present, the primary challenge lies in identifying suitable materials for these applications, prompting extensive research to assess their efficacy in energy conversion.

In this chapter, we are going to give an overview on the principal physical effects used in the working mechanisms of solar cells, in thermoelectric generators and in hybrid systems. Furthermore, we will summarise some important historical steps in the development of these applications.

I.2. Solar cells

I.2.1. Photovoltaic effect

In semiconductors, electrons can be excited to higher energies by photons with sufficient energy. Stimulated electrons can be useful if they are dragged to an external circuit before relaxing to the ground state. In this way, light energy is transformed into electrical energy. Such a device is a photovoltaic cell, which uses semiconductors as light-absorbing materials and generates electron-hole pairs from incident photons from the sun. The device's inherent spatial asymmetry then separates and collects electron and hole at each of its two contacts **[4]**. When a load is connected, the charges go to the external circuit and can produce voltage and current.

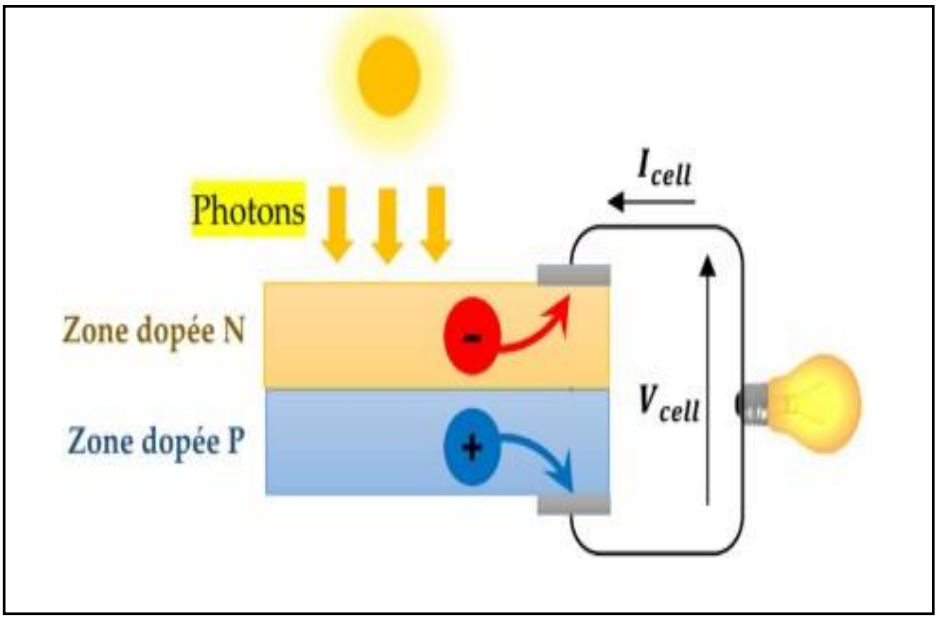

Figure. I. 1: Photovoltaic effect

In solar cell devices, when electrons are elevated to higher energy levels across the band gap, they quickly lose their excess energy through thermal relaxation, which occurs within femtoseconds. However, radiative recombination, where electrons emit photons and return to their ground state, takes a longer time, typically in the order of microseconds. This time delay allows for the collection of excited electrons. The difference in chemical potential between the excited and ground state populations creates an electrical potential difference between the device's two terminals.

The incoming solar flux causes an increase in photon absorption when the solar cell is exposed to light. However, emission also rises since a large number of electrons are already excited. This indicates that radiative recombination causes energy loss in solar cell devices at all times.

The net current density of a photovoltaic cell in the device is given by:

$$J(V) = J_{sc} - J_{dark}(V) \tag{I-1}$$

J_{sc} is the photocurrent density resulting from the net absorption of light. In an ideal situation where the material absorbs light perfectly without reflecting, and where charge separation is flawless, then:

$$J_{sc} = q \int_{E_g}^{\infty} b_s(E) dE \tag{I-2}$$

Where: E_g represents the band gap of the absorbing material, and $b_s(E)$ represents the spectrum of sunlight.

$J_{dark}(V)$: The dark current derived from spontaneous emission, specifically radiative recombination loss. This current varies depending on the applied bias voltage, V, to the device

$$J_{dark} = J_0\left(e^{qV/k_BT} - 1\right) \quad \text{(I-3)}$$

When $J(V)$ equals zero, it means that the applied bias voltage is at the open-circuit voltage (V_{oc}), and the photocurrent and dark current are perfectly balanced, cancelling each other out. The power output of the solar cell device and its power conversion efficiency (PCE) are then determined by the applied bias voltage. PCE also relies on the band gap (E_g) of the absorbing material, as absorption is influenced by E_g. If E_g is too small, the absorbed energy is wasted through carrier thermal relaxation. On the other hand, if E_g is too large, the photocurrent will be low because most low-energy photons won't be absorbed. Therefore, there is an optimal value of E_g for a given incident spectrum. For the solar spectrum, the ideal E_g is 1.4 eV, resulting in a PCE of 33% **[5]**.

In real-world solar cell devices, there are additional losses apart from radiative recombination. Auger recombination is one such loss that occurs when the carrier density is high. It involves an excited electron transitioning to the ground state, transferring its energy to another carrier, which eventually dissipates as heat during relaxation to the band edge. Another loss mechanism is Shockley-Read-Hall (SRH) recombination **[6]**, which is associated with trap states or defects in semiconductors. SRH recombination can be minimized by controlling the density of defects in semiconductors. It occurs when a trap state captures one carrier and later captures another carrier with the opposite charge. If shallow defects near the band edge capture carriers, there's a chance for thermal activation before the capture of the opposite-polarity carrier, preventing recombination. However, deep defect states near the center of the band gap lead to energy loss as heat. In practical materials, SRH recombination is the primary source of loss.

I.2.2. Different generations of solar cells

The concept of photovoltaic cell generations serves as a way to trace the historical development of solar cell technology. Over the past few decades, since the invention of solar cells, these generations can be broadly categorized into four main stages **[7]**:

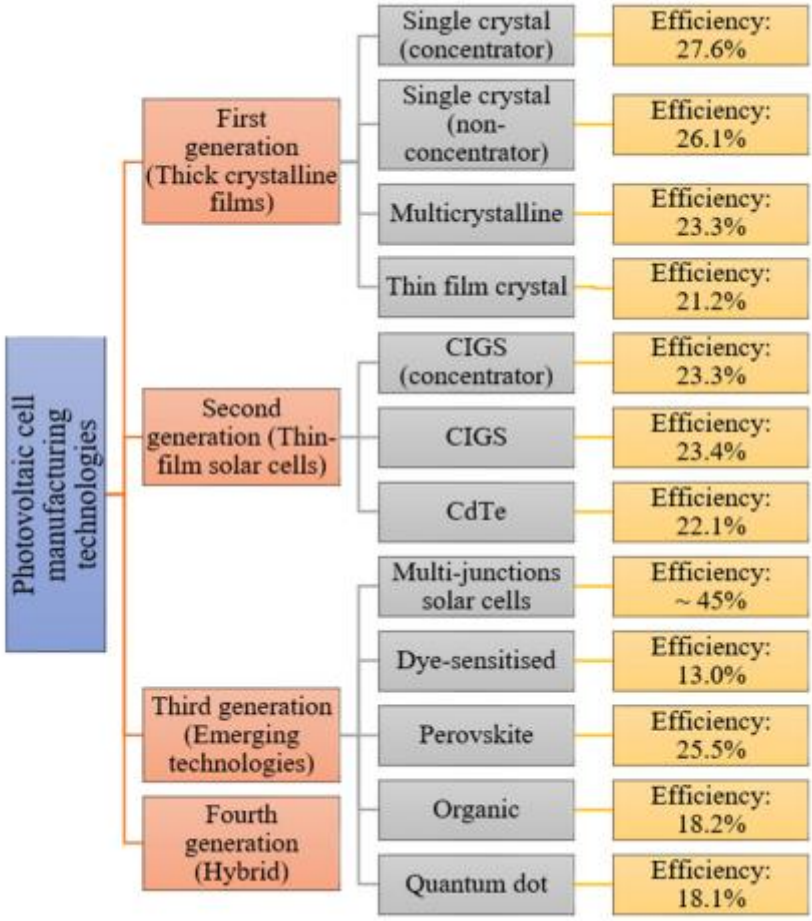

Figure. I. 2: Exemples of solar cells efficiencies

First Generation of Photovoltaic Cells

The first generation of photovoltaic cells is primarily based on silicon, which has been a dominant force in the solar cell market for decades. These silicon-based PV cells make up over 80% of the world's installed capacity and hold a 90% market share due to their relatively high efficiency. There are different types of first-generation photovoltaic cells, including monocrystalline silicon (m-si), polycrystalline silicon (p-si), and gallium arsenide (GaAs) cells **[8,9].**

-Monocrystalline Silicon (m-si):

- Efficiency: 15% to 24%
- Band gap: Approximately 1.1 eV

- Lifespan: 25 years
- Advantages: High stability, excellent performance, long service life
- Limitations: High manufacturing cost, sensitivity to temperature, absorption issues, material wastage.

- Polycrystalline Silicon (p-si):

- Efficiency: 10% to 18%
- Band gap: Approximately 1.7 eV
- Lifespan: 14 years
- Advantages: Simple manufacturing process, cost-effective, reduces silicon waste, better absorption compared to monocrystalline silicon
- Limitations: Lower efficiency compared to monocrystalline silicon, still sensitive to temperature.

- Gallium Arsenide (GaAs):

- Efficiency: 28% to 30%
- Band gap: Approximately 1.43 eV
- Lifespan: 18 years
- Advantages: High stability, reduced temperature sensitivity, superior absorption compared to monocrystalline silicon, excellent efficiency
- Limitations: Extremely expensive.

In summary, the first generation of photovoltaic cells encompasses various materials, with silicon-based cells dominating the market due to their efficiency and longevity. While monocrystalline silicon offers high performance and stability, it comes at a higher cost. Polycrystalline silicon is more cost-effective but sacrifices some efficiency, while gallium arsenide provides exceptional efficiency but is prohibitively expensive. Each type of cell has its unique advantages and limitations, allowing consumers to choose the best option based on their specific needs and budget.

Second Generation of Photovoltaic Cells

The second generation of photovoltaic cells introduced thin-film technologies such as cadmium telluride (CdTe), gallium selenide (CIGS), and amorphous silicon (a-si) cells as lower-cost alternatives to crystalline silicon cells **[8]**. These thin-film technologies offered improved mechanical flexibility, making them suitable for various applications. However, this flexibility came at the expense of reduced efficiency.

- Amorphous Silicon (a-si):

- Efficiency: 5% to 12%
- Band gap: Approximately 1.7 eV
- Lifespan: 15 years
- Advantages: Cost-effective, abundant supply, non-toxic, high absorption coefficient
- Limitations: Lower efficiency, challenges in selecting dopant materials, poor minority carrier lifetime.

- **Cadmium Telluride/Cadmium Sulfide (CdTe/CdS):**
  - Efficiency: 15% to 16%
  - Band gap: Approximately 1.45 eV
  - Lifespan: 20 years
  - Advantages: High absorption rate, less material required for production
  - Limitations: Lower efficiency, toxicity of cadmium (Cd), limited availability of tellurium (Te), sensitivity to temperature fluctuations.

- Copper Indium Gallium Selenide (CIGS):

- Efficiency: 20%
- Band gap: Approximately 1.7 eV
- Lifespan: 12 years
- Advantages: Reduced material requirements for production
- Limitations: High cost, instability, sensitivity to temperature changes, and reliability concerns.

In summary, the second-generation photovoltaic cells, including CdTe, CIGS, and a-si, were designed to offer cost-effective alternatives to crystalline silicon cells while maintaining flexibility for various applications. Each technology has its unique advantages and limitations, such as varying efficiency levels, material toxicity concerns, and temperature sensitivity. These technologies represent an important step in expanding the possibilities for solar energy generation and addressing specific needs in the photovoltaic industry.

Third Generation of Photovoltaic Cells

The third generation of solar cells represents a diverse range of approaches, including tandem, perovskite, dye-sensitized, organic, and emerging concepts. These technologies vary widely in terms of cost, efficiency, and application **[8]**, spanning from low-efficiency yet cost-effective systems to expensive, high-efficiency options suitable for space applications.

- Dye-Sensitized Photovoltaic Cells:

- Efficiency: 5% to 20%

- Advantages: Lower cost, operation in low light and at wider angles, lower internal temperature, robustness, extended lifetime
- Limitations: Temperature stability issues, use of poisonous and volatile substances.

- Quantum Dot Photovoltaic Cells:

- Efficiency: 11% to 17%
- Advantages: Low production cost, low energy consumption
- Limitations: High natural toxicity, degradation concerns.
- Organic and Polymeric Photovoltaic Cells:
- Efficiency: 9% to 11%
- Advantages: Low processing cost, lighter weight, flexibility, thermal stability
- Limitations: Lower efficiency compared to other technologies.

- Perovskite Photovoltaic Cells:

- Efficiency: 21%
- Advantages: low-cost and simplified structure, lightweight, flexibility, high efficiency, low manufacturing cost
- Limitations: Stability issues.

- Multi-Junction Solar Cells:

- Efficiency: 36% and higher
- Advantages: High performance
- Limitations: Complex and expensive.

These third-generation photovoltaic cells, also known as "emerging concepts," **[10]** offer a wide range of possibilities for solar energy generation. They cater to various applications, from building integration to space missions. While some of these technologies have been in development for over 25 years **[11]**, they are still in the process of gaining market acceptance. Ongoing research and development efforts aim to improve their efficiency, stability, and overall performance, making them a promising area for the future of solar energy.

I.3. Thermoelectricity

Thermoelectricity consists of the direct conversion of thermal energy into electricity, and vice versa, in appropriate materials.

There are three thermoelectric effects which result from the coupling between the phenomena of electrical and thermal conduction: the Seebeck, Peltier and Thomson effects.

I.3.1. Thermoelectric effects

I.3.1.1. Seebeck effect

The Seebeck effect, discovered by Thomas-Johann Seebeck in 1821 **[12]**, describes the occurrence of an electric potential difference within a material when exposed to a temperature gradient. When two metallic materials, labelled A and B, are connected and a temperature difference exists between their junctions even when the circuit is open, a potential difference (ΔV) is created between these junctions (**Figure. I. 3**). This phenomenon is known as the Seebeck effect.

$$S = \frac{\Delta V_{AB}}{\Delta T_{AB}} \tag{I-4}$$

Where S is called Seebeck coefficient or thermoelectric power.

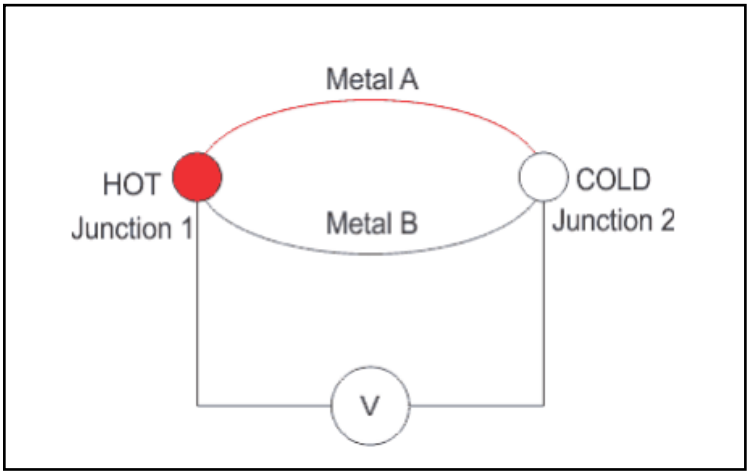

Figure. I. 3: A schematic diagram of Seebeck effect

I.3.1.2. Peltier effect

In 1834, the French physicist Jean Peltier discovered the second thermoelectric effect, which involves the generation of heat within a circuit when an electric current is applied. Specifically, when an electric current flows through the circuit, one junction releases heat ($\vec{Q}$), while the other junction absorbs heat. This phenomenon can be observed at the junction illustrated in **Figure. I. 4**. Notably, the amount of heat ($\vec{Q}$) absorbed or released is directly proportional to the magnitude of the injected current density ($\vec{J}$). The Peltier coefficient Π_{ab} is then defined by :

$$\vec{Q} = \Pi_{AB}.\vec{J} \quad \text{(I-5)}$$

$\vec{Q}$: surface heat flux.

Π_{AB}: Peltier coefficient.

$\vec{J}$: the charge flow.

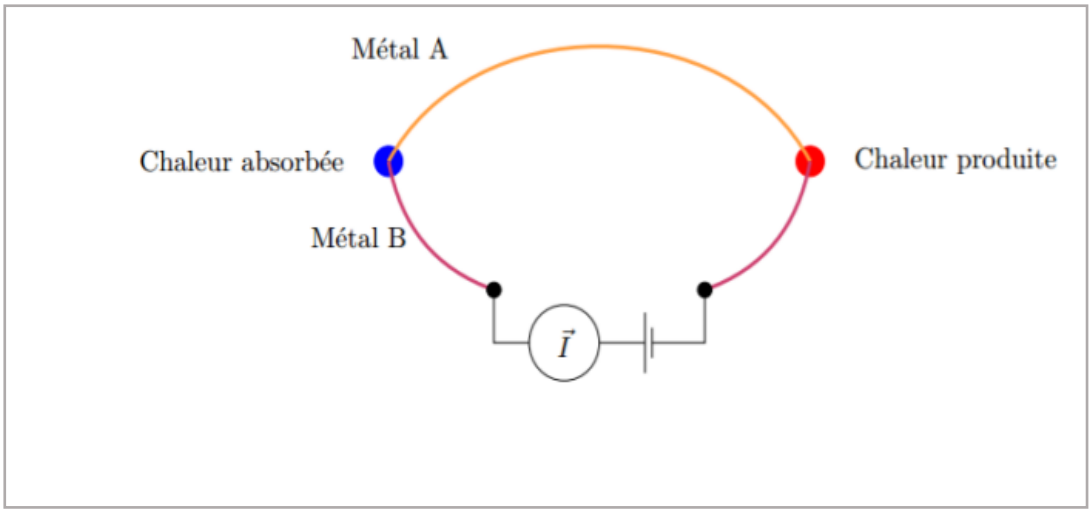

Figure. I. 4: A schematic diagram of Peltier effect

I.3.1.3. Thomson effect

In 1851, the English physicist William Thomson (also known as Lord Kelvin) identified the third thermoelectric effect, known as the Thomson effect. This effect becomes prominent when there exists both a temperature gradient and an electric current simultaneously within a material. It involves the generation or absorption of heat in each segment of the thermocouple. Unlike the first two thermoelectric effects, the Thomson effect pertains to a single material and does not necessitate the presence of a junction. To quantify the heat flux emitted or absorbed per unit volume in this effect, a specific formula is utilized **[5]**

$$Q_T = \tau.\vec{J}.\vec{\nabla}T \quad \text{(I-6)}$$

With $\boldsymbol{\tau}$ the Thomson coefficient.

The Kelvin relations establish a relation between the thermoelectric transport coefficients, including the Seebeck, Peltier, and Thomson coefficients.

$$\begin{cases} \boldsymbol{\Pi} = \boldsymbol{S}.T \\ \boldsymbol{\tau} = T\frac{dS}{dT} \end{cases} \quad \text{(I-7)}$$

I.3.2. Thermoelectric modules

Thermoelectric (TE) modules are semiconductor devices have the ability to directly transform thermal energy into electrical energy. When subjected to a temperature gradient, they utilize the Seebeck effect to produce a voltage, or they employ the Peltier effect to produce a gradient of temperature when they are given electricity.

TE modules have versatile applications and can be used for either cooling or power generation, as depicted in **Figure. I. 5**.

These TE modules consist of arrays of both N and P type semiconductors. By applying a heat source to one side and a cooling heat sink to the other side, they produce electric power. Conversely, when the current direction is reversed, electric power can be converted into cooling or heating **[13].**

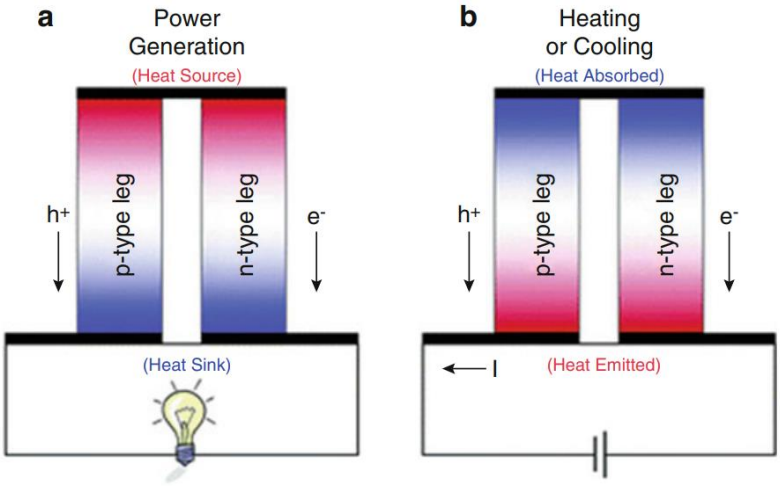

Figure. I. 5: Applications of thermoelectric devices **[14].**

I.3.3. Important parameters of TE materials

The optimal performance of thermoelectric (TE) modules relies on various factors, with material selection being a crucial consideration. When choosing Thermoelectric Generators (TEGs) for specific applications under varying conditions, it's essential to pick a semiconductor material that performs well within the temperature range of that application **[15]**.

In general, to achieve the highest efficiency, the key characteristic of a thermoelectric material is its dimensionless thermoelectric performance **Figure of merit**, denoted as **ZT [13]** :

$$ZT = \frac{S^2 \sigma \pi T}{\kappa_L + \kappa_e} \quad \text{(I-8)}$$

This parameter depends on the Seebeck coefficient (S), electrical conductivity (s), absolute temperature (T), and thermal conductivity (λ). To maximize thermoelectric efficiency, it's important to have a high ZT value. **Figure. I. 6** shows the variation of these parameters as function of carrier concentration **[44]**. In the other hand, **figure. I. 7** depicts temperature dependence of figure of merit ZT of a number of TE materials.

This implies that one way to enhance the efficiency of TEGs is to either discover materials with properties that result in higher ZT values or modify existing materials to improve their ZT value.

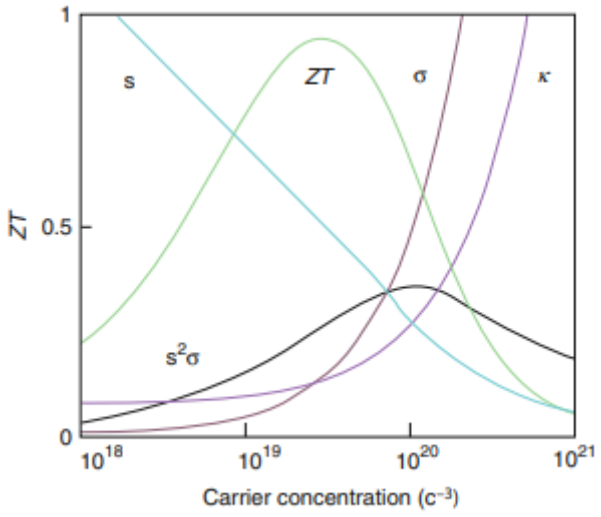

Figure. I. 6: Thermoelectric parameters variation in terms of carrier concentration (Source: Snyder and Toberer **[44]**).

I.3.4. Thermoelectric materials

Considerable progress has been reached in the field of thermoelectric materials, encompassing a wide range of materials such as, silicides, chalcogenides, Zintls, skutterudites, Heusler alloys, clathrates, oxides, composites, and organics . This progress has been facilitated by various approaches, including electronic band engineering, nano-engineering, the phonon-glass electron-crystal strategy, and the utilization of magnetic effects, among others **[16,17]**.

A recent noteworthy development is the report by C. Zhou et al. **[18]**, highlighting a high ZT value of 3.10 for polycrystalline SnSe, achieved at 783 K by eliminating oxide impurities. This

discovery not only exceeds the ZT ceiling of 3 for thermoelectric materials, but it also shows a noteworthy average ZT of about 2 in the 400–700 K temperature range.

Such achievements have become increasingly common over the past two decades, with extensive literature available on various thermoelectric materials and techniques to enhance their properties.

Reviews by X. Shi et al. **[19]** and D. Beretta et al. **[16]** have comprehensively covered advancements in thermoelectric materials, structures, and device design, both from a contemporary and historical perspective. Additionally, a great deal of other reviews have examined particular facets of thermoelectric materials, such as flexible and wearable thermoelectric materials and devices **[21]**, carbon allotrope hybrids **[20]**, and fiber-based thermoelectric materials **[21]**. and flexible and wearable thermoelectric materials and devices **[19**,**22**,**23]**.

It's important to note that while enhancing the thermoelectric properties of materials is crucial, there are additional challenges to address for practical applications. These include factors such as machinability, the availability of raw materials, thermal stability, mechanical stability, toxicity, and the chemical stability of the utilized materials. Research, such as the investigation of TE materials' fracture toughness conducted by G. Li et al. **[24]**, is exploring strategies to improve the mechanical strength of TE materials, helping to create high-performing TE devices with superior mechanical dependability.

Overall, the advancements in thermoelectric materials hold great promise and are essential for expanding the practicality and viability of thermoelectric devices.

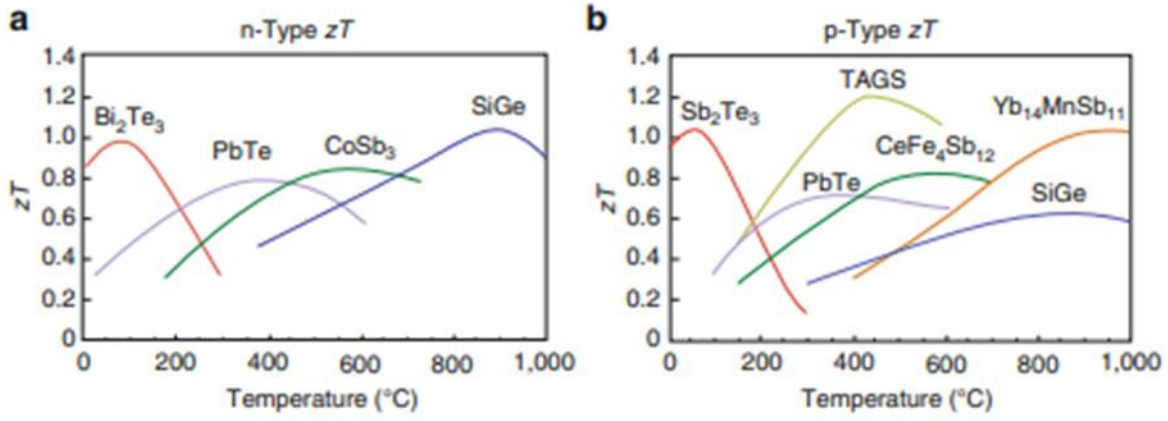

Figure I. 7: Temperature dependence of ZT for some TE materials (Source: C. Bera, Thermoelectric properties of nanocomposites materials, Engineering Sciences, Ecole Centrale Paris, 2010).

I.4. Hybrid systems thermo-photovoltaic

Hybrid systems thermo-photovoltaic devices represent innovative solutions for harnessing a broader spectrum of solar radiation, leveraging the capabilities of both solar converters and Thermoelectric Generators (TEGs) for power generation. To improve the usability and reliability of these systems, researchers have been working actively.

To take use of the broader sun spectrum, the idea of solar-based thermoelectric devices has emerged. The integration of thermoelectric materials with solar electricity conversion technology has been the subject of recent research efforts, yielding two primary categories: Two types of devices are (i) hybrid photovoltaic-thermoelectric (PV-TEG) systems and (ii) solar thermoelectric generators (STEGs).

For usage in solar thermoelectric applications, a variety of classes of TM materials with varying temperature ranges are available. As an example, alloys containing bismuth telluride can be used in low-temperature applications (30° to 200 °C) **[25,26].** For medium-temperature applications (200 to 500 °C), half-Heuslers, skutterudites, and PbTe/PbSe alloys are suitable **[25].** SiGe alloys demonstrate the capacity to function at high temperatures for prolonged periods of time with no material deterioration **[25,27]**.

A TEG module can receive a broad range of photons when a PV module is coupled with it, enabling the generation of electricity through the thermoelectric effect **[28]**. This approach enhances conversion efficiency and reduces heat dissipation through the PV module.

A hybrid PV-TEG system effectively utilizes the thermal losses associated with a PV module to generate electricity. This innovative approach represents a promising avenue for more efficient and sustainable solar power generation.

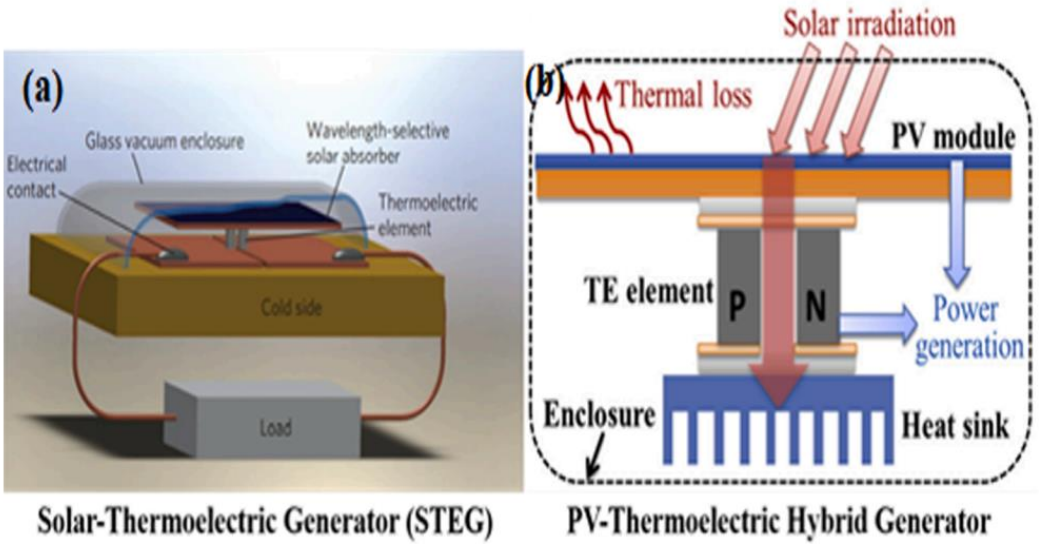

Figure. I. 8: Hybrid systems **[26]**

I.4.1. STEG device structure & optimization

A Solar Thermoelectric Generator (STEG) consists of a Thermoelectric Generator (TEG) placed between a solar absorber and a heat sink. The solar absorber concentrates sunlight onto a specific focal point, while the heat sink removes excess heat, maintaining a thermal gradient across the TEG. The solar absorber is larger than the STEG setup's cross-sectional area. The TEG converts heat from the PV module into electrical energy, effectively utilizing generated heat and enhancing hybrid system performance. Strategies to improve STEG performance include increasing the temperature gradient across the TEG legs, enhancing the ZT of thermoelectric elements, using concentrators, heat pipe arrays, and evacuated enclosures. Efficient thermoelectric materials, along with TEG management and thoughtful thermal design, play crucial roles in enhancing generator performance.

I.4.2. PV-TEG hybrid device structure & optimization

In 2008, Vorobiev et al. explored the concept of coupled Photovoltaic and Thermal Converters (PV-TEG) **[29]**, which laid the foundation for the development of new PV-TEG devices. These hybrid systems can be configured in two main designs. In the first arrangement, a solar cell is positioned above a concentrator that concentrates solar radiation onto a Thermoelectric (TE) module. Alternatively, in a different setup, the solar cell is placed between the concentrator and the TE module and can operate at higher temperatures **[30]**. The overall

efficiency of the PV-TEG hybrid system is estimated based on the efficiencies of the TE generator and an ideal solar cell.

In this hybrid system, a series of TE converters are mounted on a heat sink attached to the rear of the PV module. These thermoelectric converters facilitate the conversion of heat generated within the PV module into electrical energy. Researchers, such as Kraemer et al. in 2008 **[30]**, have developed optimization methodologies for these hybrid systems.

Furthermore, in 2011, Sark reported module temperatures of approximately 80°C under high irradiation and varying ambient temperatures, depending on the system design **[31]**. This arrangement generates a maximum temperature difference in the range of 50–60°C, prompting the use of low-temperature thermoelectric materials. Ongoing research efforts aim to enhance the efficiency of PV-TEG hybrid systems, exploring various avenues to maximize their performance.

I.4.3. Applications of STEGs and PV-TEG hybrid generators

The demand for Solar Thermoelectric Generators (STEGs) and Photovoltaic-Thermoelectric (PV-TEG) hybrid generators has been steadily increasing due to their rising conversion efficiencies. These technologies are scalable and suitable for both small and large-scale applications **[33]**. STEGs find use in diverse applications such as micro power generation **[34]**, mobile computing **[35]**, terrestrial applications **[36-38]**, space applications **[39]**, electricity and heat supply **[40]**, automotive **[28]**, air pre-heating, pre-cooling **[41]**, water-pumping **[42]**, and battery energy storage **[43]**.

Key factors for enhancing the overall performance of STEGs and PV-TEG hybrid systems **[32]** include utilizing thermoelectric materials with high ZT values, high-efficiency PV modules, and effective heat dissipation systems. Researchers are actively exploring various aspects, including novel thermoelectric materials with high figure-of-merit, modern solar energy collection and transfer techniques, and advanced optimization designs for STEG and PV-TEG systems.

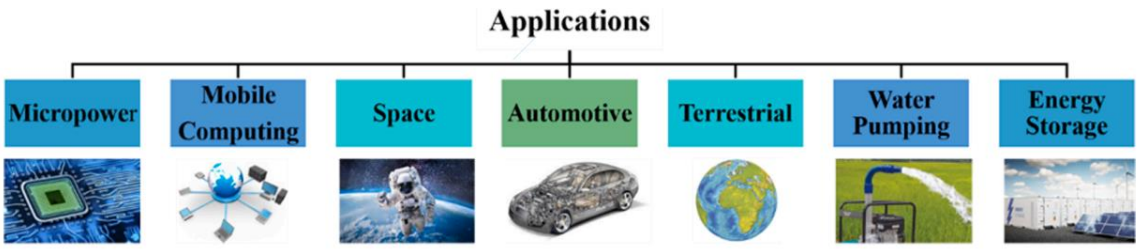

Figure. I. 9: . Some Solar based TEG devices applications **[32]**

By focusing on materials with improved figure-of-merit at higher temperatures and optimizing module designs, solar thermoelectric systems have the potential to become economically viable solutions for small-scale PV-based power generation technologies. Predictions indicate that STEG system efficiency will continue to improve, potentially reaching values around 25% for zT values greater than 2.

I.5. Conclusion

In conclusion, a comprehensive exploration of the evolution of photovoltaic cells, categorizing them into three generations, each with its unique set of materials, advantages, and limitations. The first generation, dominated by silicon-based cells, emphasizes efficiency and longevity, while the second generation introduces thin-film technologies as cost-effective alternatives with improved flexibility. The third generation explores emerging concepts, showcasing a diverse range of technologies with varying efficiency levels and applications.

Moreover, the significant progress in thermoelectric materials, highlighting achievements such as the remarkable ZT value for polycrystalline SnSe. The advancements in this field, facilitated by various approaches, hold great promise for enhancing the practicality and viability of thermoelectric devices, though challenges related to material properties and practical applications persist.

Overall, the discussion underscores the continuous efforts in research and development across generations of photovoltaic cells and thermoelectric materials. The ongoing pursuit of increased efficiency, stability, and overall performance reflects a promising trajectory for the future of sustainable energy.

References

[1] W.-J. Yin, B. Weng, J. Ge, Q. Sun, Z. Li, and Y. Yan, "Oxide perovskites, double perovskites and derivatives for electrocatalysis, photocatalysis, and photovoltaics," *Energy Environ. Sci.*, vol. 12, no. 2, pp. 442–462, 2019, doi: 10.1039/C8EE01574K.

[2] Po-Kai Kung, Ming-Hsien Li, Pei-Ying Lin, Jia-Yun Jhang, Martina Pantaler, Doru C. Lupascu, Giulia Grancini, and Peter Chen., "Lead-Free Double Perovskites for Perovskite Solar Cells," *Sol. RRL*, vol. 4, no. 2, p. 1900306, Feb. 2020, doi: 10.1002/solr.201900306.

[3] M. M. Lee, J. Teuscher, T. Miyasaka, T. N. Murakami, and H. J. Snaith, "Efficient Hybrid Solar Cells Based on Meso-Superstructured Organometal Halide Perovskites," *Science*, vol. 338, no. 6107, pp. 643–647, Nov. 2012, doi: 10.1126/science.1228604.

[4] J. Bisquert, *The physics of solar cells: perovskites, organics, and photovoltaic fundamentals*. Boca Raton, FL: CRC Press, Taylor & Francis Group, 2018.

[5] S. Rühle, "Tabulated values of the Shockley–Queisser limit for single junction solar cells," *Sol. Energy*, vol. 130, pp. 139–147, Jun. 2016, doi: 10.1016/j.solener.2016.02.015.

[6] W. Shockley and W. T. Read, "Statistics of the Recombinations of Holes and Electrons," *Phys. Rev.*, vol. 87, no. 5, pp. 835–842, Sep. 1952, doi: 10.1103/PhysRev.87.835.

[7] S. Hegedus and A. Luque, "Achievements and Challenges of Solar Electricity from Photovoltaics," in *Handbook of Photovoltaic Science and Engineering*, 1st ed., A. Luque and S. Hegedus, Eds., Wiley, 2010, pp. 1–38. doi: 10.1002/9780470974704.ch1.

[8] Suman, P. Sharma, and P. Goyal, "Evolution of PV technology from conventional to nano-materials," *Mater. Today Proc.*, vol. 28, pp. 1593–1597, 2020, doi: 10.1016/j.matpr.2020.04.846.

[9] A. Richter, M. Hermle, and S. W. Glunz, "Reassessment of the Limiting Efficiency for Crystalline Silicon Solar Cells," *IEEE J. Photovolt.*, vol. 3, no. 4, pp. 1184–1191, Oct. 2013, doi: 10.1109/JPHOTOV.2013.2270351.

[10] P. Peumans, A. Yakimov, and S. R. Forrest, "Small molecular weight organic thin-film photodetectors and solar cells," *J. Appl. Phys.*, vol. 93, no. 7, pp. 3693–3723, Apr. 2003, doi: 10.1063/1.1534621.

[11] W. A. Dunlap-Shohl, Y. Zhou, N. P. Padture, and D. B. Mitzi, "Synthetic Approaches for Halide Perovskite Thin Films," *Chem. Rev.*, vol. 119, no. 5, pp. 3193–3295, Mar. 2019, doi: 10.1021/acs.chemrev.8b00318.

[12] T. J. Seebeck, "Ueber die magnetische Polarisation der Metalle und Erze durch Temperaturdifferenz," *Ann. Phys.*, vol. 82, no. 3, pp. 253–286, 1826, doi: 10.1002/andp.18260820302.

[13] X. F. Zheng, C. X. Liu, Y. Y. Yan, and Q. Wang, "A review of thermoelectrics research – Recent developments and potentials for sustainable and renewable energy applications," *Renew. Sustain. Energy Rev.*, vol. 32, pp. 486–503, Apr. 2014, doi: 10.1016/j.rser.2013.12.053.

[14] J. R. Szczech, J. M. Higgins, and S. Jin, "Enhancement of the thermoelectric properties in nanoscale and nanostructured materials," *J Mater Chem*, vol. 21, no. 12, pp. 4037–4055, 2011, doi: 10.1039/C0JM02755C.

[15] Zhiqiang Niu, Shuhai Yu, Hai Diao, Qianshan Li, Kui Jiao ⇑ , Qing Du, Hua Tian, Gequn Shu, "Elucidating modeling aspects of thermoelectric generator," *Int. J. Heat Mass Transf.*, vol. 85, pp. 12–32, Jun. 2015, doi: 10.1016/j.ijheatmasstransfer.2015.01.107.

[16] D. Beretta *et al.*, "Thermoelectrics: From history, a window to the future," *Mater. Sci. Eng. R Rep.*, vol. 138, p. 100501, Oct. 2019, doi: 10.1016/j.mser.2018.09.001.

[17] B. Cai, H. Hu, H.-L. Zhuang, and J.-F. Li, "Promising materials for thermoelectric applications," *J. Alloys Compd.*, vol. 806, pp. 471–486, Oct. 2019, doi: 10.1016/j.jallcom.2019.07.147.

[18] C. Zhou *et al.*, "Polycrystalline SnSe with a thermoelectric figure of merit greater than the single crystal," *Nat. Mater.*, vol. 20, no. 10, pp. 1378–1384, Oct. 2021, doi: 10.1038/s41563-021-01064-6.

[19] L. Zhang, X.-L. Shi, Y.-L. Yang, and Z.-G. Chen, "Flexible thermoelectric materials and devices: From materials to applications," *Mater. Today*, vol. 46, pp. 62–108, Jun. 2021, doi: 10.1016/j.mattod.2021.02.016.

[20] W.-D. Liu, Y. Yu, M. Dargusch, Q. Liu, and Z.-G. Chen, "Carbon allotrope hybrids advance thermoelectric development and applications," *Renew. Sustain. Energy Rev.*, vol. 141, p. 110800, May 2021, doi: 10.1016/j.rser.2021.110800.

[21] X.-L. Shi, W.-Y. Chen, T. Zhang, J. Zou, and Z.-G. Chen, "Fiber-based thermoelectrics for solid, portable, and wearable electronics," *Energy Environ. Sci.*, vol. 14, no. 2, pp. 729–764, 2021, doi: 10.1039/D0EE03520C.

[22] S. Xu, X.-L. Shi, M. Dargusch, C. Di, J. Zou, and Z.-G. Chen, "Conducting polymer-based flexible thermoelectric materials and devices: From mechanisms to applications," *Prog. Mater. Sci.*, vol. 121, p. 100840, Aug. 2021, doi: 10.1016/j.pmatsci.2021.100840.

[23] M. Dargusch, W. Liu, and Z. Chen, "Thermoelectric Generators: Alternative Power Supply for Wearable Electrocardiographic Systems," *Adv. Sci.*, vol. 7, no. 18, p. 2001362, Sep. 2020, doi: 10.1002/advs.202001362.

[24] G. Li *et al.*, "Fracture toughness of thermoelectric materials," *Mater. Sci. Eng. R Rep.*, vol. 144, p. 100607, Apr. 2021, doi: 10.1016/j.mser.2021.100607.

[25] D. Mills, "Advances in solar thermal electricity technology," *Sol. Energy*, vol. 76, no. 1–3, pp. 19–31, Jan. 2004, doi: 10.1016/S0038-092X(03)00102-6.

[26] D. Kraemer *et al.*, "High-performance flat-panel solar thermoelectric generators with high thermal concentration," *Nat. Mater.*, vol. 10, no. 7, pp. 532–538, Jul. 2011, doi: 10.1038/nmat3013.

[27] P. Li, L. Cai, P. Zhai, X. Tang, Q. Zhang, and M. Niino, "Design of a Concentration Solar Thermoelectric Generator," *J. Electron. Mater.*, vol. 39, no. 9, pp. 1522–1530, Sep. 2010, doi: 10.1007/s11664-010-1279-0.

[28] X. Ju, Z. Wang, G. Flamant, P. Li, and W. Zhao, "Numerical analysis and optimization of a spectrum splitting concentration photovoltaic–thermoelectric hybrid system," *Sol. Energy*, vol. 86, no. 6, pp. 1941–1954, Jun. 2012, doi: 10.1016/j.solener.2012.02.024.

[29] Yu. Vorobiev, J. González-Hernández, P. Vorobiev, and L. Bulat, "Thermal-photovoltaic solar hybrid system for efficient solar energy conversion," *Sol. Energy*, vol. 80, no. 2, pp. 170–176, Feb. 2006, doi: 10.1016/j.solener.2005.04.022.

[30] D. Kraemer, L. Hu, A. Muto, X. Chen, G. Chen, and M. Chiesa, "Photovoltaic-thermoelectric hybrid systems: A general optimization methodology," *Appl. Phys. Lett.*, vol. 92, no. 24, p. 243503, Jun. 2008, doi: 10.1063/1.2947591.

[31] W. G. J. H. M. V. Sark, "Feasibility of photovoltaic – Thermoelectric hybrid modules," *Appl. Energy*, vol. 88, no. 8, pp. 2785–2790, Aug. 2011, doi: 10.1016/j.apenergy.2011.02.008.

[32] K. Tyagi, B. Gahtori, S. Kumar, and S. R. Dhakate, "Advances in solar thermoelectric and photovoltaic-thermoelectric hybrid systems for power generation," *Sol. Energy*, vol. 254, pp. 195–212, Apr. 2023, doi: 10.1016/j.solener.2023.02.051.

[33] L. L. Baranowski, G. J. Snyder, and E. S. Toberer, "Concentrated solar thermoelectric generators," *Energy Environ. Sci.*, vol. 5, no. 10, p. 9055, 2012, doi: 10.1039/c2ee22248e.

[34] R. Amatya and R. J. Ram, "Solar Thermoelectric Generator for Micropower Applications," *J. Electron. Mater.*, vol. 39, no. 9, pp. 1735–1740, Sep. 2010, doi: 10.1007/s11664-010-1190-8.

[35] A. Muhtaroglu, A. Yokochi, and A. Von Jouanne, "Integration of thermoelectrics and photovoltaics as auxiliary power sources in mobile computing applications," *J. Power Sources*, vol. 177, no. 1, pp. 239–246, Feb. 2008, doi: 10.1016/j.jpowsour.2007.11.016.

[36] D. Kraemer, K. McEnaney, M. Chiesa, and G. Chen, "Modeling and optimization of solar thermoelectric generators for terrestrial applications," *Sol. Energy*, vol. 86, no. 5, pp. 1338–1350, May 2012, doi: 10.1016/j.solener.2012.01.025.

[37] S. Lv, Y. Ji, Z. Qian, Y. Pan, Y. Zhang, and W. He, "Preliminary experiment and performance evaluation of a terrestrial solar thermoelectric generators under fluctuant solar radiation," *Appl. Therm. Eng.*, vol. 190, p. 116753, May 2021, doi: 10.1016/j.applthermaleng.2021.116753.

[38] S. Lv *et al.*, "High-performance terrestrial solar thermoelectric generators without optical concentration for residential and commercial rooftops," *Energy Convers. Manag.*, vol. 196, pp. 69–76, Sep. 2019, doi: 10.1016/j.enconman.2019.05.089.

[39] N. Fuschillo, R. Gibson, F. K. Eggleston, and J. Epstein, "Solar thermoelectric generator for near-earth space applications," *IEEE Trans. Electron Devices*, vol. ED-13, no. 4, pp. 426–432, Apr. 1966, doi: 10.1109/T-ED.1966.15706.

[40] W. He, Y. Su, S. B. Riffat, J. Hou, and J. Ji, "Parametrical analysis of the design and performance of a solar heat pipe thermoelectric generator unit," *Appl. Energy*, vol. 88, no. 12, pp. 5083–5089, Dec. 2011, doi: 10.1016/j.apenergy.2011.07.017.

[41] N. Le Pierrès, M. Cosnier, L. Luo, and G. Fraisse, "Coupling of thermoelectric modules with a photovoltaic panel for air pre-heating and pre-cooling application; an annual simulation," *Int. J. Energy Res.*, vol. 32, no. 14, pp. 1316–1328, Nov. 2008, doi: 10.1002/er.1439.

[42] M. N. Ibrahim, H. Rezk, M. Al-Dahifallah, and P. Sergeant, "Hybrid Photovoltaic-Thermoelectric Generator Powered Synchronous Reluctance Motor for Pumping Applications," *IEEE Access*, vol. 7, pp. 146979–146988, 2019, doi: 10.1109/ACCESS.2019.2945990.

[43] K. N, "Photovoltaic and Thermoelectric Generator Combined Hybrid Energy System with an Enhanced Maximum Power Point Tracking Technique for Higher Energy Conversion Efficiency," *Sustainability*, vol. 13, no. 6, p. 3144, Mar. 2021, doi: 10.3390/su13063144.

[44] G. J. Snyder, E.S. Toberer, Complex Thermoelectric Materials. *Nat. Mater*. 7, 105–114, 2008.

Chapter II: Vacancy ordered double perovskites (VODPs)

II.1. Introduction

Although lead-based halide perovskites and organic-inorganic hybrid perovskites have high PCE, appropriate optical absorption, and tunable band gaps, their commercial applications have been limited due to the toxic effects of lead in the former and instability in the latter. As a result, scientists have been seeking for acceptable substitutes. In this regard, lead-free vacancy ordered double perovskites, have come to light as fascinating alternatives with potential qualities.

II.2. General presentation of the structure of vacancy ordered perovskite compounds

Before discussing vacancy ordered double perovskite compounds structure, a basic understanding of the simple perovskite structure is essential. Perovskite, originally, is a mineral composed of calcium oxide and titanium with the formula CaTiO3, which was discovered in the Ural Mountains in Russia. It was first described in 1839 by the German geologist Gustav Rose, who named it in honor of a prominent Russian mineralogist, Count Lev Aleksevich von Perovski.

II.2.1. The structure of simple perovskite

Currently, perovskites constitute one of the primary families of crystalline oxides, characterized by a general formula ABX_3. In this formula, 'A' can represent an alkali metal, alkaline earth metal, or a rare earth element (lanthanide), 'B' denotes a transition metal, and 'X' is typically oxygen, although it can occasionally be replaced by sulfur, nitrogen, a halogen, or hydroxide.

The ideal structure of a perovskite is a high-symmetry, face-centered cubic structure with a lattice parameter of a_0 (approximately 4 Ångströms), belonging to the space group **F**m3m **[1]**. This is the case for barium titanate ($BaTiO_3$). Its structure can be described as follows **(Figure II. 1a):** it consists of a cubic lattice of Ba^{+2} cations at the corners (site A), with O^{-2} anions located at the centers of the faces, and a Ti^{+4} cation occupying the octahedral site (site B) at the center of the cube.

Alternatively, this structure can be described **(Figure II. 1b)** as a cubic lattice of TiO_6 octahedra connected by corners, with Ba^{+2} cations occupying the centers of the cuboctahedra. Site A, in a cuboctahedral environment with a coordination number of twelve, is connected to the twelve nearest oxygen anions **(Figure II. 1c).** Site B, in an octahedral environment with a coordination number of six, is connected to the six nearest oxygen anions. In an octahedral

environment, oxygen has four cations A and two cations B as nearest neighbors, resulting in a coordination number of 6.

Perovskites can exhibit a wide variety of lower symmetries because they often deviate from this ideal cubic structure. This can occur in several ways, including:

- Distortion of the entire unit cell, such as elongation along a specific crystallographic direction.
- Displacement of ion A from the center of the cuboctahedron or ion B from the center of the octahedron.
- Rotation of the octahedra around an axis (referred to as "tilting").
- Deformation of the octahedra.

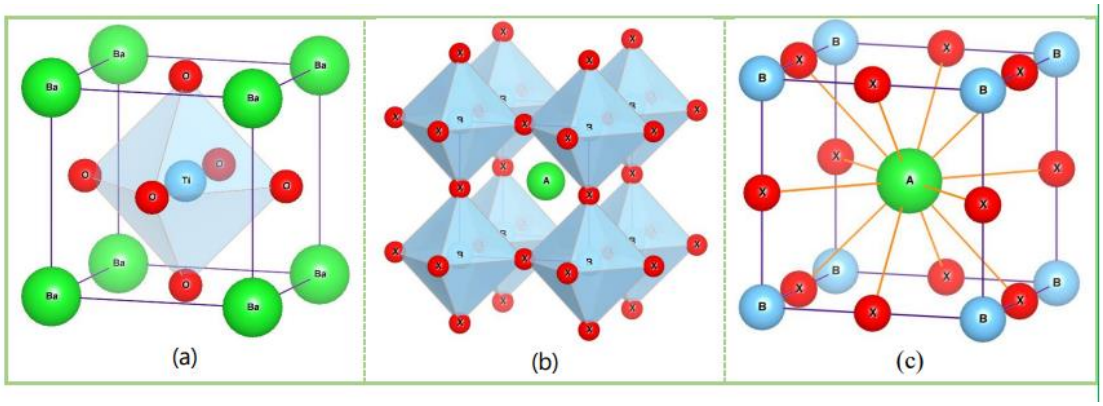

Figure. II. 1: Structure of an ideal cubic perovskite ABO_3 viewed in two different ways: (a) Site A at the origin (0,0,0); (b) Site B at the origin (0,0,0); (c) Coordination 12 of site A.

II.2.2. Vacancy ordered perovskite properties

II.2.2.1. The structure

The ABX_3 formula, which specifies the perovskite crystal structure, is precursored by $CaTiO_3$ **[2]**. The exceptional electrical properties of lead-based halide perovskites are largely attributed to their strong Oh symmetry, which is thought to be a critical component of the crystal structure of these materials **[3]**. Through cation transformation, the ordinary cubic perovskite archetype ABX_3 yields the ideal crystal structure of highly degenerate perovskites (HDP) with the general formula $A_2B_2X_6$ **(Figure II. 1a) [4]**. As a result, HDP crystal structures and traditional halide single perovskites have a number of traits in common. Two non-toxic B-cations, such as $B(I)X_6$ and $B(III)X_6$, that are separated in ABX_3 are commonly found in HDPs.

This happens when the same A-site cation, such as CH_3NH_3+ (MA+) or Cs+, occupies the center of the cuboctahedral cavity **[5]**. This results in a network structure of alternating B(I)X_6 and B(III)X_6 octahedra at the shared corners, which is referred to as rock-salt ordering **[6]**. Halogens can be substituted at the X-site, metal cations in different oxidation states at the B-site, and both inorganic and organic compounds at the A-site thanks to its crystal structure.

When one B-site cation is missing, HDP $A_2B_2X_6$ adopts a vacancy-ordered structure, as shown in **Figure II. 1b**. The A_2BX_6 structure bears many similarities to cubic ABX_3 perovskites. The three sites (A, B, and X) in vacancy-ordered HDPs can have their compositions changed, opening up a large phase space with lots of possibilities to change their dynamic, structural, and compositional characteristics **[7]**. Its tunability makes it possible to achieve desired optical and electrical characteristics. For example, the band gap of vacancy ordered double perovskite can be changed by the selection of X ions and the strong covalent contact between B and the X site **[8]**. Large halides generate a closely packed lattice that allows significant orbital overlap between neighboring isolated octahedra, which can lead to better carrier mobilities and lower effective weights of carriers. To obtain the necessary characteristics, the structure can accept a broad variety of tetravalent ions at the B site. The choice of B site in vacancy-ordered double perovskite greatly affects the features of charge transport and defect chemistry. All-inorganic cesium halide perovskites are interesting options because of their exceptional thermodynamic stability and moisture resistance when Cs+ is substituted for MA+ or $CH(NH_2)_2$+ (FA+). **[9**,**10]**.

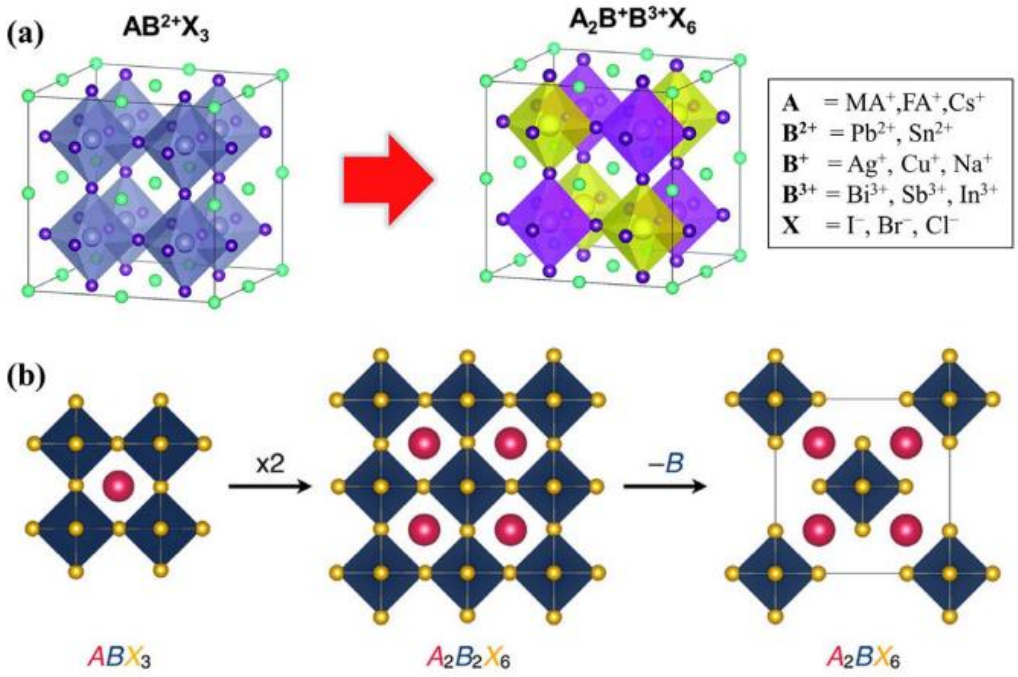

Figure. II. 2: Diagram of the relationship between the simple perovskite (ABX_3) and vacancy-ordered double perovskite (A_2BX_6) structures **[4,7].**

II.2.2.2. The band gap

The band gap and optical properties of vacancy-ordered double perovskites are influenced by the electronic states of the B- and X- site ions. Initially, let's examine the impact of the X-site halogen on the band alignment and optical gap. When smaller halogens ($I^- \rightarrow Br^- \rightarrow Cl^-$) are incorporated, it leads to a progressive increase in the band gap, as shown in a computational study by Cai et al **[11]**. This trend is consistent with experimental data for the Cs_2SnX_6 and Cs_2TiX_6 series. For instance, Cs_2SnI_6 has an experimental optical gap of approximately 1.3 eV **[12-15],** while replacing I^- with Br^- and Cl^- increases the optical gap to 2.7 and 3.9 eV **[14**,**16]**, respectively. This pattern holds for various members of the vacancy-ordered double perovskite family as long as the A- and B-site cations remain constant.

The influence of the X site halogen on the optical gap primarily arises from the presence of halogen states at the valence and conduction band edges. In most cases, the valence band maximum (VBM) is primarily composed of the halogen p states, making the choice of halogen a significant factor in determining the valence band energy. This is evident in the Cs_2SnX_6 series, where the highest occupied states originate from halogen nonbonding p states. When

smaller halogens are incorporated, these states move to lower energies due to the decreasing ionization potential of the halogen p orbitals, resulting in a wider experimental optical gap **[14]**.

By interacting with the B site cation at the octahedra's center and affecting the energy of the conduction band minimum, the X site halogen likewise influences the band gap. In the Cs_2SnX_6 series, the conduction band minimum is a hybrid of Sn 5s and X p states **[12-14]**, **[17**,**18]**. As the halogen p states approach the energy of the Sn 5s states, the energy of the lowest unoccupied states rises due to increased covalent interactions. This combined effect of lowering the valence band and raising the conduction band minimum contributes to the increased band gap observed with smaller halogens.

Interestingly, the change in band gap across the Cs_2SnX_6 series is more significant than in the $CsSnX_3$ perovskites **[19]**. This is because the $CsSnX_3$ compounds have valence band maxima derived from hybridized Sn 5s/halogen p states **[20]**, and the effect of incorporating smaller halogens on the valence band energy is less pronounced compared to the nonbonding halogen states in Cs_2SnX_6.

The molecular orbital theory diagrams provided in **Figure. II. 3** offer a useful tool for predicting the impact of X-site substitution on the band gap. These predictions align with experimental data and reported band alignments for various vacancy-ordered double perovskites. For instance, bromide-based vacancy-ordered double perovskites have lower ionization potentials compared to their iodide counterparts, resulting in lower energy valence band maxima and larger band gaps.

The interaction between the B-site and the halide ligands within the octahedra further influences the band gap's nature and magnitude. For example, replacing Sn with Te at the B-site in Cs_2TeI_6 leads to a larger, indirect band gap compared to Cs_2SnI_6. This is due to covalent interactions between Te 5p and I 5p states, affecting the conduction band energy while the valence band maximum remains associated with the iodine 5p states.

In summary, the band gap and optical properties of vacancy-ordered double perovskites are determined by a combination of factors, including the choice of halogen at the X site, interactions with the B site cation, and orbital character at the band edges. The trends observed in computational and experimental data are consistent with molecular orbital theory predictions and provide valuable insights into these materials' electronic structures and optical behaviors.

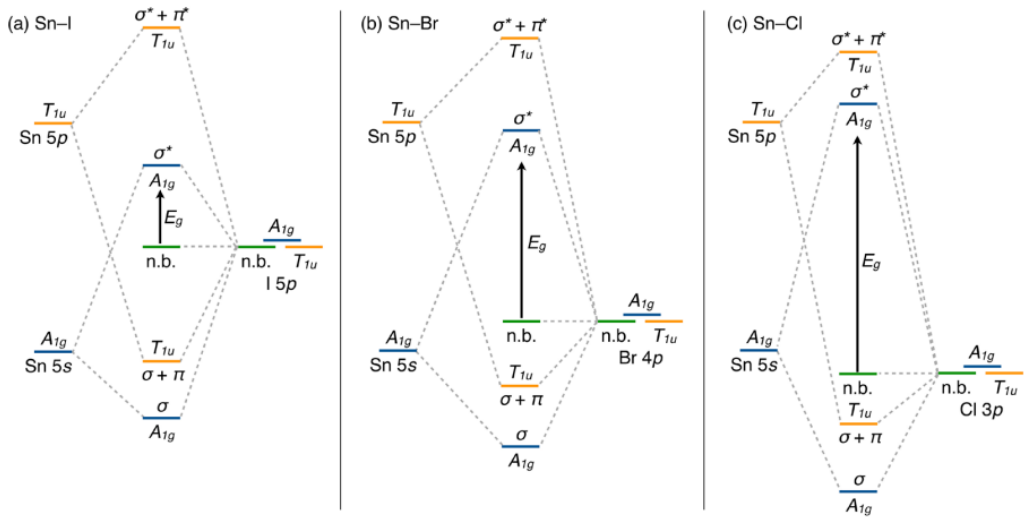

Figure. II. 3 : Molecular orbital theory perspective of the frontier states of (a) Cs_2SnI_6, (b) Cs_2SnBr_6, and (c) Cs_2SnCl_6 considering the interactions between the Sn and X orbitals **[7]**.

II.3. State of the art

II.3.1. Optoelectronic properties of VODPs

The family of inorganic vacancy-ordered double perovskites (IVODPs) has recently gained significant attention within the scientific community due to their promising band gap suitability for solar cell applications, superior stability, long carrier diffusion lengths, and versatile applications such as catalysts, alpha particle and UV detectors. The chemical formula for VODPs is generally $A_2^{+1}\,B^{+4}\,X_6^{-1}$, derived from the standard $A_2^{+1}B^{+1}\,B^{+3}\,X_6^{-1}$ double perovskite lattice by periodically incorporating vacancies at B sites **[21-23]**. The resulting A_2BX_6 lattice structure resembles a check-board pattern between vacancies and isolated BX_6 octahedra.

Vacancy-ordered double perovskites (HDPs) exhibit the potential to tailor the composition, structure, and dynamics at the A, B, and X sites, allowing for desired optical and electronic properties. The choice of X ions and the utilization of strong covalent B–X interactions enable the adjustment of the band gap. The use of large halides facilitates low carrier effective masses and potentially higher mobilities. Incorporating tetravalent ions at the B site and Cs+ at the A-site contributes to achieving the desired properties of thermodynamic stability and resistance to humidity. The tunable optical and electronic properties, coupled with

the high stability and non-toxicity of vacancy-ordered double perovskites, position them as promising candidates for use in photovoltaic applications.

Over the past few years, various research groups have explored the distinctive features of VODPs. Faizan et al. **[24]** conducted theoretical investigations on a diverse range of vacancy ordered double Perovskites (VODPs) with the formula A_2BX_6 (A = Rb, Cs; B= Sn, Pd, Pt; X = Cl, Br, I) to comprehend their structural, electronic, and optical properties. Diao et al. delved into the stability and efficiency of a series of VODPs A_2BX_6 (A = Cs, Rb; B=Ge, Zr, Sn, Hf, Se, Te, Pd; X = I, Cl, Br) **[22]**. Chen et al. provided a review of properties of various inorganic perovskites with a focus on solar cell applications **[21]**. Zhou et al. synthesized highly stable Cs_2PdX_6 (X = Br, I) perovskite nano-crystals with 1–2 unit cell thickness, showing promise for optoelectronic applications **[25]**. Sakai et al. developed a new semiconductor, Cs_2PdBr_6, for optoelectronic applications **[26]**. Han et al. reported the facile solution synthesis of high-quality stable Cs_2SnX_6 (X = Br, I) perovskite crystals for use in optoelectronic devices **[27]**. Kaltzoglou et al. investigated the optical and vibrational properties of defect perovskites Cs_2SnX_6 (X = Cl, Br, I) to study hole transport efficiency in dye-sensitized solar cells **[14]**. Ju et al. explored titanium-based Vacancy Ordered Double Perovskite (VODP) halides A_2TiI_6 (A = Cs, Rb, K, In) as promising photovoltaic materials, with a tunable band-gap in the range of 1.0–1.8 eV, employing a combination of experimental and theoretical investigations [**28]**. The study of Cs and Ti based halide VODP Cs_2TiI_6 was also reported by Zhao et al., examining their applications as ultra-high-performance photovoltaic cells and alpha particle detectors **[29,30]**. In recent years, a diverse range of Vacancy Ordered Double Perovskites (VODPs) has been extensively studied by Ali et al. and Berri et al. to explore various physical properties and potential applications in electronics, magneto-electronics, spintronics, thermoelectrics, and optoelectronics.

Recent research has shown that Cs_2PtI_6 perovskite attained the highest energy conversion efficiency of 13.88% in the field of vacancy-ordered HDP solar cells **[31]**. Scholars are presently investigating several modifications to augment the efficiency of power conversion of A_2BX_6 perovskites.

However, Due to both intrinsic and external flaws, the efficiency of photovoltaic solar cells (PSCs) using vacancy-ordered HDP materials has been comparatively inferior than that of their lead-based equivalents. Lead-free vacancy-ordered HDPs are difficult to synthesize because of their quaternary structure, limited solubility of precursors, and high annealing temperature

requirements. It is difficult to obtain high-quality HDPs in thin-film or crystal form, and limited precursor solubility remains a significant factor.

II.3.2. Thermoelectric properties of VODPs

The crystal structure and promising electronic and thermoelectric properties of vacancy-ordered double perovskites (A_2BX_6), such as Cs_2SnX_6 (X = Br, I), have garnered increased attention **[32-34]**. Notably, Cs_2SnX_6 exhibits exceptionally low lattice thermal conductivity near room temperature, with ZT values reaching 0.32 for X = Br and 0.9 for X = I **[35]**. Li et al. conducted a comprehensive computational study on A_2BX_6 and other semiconductors **[36]** , identifying 532 materials with a lattice thermal conductivity ($\kappa\iota$) of $< 2\ W.m^{-1}.K^{-1}$ out of 1171 investigated . The 'vacancy ordered' double perovskite Rb_2SnI_6, in particular, demonstrated a remarkably low $\kappa\iota$ of $0.1\ W.m^{-1}.K^{-1}$ at room temperature.

Bousahla et al. explored Pd-based vacancy-ordered double perovskites (A_2PdBr_6) and revealed their potential for optoelectronic and thermoelectric applications, showcasing a broader absorption coefficient and high Seebeck coefficient **[37]**. Additionally, Zeng and co-workers investigated the thermoelectric performance of Cs_2SnBr_6, finding an ultralow lattice thermal conductivity ($\kappa\iota$) of $0.17\ W.m^{-1}.K^{-1}$ with a glass-like heat transport mechanism through first-principles DFT calculations **[38]**.

While extensive research has focused on the thermoelectric properties of pristine materials, various strategies, including atomic doping, nanostructuring **[39,40]**, and oxygen vacancy modulation **[32]**, have been employed to modulate these properties. To advance the field of thermoelectrics, there is a need for innovative material designs, thermoelectric devices, and transport theory. Established thermoelectric materials typically have ZT values around 2 for enhanced power generation **[41,42]**, but there is a push to synthesize materials with even higher ZT values **[43]**. The ongoing search for novel thermoelectric materials, particularly halide perovskite compounds, has become a crucial research direction **[44-46]**. However, substantial efforts are required to enhance their performance and make them competitive with traditional thermoelectric materials. This pursuit demands decades of research and optimization, similar to the extensive efforts invested in traditional thermoelectric materials.

II.4. Conclusion

VODPs, with the general formula A_2BX_6, exhibit a vacancy-ordered structure derived from the conventional perovskite archetype. This structure allows for a wide range of tunability in composition, providing significant opportunities to adjust structural, compositional, and

dynamic properties. The choice of halogen at the X-site, interactions with the B-site cation, and orbital character at the band edges collectively determine the band gap and optical properties of VODPs.

The optoelectronic properties of VODPs, including their band-gap suitability for solar cell applications, superior stability, long carrier diffusion lengths, and versatility in applications such as catalysts and detectors, have attracted considerable attention. Recent studies have explored the structural, electronic, and optical properties of various VODPs, showcasing their potential in photovoltaic applications. However, challenges remain in synthesizing high-quality lead-free VODPs, and their performance in photovoltaic solar cells still lags behind lead-based counterparts.

Additionally, the thermoelectric properties of VODPs, such as their low lattice heat conductivity, which makes them excellent choices for thermoelectric uses.

Research efforts have focused on exploring materials like Cs_2SnX_6 for their exceptional thermoelectric performance, with strategies such as atomic doping and nanostructuring being employed to further enhance their properties.

While the potential of VODPs in both solar cells and thermoelectrics is evident, ongoing research and optimization efforts are crucial to address challenges and improve their performance. The pursuit of novel materials, coupled with innovative design strategies, holds the key to realizing the full potential of VODPs in sustainable and efficient energy conversion technologies.

References

[1] A. M. Glazer, "**Perovskites modern and ancient** . By Roger H. Mitchell.Thunder Bay, Ontario: AlmazPress, 2002. Price USD 70.00. ISBN0-9689411-0-9," *Acta Crystallogr B Struct Sci*, vol. 58, no. 6, pp. 1075–1075, Dec. 2002, doi: 10.1107/S0108768102020220.

[2] H. F. Kay and P. C. Bailey, "Structure and properties of CaTiO3," *Acta Cryst*, vol. 10, no. 3, pp. 219–226, Mar. 1957, doi: 10.1107/S0365110X57000675.

[3] Z. Xiao and Y. Yan, "Progress in Theoretical Study of Metal Halide Perovskite Solar Cell Materials," *Advanced Energy Materials*, vol. 7, no. 22, p. 1701136, Nov. 2017, doi: 10.1002/aenm.201701136.

[4] P. Zhang, J. Yang, and S.-H. Wei, "Manipulation of cation combinations and configurations of halide double perovskites for solar cell absorbers," *J. Mater. Chem. A*, vol. 6, no. 4, pp. 1809–1815, 2018, doi: 10.1039/C7TA09713A.

[5] G. Volonakis *et al.*, "Lead-Free Halide Double Perovskites via Heterovalent Substitution of Noble Metals," *J. Phys. Chem. Lett.*, vol. 7, no. 7, pp. 1254–1259, Apr. 2016, doi: 10.1021/acs.jpclett.6b00376.

[6] G. King and P. M. Woodward, "Cation ordering in perovskites," *J. Mater. Chem.*, vol. 20, no. 28, p. 5785, 2010, doi: 10.1039/b926757c.

[7] A. E. Maughan, A. M. Ganose, D. O. Scanlon, and J. R. Neilson, "Perspectives and Design Principles of Vacancy-Ordered Double Perovskite Halide Semiconductors," *Chem. Mater.*, vol. 31, no. 4, pp. 1184–1195, Feb. 2019, doi: 10.1021/acs.chemmater.8b05036.

[8] L. Qiao, W.-H. Fang, and R. Long, "Dopant Control of Electron–Hole Recombination in Cesium–Titanium Halide Double Perovskite by Time Domain Ab Initio Simulation: Codoping Supersedes Monodoping," *J. Phys. Chem. Lett.*, vol. 9, no. 23, pp. 6907–6914, Dec. 2018, doi: 10.1021/acs.jpclett.8b03356.

[9] M. Deepa, M. Salado, L. Calio, S. Kazim, S. M. Shivaprasad, and S. Ahmad, "Cesium power: low Cs^{+} levels impart stability to perovskite solar cells," *Phys. Chem. Chem. Phys.*, vol. 19, no. 5, pp. 4069–4077, 2017, doi: 10.1039/C6CP08022G.

[10] J. Lee, D. Kim, H. Kim, S. Seo, S. M. Cho, and N. Park, "Formamidinium and Cesium Hybridization for Photo- and Moisture-Stable Perovskite Solar Cell," *Advanced Energy Materials*, vol. 5, no. 20, p. 1501310, Oct. 2015, doi: 10.1002/aenm.201501310.

[11] Y. Cai *et al.*, "Computational Study of Halide Perovskite-Derived A_2BX_6 Inorganic Compounds: Chemical Trends in Electronic Structure and Structural Stability," *Chem. Mater.*, vol. 29, no. 18, pp. 7740–7749, Sep. 2017, doi: 10.1021/acs.chemmater.7b02013.

[12] B. Lee *et al.*, "Air-Stable Molecular Semiconducting Iodosalts for Solar Cell Applications: Cs_2SnI_6 as a Hole Conductor," *J. Am. Chem. Soc.*, vol. 136, no. 43, pp. 15379–15385, Oct. 2014, doi: 10.1021/ja508464w.

[13] A. E. Maughan, A. M. Ganose, M. M. Bordelon, E. M. Miller, D. O. Scanlon, and J. R. Neilson, "Defect Tolerance to Intolerance in the Vacancy-Ordered Double Perovskite Semiconductors Cs_2SnI_6 and Cs_2TeI_6," *J. Am. Chem. Soc.*, vol. 138, no. 27, pp. 8453–8464, Jul. 2016, doi: 10.1021/jacs.6b03207.

[14] A. Kaltzoglou *et al.*, "Optical-Vibrational Properties of the Cs_2SnX_6 (X = Cl, Br, I) Defect Perovskites and Hole-Transport Efficiency in Dye-Sensitized Solar Cells," *J. Phys. Chem. C*, vol. 120, no. 22, pp. 11777–11785, Jun. 2016, doi: 10.1021/acs.jpcc.6b02175.

[15] H.-M. Huang, Z.-Y. Jiang, and S.-J. Luo, "First-principles investigations on the mechanical, thermal, electronic, and optical properties of the defect perovskites $Cs_2Sn\mathit{X}_6$ (X = Cl, Br, I)," *Chinese Phys. B*, vol. 26, no. 9, p. 096301, Aug. 2017, doi: 10.1088/1674-1056/26/9/096301.

[16] B. Lee, A. Krenselewski, S. I. Baik, D. N. Seidman, and R. P. H. Chang, "Solution processing of air-stable molecular semiconducting iodosalts, $Cs_2SnI_{6-x}Br_x$, for potential solar cell applications," *Sustainable Energy Fuels*, vol. 1, no. 4, pp. 710–724, 2017, doi: 10.1039/C7SE00100B.

[17] A. E. Maughan, A. M. Ganose, M. A. Almaker, D. O. Scanlon, and J. R. Neilson, "Tolerance Factor and Cooperative Tilting Effects in Vacancy-Ordered Double Perovskite Halides," *Chem. Mater.*, vol. 30, no. 11, pp. 3909–3919, Jun. 2018, doi: 10.1021/acs.chemmater.8b01549.

[18] A. E. Maughan, A. M. Ganose, A. M. Candia, J. T. Granger, D. O. Scanlon, and J. R. Neilson, "Anharmonicity and Octahedral Tilting in Hybrid Vacancy-Ordered Double Perovskites," *Chem. Mater.*, vol. 30, no. 2, pp. 472–483, Jan. 2018, doi: 10.1021/acs.chemmater.7b04516.

[19] G. M. Dalpian *et al.*, "Changes in charge density vs changes in formal oxidation states: The case of Sn halide perovskites and their ordered vacancy analogues," *Phys. Rev. Materials*, vol. 1, no. 2, p. 025401, Jul. 2017, doi: 10.1103/PhysRevMaterials.1.025401.

[20] L. Huang and W. R. L. Lambrecht, "Electronic band structure, phonons, and exciton binding energies of halide perovskites CsSnCl 3 , CsSnBr 3 , and CsSnI 3," *Phys. Rev. B*, vol. 88, no. 16, p. 165203, Oct. 2013, doi: 10.1103/PhysRevB.88.165203.

[21] H. Chen, S. Xiang, W. Li, H. Liu, L. Zhu, and S. Yang, "Inorganic Perovskite Solar Cells: A Rapidly Growing Field," *Solar RRL*, vol. 2, no. 2, p. 1700188, Feb. 2018, doi: 10.1002/solr.201700188.

[22] X. Diao *et al.*, "High-throughput screening of stable and efficient double inorganic halide perovskite materials by DFT," *Sci Rep*, vol. 12, no. 1, p. 12633, Jul. 2022, doi: 10.1038/s41598-022-16221-3.

[23] X. Ye *et al.*, "Computational screening of Cs based VACANCY-ORDERED double perovskites for solar cell and photocatalysis applications," *EcoMat*, vol. 5, no. 3, p. e12295, Mar. 2023, doi: 10.1002/eom2.12295.

[24] M. Faizan *et al.*, "Electronic and optical properties of vacancy ordered double perovskites A2BX6 (A = Rb, Cs; B = Sn, Pd, Pt; and X = Cl, Br, I): a first principles study," *Sci Rep*, vol. 11, no. 1, p. 6965, Mar. 2021, doi: 10.1038/s41598-021-86145-x.

[25] L. Zhou *et al.*, "All-Inorganic Lead-Free Cs_2PdX_6 (X = Br, I) Perovskite Nanocrystals with Single Unit Cell Thickness and High Stability," *ACS Energy Lett.*, vol. 3, no. 10, pp. 2613–2619, Oct. 2018, doi: 10.1021/acsenergylett.8b01770.

[26] N. Sakai *et al.*, "Solution-Processed Cesium Hexabromopalladate(IV), Cs_2PdBr_6, for Optoelectronic Applications," *J. Am. Chem. Soc.*, vol. 139, no. 17, pp. 6030–6033, May 2017, doi: 10.1021/jacs.6b13258.

[27] X. Han *et al.*, "Lead-Free Double Perovskite Cs_2SnX_6: Facile Solution Synthesis and Excellent Stability," *Small*, vol. 15, no. 39, p. 1901650, Sep. 2019, doi: 10.1002/smll.201901650.

[28] M.-G. Ju *et al.*, "Earth-Abundant Nontoxic Titanium(IV)-based Vacancy-Ordered Double Perovskite Halides with Tunable 1.0 to 1.8 eV Bandgaps for Photovoltaic Applications," *ACS Energy Lett.*, vol. 3, no. 2, pp. 297–304, Feb. 2018, doi: 10.1021/acsenergylett.7b01167.

[29] P. Zhao *et al.*, "A new all-inorganic vacancy-ordered double perovskite Cs2CrI6 for high-performance photovoltaic cells and alpha-particle detection in space environment," *Materials Today Physics*, vol. 20, p. 100446, Sep. 2021, doi: 10.1016/j.mtphys.2021.100446.

[30] P. Zhao *et al.*, "Cs2TiI6: A potential lead-free all-inorganic perovskite material for ultrahigh-performance photovoltaic cells and alpha-particle detection," *Nano Res.*, vol. 15, no. 3, pp. 2697–2705, Mar. 2022, doi: 10.1007/s12274-021-3801-5.

[31] D. Schwartz *et al.*, "Air Stable, High-Efficiency, Pt-Based Halide Perovskite Solar Cells with Long Carrier Lifetimes," *Physica Rapid Research Ltrs*, vol. 14, no. 8, p. 2000182, Aug. 2020, doi: 10.1002/pssr.202000182.

[32] X. Feng *et al.*, "Graphene promoted oxygen vacancies in perovskite for enhanced thermoelectric properties," *Carbon*, vol. 112, pp. 169–176, Feb. 2017, doi: 10.1016/j.carbon.2016.11.012.

[33] M. M. AL-Anazy *et al.*, "Study of optoelectronic and thermoelectric properties of double perovskites for renewable energy," *Phys. Scr.*, vol. 96, no. 12, p. 125828, Dec. 2021, doi: 10.1088/1402-4896/ac297a.

[34] H. Albalawi *et al.*, "Study of optical and thermoelectric properties of double perovskites Cs2KTlX6 (X = Cl, Br, I) for solar cell and energy harvesting," *Materials Today Communications*, vol. 32, p. 104083, Aug. 2022, doi: 10.1016/j.mtcomm.2022.104083.

[35] M. Fallah and H. Milani Moghaddam, "Ultra-low lattice thermal conductivity and high thermoelectric efficiency in Cs2SnX6 (X=Br, I): A DFT study," *Materials Science in Semiconductor Processing*, vol. 133, p. 105984, Oct. 2021, doi: 10.1016/j.mssp.2021.105984.

[36] J. Li, W. Hu, and J. Yang, "High-Throughput Screening of Rattling-Induced Ultralow Lattice Thermal Conductivity in Semiconductors," *J. Am. Chem. Soc.*, vol. 144, no. 10, pp. 4448–4456, Mar. 2022, doi: 10.1021/jacs.1c11887.

[37] M. A. Bousahla *et al.*, "DFT study on the crystal structure, optoelectronic, and thermoelectric properties of lead-free inorganic A2PdBr6 (A = K, Rb, and Cs) perovskites," *Materials Today Communications*, vol. 30, p. 103061, Mar. 2022, doi: 10.1016/j.mtcomm.2021.103061.

[38] X. Zeng *et al.*, "Physical Insights on the Thermoelectric Performance of Cs_2SnBr_6 with Ultralow Lattice Thermal Conductivity," *J. Phys. Chem. Lett.*, vol. 13, no. 41, pp. 9736–9744, Oct. 2022, doi: 10.1021/acs.jpclett.2c02350.

[39] H. Wu *et al.*, "Ni doping and rational annealing boost thermoelectric performance of nanostructured double perovskite Pr1.8Sr0.2CoFeO6," *Applied Materials Today*, vol. 29, p. 101580, Dec. 2022, doi: 10.1016/j.apmt.2022.101580.

[40] T. Wu, X. Shi, W. Liu, S. Sun, Q. Liu, and Z. Chen, "Dual Post-Treatments Boost Thermoelectric Performance of PEDOT:PSS Films and Their Devices," *Macro Materials & Eng*, vol. 307, no. 12, p. 2200411, Dec. 2022, doi: 10.1002/mame.202200411.

[41] K. F. Hsu *et al.*, "Cubic AgPb $_m$ SbTe $_{2+m}$: Bulk Thermoelectric Materials with High Figure of Merit," *Science*, vol. 303, no. 5659, pp. 818–821, Feb. 2004, doi: 10.1126/science.1092963.

[42] F. J. DiSalvo, "Thermoelectric Cooling and Power Generation," *Science*, vol. 285, no. 5428, pp. 703–706, Jul. 1999, doi: 10.1126/science.285.5428.703.

[43] B. Poudel *et al.*, "High-Thermoelectric Performance of Nanostructured Bismuth Antimony Telluride Bulk Alloys," *Science*, vol. 320, no. 5876, pp. 634–638, May 2008, doi: 10.1126/science.1156446.

[44] Y. Jung, W. Lee, S. Han, B. Kim, S. Yoo, and H. Jang, "Thermal Transport Properties of Phonons in Halide Perovskites," *Advanced Materials*, vol. 35, no. 43, p. 2204872, Oct. 2023, doi: 10.1002/adma.202204872.

[45] X. Mettan *et al.*, "Tuning of the Thermoelectric Figure of Merit of $CH_3NH_3MI_3$ (M═Pb,Sn) Photovoltaic Perovskites," *J. Phys. Chem. C*, vol. 119, no. 21, pp. 11506–11510, May 2015, doi: 10.1021/acs.jpcc.5b03939.

[46] A. Van Roekeghem, J. Carrete, C. Oses, S. Curtarolo, and N. Mingo, "High-Throughput Computation of Thermal Conductivity of High-Temperature Solid Phases: The Case of Oxide and Fluoride Perovskites," *Phys. Rev. X*, vol. 6, no. 4, p. 041061, Dec. 2016, doi: 10.1103/PhysRevX.6.041061.

Chapter III :

Density Functional Theory (DFT) and FP-LAPW method

III.1. Introduction

An explanation of many-electrons systems' behavior and structure is one of the fundamental issues in theoretical chemistry and physics. Density Functional Theory is one of the most popular and effective quantum mechanical approaches to describe matter in use today. It can be used to nuclei, molecules, solids, atoms, and both quantum and classical fluids. These days, DFT is frequently used to calculate a wide range of features in physics and chemistry, such as solids' band structures and molecular structures and reaction pathways.

III.2. Many body Schrödinger equation

The solution of the time-independent, non-relativistic Schrödinger equation is the ultimate aim of the majority of methods used in solid-state physics and quantum chemistry in order to obtain all available information of system.

Consider a system of N particles interacting with each other via Coulomb potential. The Schrödinger equation for it is:

$$\mathbf{H\Psi = E\Psi} \tag{III-1}$$

Where:

- The many body wave function, denoted by **Ψ**, is dependent on the locations of every electron and nucleus within the system. For N electrons and M nuclei, we have: for N electrons with coordinates $\overrightarrow{r_1}, \overrightarrow{r_2}, \dots, \overrightarrow{r_3}$and M nuclei with coordinates, $\overrightarrow{R_1}, \overrightarrow{R_2}, \dots, \overrightarrow{R_M}$ we have:

$$\Psi = \Psi\left(\overrightarrow{r_1}, \overrightarrow{r_2}, \dots, \overrightarrow{r_N};\ \overrightarrow{R_1}, \overrightarrow{R_2}, \dots, \overrightarrow{R_M}\right) \tag{III-2}$$

- **E** : the system's total energy in the designated quantum state Ψ.
- **H** : the Hamiltonian operator of the system :

$$\boldsymbol{H = T_e + T_n + U_{e-e} + U_{n-n} + U_{e-n}} \tag{III-3}$$

1. T_e is the kinetic energy of electrons:

$$T_e = \sum_{i=1}^{N} \frac{{P_i}^2}{2m_e} = \sum_{i=1}^{N} \frac{-\hbar^2}{2m_e} \Delta_i \tag{III-4}$$

2. T_n is the kinetic energy of nuclei:

$$T_n = \sum_{i=1}^{M} \frac{{P_i}^2}{2m_n} = \sum_{i=1}^{M} \frac{-\hbar^2}{2m_n} \Delta_i \quad \text{(III-5)}$$

3. U_{e-e} is the Coulomb interaction of electrons:

$$U_{e-e} = \frac{1}{2} \cdot \frac{1}{4\pi\varepsilon_0} \sum_{i \neq j}^{N} \frac{e^2}{|\vec{r_i} - \vec{r_j}|} \quad \text{(III-6)}$$

4. U_{n-n} is the Coulomb interaction of nuclei:

$$U_{n-n} = \frac{1}{2} \cdot \frac{1}{4\pi\varepsilon_0} \sum_{\alpha \neq \beta}^{M} \frac{Z_\alpha Z_\beta e^2}{|\vec{R_\alpha} - \vec{R_\beta}|} \quad \text{(III-7)}$$

5. U_{e-n} is the Coulombien interaction between electrons and nuclei:

$$U_{e-n} = -\frac{1}{4\pi\varepsilon_0} \sum_{i,\alpha}^{N,M} \frac{Z_\alpha e^2}{|\vec{r_i} - \vec{R_\alpha}|} \quad \text{(III-8)}$$

$\overrightarrow{\boldsymbol{r_i}}$: electrons coordinates

$\overrightarrow{\boldsymbol{R_\alpha}}$: nuclei coordinates

III.3. Born-Oppenheimer approximation (clamped nuclei approximation)

As it stands, the resolution of Schrödinger equation, which is partial differential equation, poses an exceedingly complicated technical problem.

The nuclei in solids usually stay in or close to specific locations. As a result, we can presume that the nuclei are kept stationary (clamped) in predetermined locations. This option suggests that the Coulomb repulsion between nuclei is just a constant and that we can ignore the kinetic energy of the nuclei in equation (III-3). By an adequate choice of the potential reference we have $U_{n-n} = 0$.

Hence, the standard first step towards a solution of equation (III-1) is a partial decoupling of the electrons from the nuclear motion.

So that we can break up the many-electron Hamiltonien as fallows:

$$\mathrm{H}_e \Psi_e = \mathrm{E}_e \Psi_e \quad \text{(III-9)}$$

$$H_e = T_e + U_{e-e} + U_{e-n} \quad \text{(III-10)}$$

This is archived by the **Born-Oppenheimer** approximation **[1]** .

III.4. Independent electrons approximation (Mean field approximation)

We state that each individual electron is said to move independently of the others, perceiving only the average electric field generated by the nucleus and all of the other electrons.

Stated differently, this is the potential resulting from the ionic lattice and electron density distribution, excluding the effects of exchange and correlation. Hence, every electron engages with the crystal separately from the others.

The multi-electronic wave function (N electrons) Ψ_e is simply the product of the N single-electron wave function ϕ_i:

$$\boldsymbol{\Psi_e(\overrightarrow{r_1}, \overrightarrow{r_2}, \dots, \overrightarrow{r_N}) = \phi_1(\overrightarrow{r_1}).\phi_2(\overrightarrow{r_2}) \dots \dots \dots .\phi_N(\overrightarrow{r_N})} \quad \text{(III-11)}$$

III.4.1.Hartree potential

A distribution of electronic charge generates an electrostatic potential $\Phi(\vec{r})$ through Poisson's equation (Jackson, 1998):

$$\Delta\Phi(\vec{r}) = 4\pi\,\rho(\vec{r}) \quad \text{(III-12)}$$

The electrons immersed in this electrostatic potential have a potential energy

$$U_H(\vec{r}) = -e\Phi(\vec{r}) \quad \text{(III-13)}$$

Which is called the "Hartree potential" **[2].**

The formal solution of this equation is:

$$U_H = -e\int \frac{\rho(\overrightarrow{r'})}{|\vec{r}-\overrightarrow{r'}|}d\vec{r}' \quad \text{(III-14)}$$

$$\rho(\vec{r}) = \sum_j \phi_j^*(\vec{r})\,.\,\phi_j(\vec{r}) \quad \text{(III-15)}$$

Since the potential U_H is the 'average' potential experienced by each electron, we call this approach the **"mean-field approximation"**.

III.4.2. Schrödinger equation of a single electron

Thus, the electronic Hamiltonian of equation (III-9) becomes:

$$H_e = \sum_{i=1}^{N}\left(\frac{-\hbar^2}{2m}\Delta_i\right) + \sum_{i=1}^{N} U_H(\overrightarrow{r_i}) + \sum_{i=1}^{N}(\sum_{\alpha=1}^{M} U_{i\alpha}) \quad \text{(III-16)}$$

$$U_{i\alpha} = \frac{\boldsymbol{Z_\alpha e^2}}{|\overrightarrow{r_i}-\overrightarrow{R_\alpha}|} \quad \text{(III-17)}$$

Thus,

$$H_e = \sum_{i=1}^{N} H_i \quad \text{(III-18)}$$

$$H_i = \left(\frac{-\hbar^2}{2m}\Delta_i\right) + U_H(\vec{r_i}) + U_i(\vec{r_i}) \quad \text{(III-19)}$$

With:

$$U_i = \sum_{\alpha=1}^{M} U_{i\alpha} \quad \text{(III-20)}$$

So the wave function of each electron is solution of the equation:

$$\left[\frac{-\hbar^2}{2m}\Delta_i + U_n(\vec{r_i}) + U_H(\vec{r_i})\right]\phi_i = \varepsilon_i\phi_i(\vec{r}) \quad \text{(III-21)}$$

III.5. Hartree-Fock approximation

The description in the Hartree approach is incomplete. In fact, electrons are not independent. Hartree – Fock approximation takes into account the exchange interaction.

Exclusion principle (Slater Determinant)

The Pauli's exclusion principle states that, since electrons are 'fermions', the many-body wave function,ψ, must change sign if we exchange the variables of any two electrons, so, the wave function of the system can not be a simple product of the single wave functions (anti symmetricity of the wave function). This principle is equivalent to the statement that no two electrons can occupy the same electronic state **[3]**.

Hence, Hartree-Fock approximation, which defines the wave function as a "Slater determinant" (anti symmetric product of single electronic Hartree functions):

$$\Psi(\overrightarrow{r_1}\,\overrightarrow{\sigma_1}, \overrightarrow{r_2}\,\overrightarrow{\sigma_2}, \dots, \overrightarrow{r_N}\,\overrightarrow{\sigma_N}) = \frac{1}{\sqrt{N!}}\begin{vmatrix} \phi_1(\overrightarrow{r_1}\,\overrightarrow{\sigma_1}) & \phi_1(\overrightarrow{r_2}\,\overrightarrow{\sigma_2}) & \dots\dots\dots & \phi_1(\overrightarrow{r_N}\,\overrightarrow{\sigma_N}) \\ \phi_2(\overrightarrow{r_1}\,\overrightarrow{\sigma_1}) & \phi_2(\overrightarrow{r_2}\,\overrightarrow{\sigma_2}) & \dots\dots\dots & \phi_2(\overrightarrow{r_N}\,\overrightarrow{\sigma_N}) \\ \vdots & \vdots & \vdots & \vdots \\ \phi_N(\overrightarrow{r_1}\,\overrightarrow{\sigma_1}) & \phi_N(\overrightarrow{r_2}\,\overrightarrow{\sigma_2}) & \dots\dots\dots & \phi_N(\overrightarrow{r_N}\,\overrightarrow{\sigma_N}) \end{vmatrix} \quad \text{(III-22)}$$

ϕ_i : single electron wave function

N : electrons number

$\overrightarrow{\sigma_i}$: electrons spin

$\overrightarrow{r_i}$: electrons coordinate

Using a "variational principle", Fock obtains the so-called Hartree-Fock equations:

$$\left[\frac{-\hbar^2}{2m}\Delta_i + U_n(\overrightarrow{r_i}) + U_H(\overrightarrow{r_i})\right]\phi_i + \int \boldsymbol{d\vec{r}'}\, \boldsymbol{V_X}(\vec{\boldsymbol{r}}, \vec{\boldsymbol{r}}')\boldsymbol{\phi_i}(\vec{\boldsymbol{r}}') = \varepsilon_i \phi_i(\vec{r}) \qquad \text{(III-23)}$$

$$V_X(\vec{r}, \vec{r}') = -\sum_j \frac{\phi_j^*(\vec{r}').\phi_j(\vec{r})}{\left|\vec{r}-\overrightarrow{r'}\right|} \qquad \text{(III-24)}$$

The application of this approximation (Hartree-Fock approximation) leads to good results. However, it always gives an upper bound to energy. It does not take into account the effects of electronic correlations. Processing large systems, such as solids, remains difficult. An attempt to its improvement by including correlation effects made it extremely expensive in computation by depending on the number of electrons. Despite everything, this Hartree-Fock method remains an essential benchmark.

III.6. Differential functional theory (DFT)

We have observed that the challenge of finding the quantum states of a system with N electrons is very complicated since the many-body wave function $\Psi(\overrightarrow{r_1}, \overrightarrow{r_2}, \cdots, \overrightarrow{r_N})$ involves 3N

The fundamental principle of DFT consists in describing an interacting electronic system by its **density** and not by its wave function. This idea finds its origin mainly in Thomas **[3]** and Fermi **[4]** works, but it has not given any proof until 1964, by the two theorems of Hohenberg and Kohn **[5]** which connect a whole system with N electrons evolving in an external potential V_{ext} to the electrons density of the real system.

III.6.1.Thomas-Fermi theory

Just after the publication of the original Schrödinger article, Thomas **[3]** and Fermi **[4]** suggested an alternate approach to solving the Schrödinger equation in 1928, based solely on the electronic density. This approach makes the assumption that there is no correlation between the electrons' movements and that the energy kinetics may be adequately represented by a local approximation based on findings from the situation of free electrons. . A little later,

Dirac **[6]** proposed to take into account exchange effects by incorporating a term from the exchange energy density into a homogeneous gas of electrons. This method has been successfully applied in the field of physics plasma, although it was rudimentary and did not allow the study of molecules.

III.6.2.Hohenberg-Kohn theorems [5]

The approach developed by Pierre Hohenberg and Walter Kohn allowed for the reformulation of the density functional theory proposed by Thomas and Fermi into an exact theory for a many-body system. The reformulation is applicable to any system of interacting particles evolving in an external potential. It is based on two essential theorems that were stated and proven by Hohenberg and Kohn in their 1964 article.

Theorem 1:

"*The total energy of the ground state E_0 is a single functional of the density of particles $\rho(\vec{r})$ for a given external potential V_{ext} (r)".* (1964)

A unique relationship between the electron density and the external potential is shown by this first theorem. The wave function and, thus, the system's electrical characteristics are then uniquely determined by it.

. Thus, for a given system, the total energy is written as following:

$$E[\rho] = T[\rho] + E_{ee}[\rho] + E_{Ne}[\rho] = F_{HK}[\rho] + \int \rho(\vec{r}) V_{Ne}(\vec{r}) d\vec{r} \qquad \text{(III-25)}$$

$$F_{HK}[\rho] = T[\rho] + E_{ee}[\rho] \qquad \text{(III-26)}$$

$T:$ kinetic energy

$V_{Ne}:$ potential of nuclei

E_{ee}: electron-electron interaction

The ultimate goal in density functional theory is to find the functional $F_{HK}[\rho]$. Actually, we would have precisely solved the Schrödinger equation if we had known.

Theorem 2:

"The ground state density ρ_0 is precisely the function that minimizes the total energy E".

$$\left.\frac{\partial E}{\partial \rho}\right|_{\rho_0} = 0 \qquad \text{(III-27)}$$

With these two theorems proposed by Hohenberg and Kohn, the problem posed by the solution of the multielectronic Schrödinger equation is shifted. Instead of trying to get a good approximation on the wave function of the ground state of the system, we seek to express the energy of the system as a functional of the density, without worrying about the function wave, unlike the Hartree-Fock method for which the initial knowledge of the the system's wave function is needed to assess its physical or chemical properties.

Therefore, in principle, knowing the charge density, we can deduce V_{ext} (r) and determine the operator Hamiltonian and through this operator, all the properties of the ground state of the system, in particular its energy and therefore all the associated derived quantities can be calculated.

The problem which arises is then the formulation of the functional $F_{HK}[\rho]$ and in particular the kinetic energy expression $T[\rho]$. Indeed, it is not possible, for a multi-electronic system in interaction, to find an analytical expression for the function of kinetic energy. Strong fortunately, we know how to write it very well, in the absence of interaction.

III.6.3.Kohn-Sham equations

The solution of that problem was found by Walter Kohn and Lu Sham thought in 1965 **[7]**. In fact, they got around the problem by replacing the system of N-electrons in interaction, impossible to solve analytically, by an auxiliary system whose kinetic energy is explicitly calculable. For this, they imagined a model system of N fermions without interactions, evolving in an **effective potential**, which makes it possible to guarantee that the system has, in the ground state, the same density as the real system of electrons. These fermions have the same spin as electrons and respect the Pauli Exclusion Principle. However, by eliminating interaction, each fermion can be treated independently, which allows to reduce the question to a single body problem. The kinetic energy of this fictitious system differs from that of the real system, but has the advantage of being able to be expressed itself directly from orbitals, $\phi i\,(r)$, that we can directly relate to density:

$$T_s = \frac{\hbar^2}{2m}\sum_{i=1}^{N}\langle\phi_i|\Delta|\phi_i\rangle \qquad \text{(III-28a)}$$

$$\rho_s(\vec{r}) = \sum_{i=1}^{N}\sum_s|\phi_i(\vec{r},s)| = \rho(\vec{r}) \qquad \text{(III-28b)}$$

Where: ϕ_i are the orbitals of the non-interacting system. Undoubtedly, T_S is not equal to the true kinetic energy of the real system. Kohn and Sham accounted for that by introducing the following separation of the functional $F_{KS}[\rho]$

$$F_{KS}[\rho] = T_s[\rho] + E_S[\rho] \quad \text{(III-29)}$$

To guarantee an equal density between the real system and the model (fictitious system), the effective potential should be chosen as follows:

$$\boldsymbol{E_s = E_{ee}[\rho] + (T[\rho] - T_s[\rho])} \quad \text{(III-30)}$$

This reformulation makes it possible to define a single electronic Hamiltonian and to write the equations of single electronic Kohn-Sham that can be digitally solved:

$$H_s = \sum_{i=1}^{N} h_s(\vec{r_i}) = \sum_{i=1}^{N} \left(-\frac{\hbar^2}{2m}\Delta_i + V_{eff}(\vec{r_i}) \right) \quad \text{(III-31)}$$

This Hamiltonian presents, for solution, a Slater determinant $\boldsymbol{\Psi_S}$ (III-22). Orbitals molecules in this determinant are obtained after solving the equation:

$$h_s(\vec{r_i})\phi_i(\vec{r}) = \left(-\frac{\hbar^2}{2m}\Delta_i + V_{eff}(\vec{r_i}) \right)\phi_i(\vec{r}) = \varepsilon_i \phi_i(\vec{r}) \quad \text{(III-32)}$$

These orbitals, in turn, determine the value of the kinetic energy functional without interaction $\boldsymbol{T_s[\rho]}$ of equation (III-28a) and the density of equation (II-28b). This density is the same as that of the original multi-electronic system

$$\boldsymbol{V_{eff}(\vec{r}) = V_{ext}(\vec{r}) + V_H[\rho(\vec{r})] + V_{XC}[\rho(\vec{r})]} \quad \text{(III-33)}$$

The second term, commonly known as the Hartree potential $\boldsymbol{V_H}$, expresses the conventional Coulomb interaction between a two of electrons, where $\boldsymbol{V_{ext}}$ is the exterior potential generated by nuclei. The exchange-correlation potential, or $\boldsymbol{V_{XC}}$, is the final term and includes the kinetic energy corrections $(\boldsymbol{T[\rho] - T_s[\rho]})$. $\boldsymbol{V_{XC}}$is the only term for which there isn't an explicit form available.The electron density, which is determined from the wave functions of independent fermions, which in turn depend on the potential determined from the density, etc., is what determines the potential of equation (III-32). This method produces what is known as a "self-consistent field (SCF)" processing, also termed the self-consistent field method.

III.6.4.Numerical resolution of Kohn-Sham equations

The Kohn-Sham equations represent a set of single electronic Schrödinger equations. They can be solved numerically using an iterative process, in a self-coherent manner (**Figure. III. 1**). The self-coherent cycle is initialized by an arbitrary starting density value ρ_{in} to calculate the various density functional. This allows us to find the value of the effective potential V_{eff} using equation (III-33). We then solve the single electronic system of equations

(III-32). The solutions allow to obtain a new value of the density. The processing cycle is repeated until the convergence of the various calculated quantities.

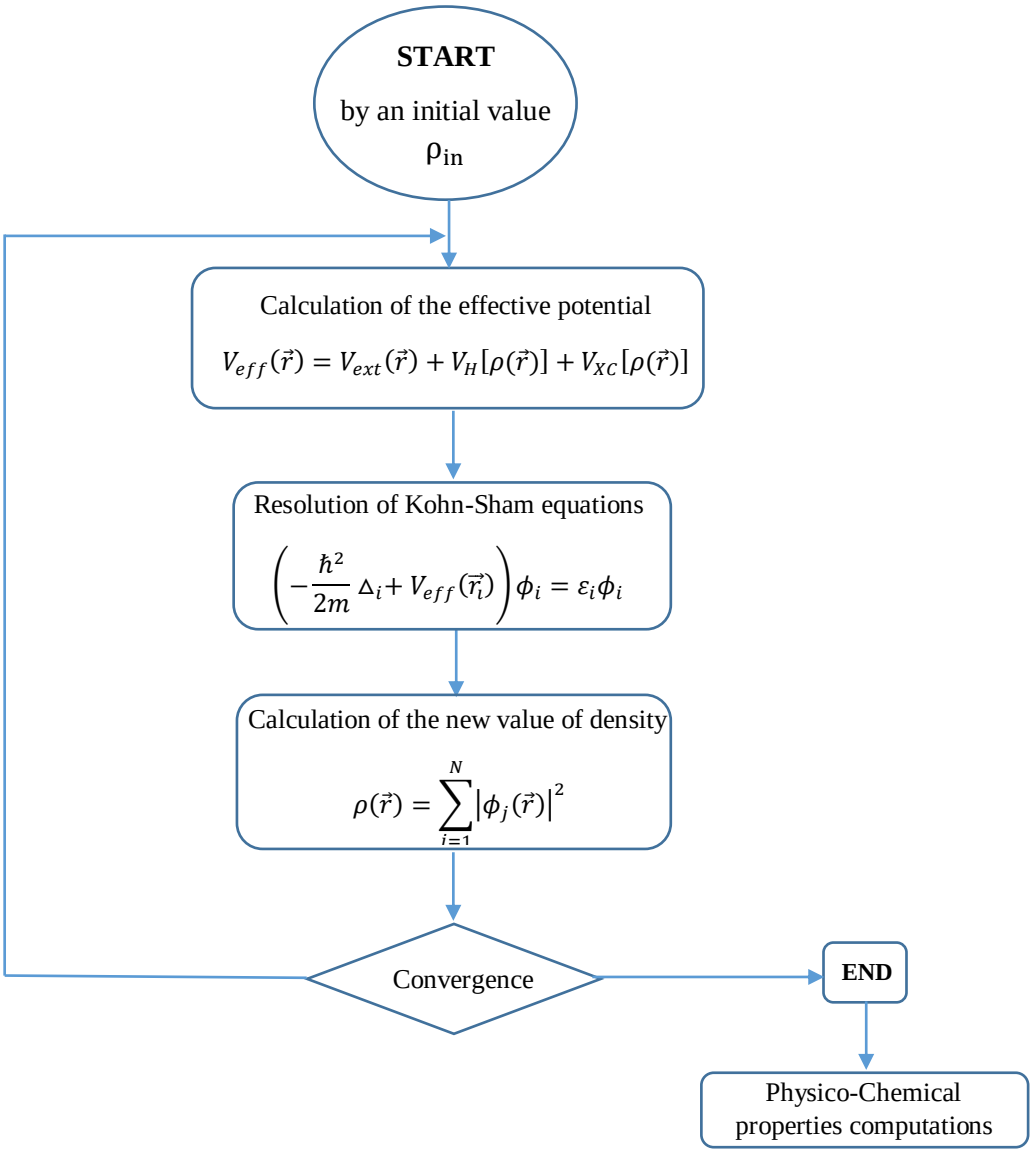

Figure. III. 1: Diagram describing the iterative process (SCF) for solving Kohn-Sham equations

III.7. Exchange – correlation potential

To solve the Kohn and Sham equations various exchange -correlation functional were considered.

III.7.1.Local density approximation LDA

The local density approximation assumes that the electron density can be processed locally as a uniform electron gas. In other words, this approach consists of making the following two assumptions:

1- The exchange-correlation effects are dominated by the density at point $\vec{r}$.

2- The density $\rho(\vec{r})$ is a function varying slowly with $\vec{r}$.

Thus, the fundamental hypothesis contained in the formalism of the LDA consists in considering that the contribution of $\varepsilon_{XC}^{LDA}[\rho]$ to the total energy of the system can be added in a cumulative manner from each portion of the non-uniform gas as if it were locally uniform.

The LDA exchange-correlation functional assumes that the exchange-correlation part of the total energy of the fundamental state of the electronic system can be written according to the expression:

$$E_{XC}^{LDA}[\rho] = \int \rho(\vec{r})\, \varepsilon_{XC}[\rho(\vec{r})] d\vec{r} \qquad \text{(III-34)}$$

in which $\varepsilon_{XC}[\rho(\vec{r})]$ represents the exchange-correlation energy per electron in a system of interacting electrons of uniform density $\rho(\vec{r})$.

The quantity $\varepsilon_{XC}[\rho(\vec{r})]$ can be further split into exchange and correlation contributions

$$\varepsilon_{XC}[\rho(\vec{r})] = \varepsilon_X[\rho(\vec{r})] + \varepsilon_C[\rho(\vec{r})] \qquad \text{(III-35)}$$

In this case, the form of exchange energy is exactly known:

$$\varepsilon_X = -\frac{3}{4}\left(\frac{3}{\pi}\right)^{\frac{1}{3}}\left(\rho(\vec{r})\right)^{\frac{4}{3}} \quad \text{(III-36)}$$

The total exchange energy in a volume Ω :

$$E_x^{LDA}[\rho(\vec{r})] = -\frac{3}{4}\left(\frac{3}{\pi}\right)^{\frac{1}{3}}\int_{(\Omega)}\left(\rho(\vec{r})\right)^{\frac{4}{3}}d\vec{r} \quad \text{(III-37)}$$

$$E_x^{LDA} = -\frac{3}{4}\left(\frac{3}{\pi}\right)^{\frac{1}{3}}\rho^{\frac{4}{3}}\,\Omega \quad \text{(III-38)}$$

An exact solution for the correlation energy of uniform gas is not known, but we know approximations for low and high electron densities. The correlation contribution was first estimated by Wigner **[8]**, then corrected by a quantum Monte-Carlo simulation by authors such as CEPERLEY **[9]** and more recently BECCA and SORELLA **[10]**. The search for analytical functions that come as close as possible to experimental results leads to the development of various functional with different degrees of success.

Since real systems are far from the model of a homogeneous electron gas, the LDA approximation only works well enough where the charge density varies slowly; the case of covalent systems and simple metals.

On the other hand, it has a bad asymptotic behavior which leads to a bad description of the ionic systems and an erroneous description of dissociations. It doesn't work also for strongly localized electrons (d and f). The improvements of the LDA approach must consider the electron gas in its real form, which is non-uniform and non-local. The GGA, meta-GGA and hybrids approximations allow us to gradually approach the consideration of these two effects.

III.7.2.Approximation of the local spin-polarized density (LSDA)

The generalization of the LDA is extended to the LSDA to support systems with polarized magnetization. For these systems, the electron density $\boldsymbol{\rho}(\vec{\boldsymbol{r}})$ can be split into two spin densities: up and down (Equation III-39) **[11,12]** and a new variable can be defined: the magnetization density $\boldsymbol{m}(\vec{\boldsymbol{r}})$ (Equation III-40) **[13]**.

The exchange-correlation energy, and therefore the total energy becomes functional of the two spin densities (Equations. (III-41) and (III-42))

$$\boldsymbol{\rho}(\vec{\boldsymbol{r}}) = \boldsymbol{\rho}_{\uparrow}(\vec{\boldsymbol{r}}) + \boldsymbol{\rho}_{\downarrow}(\vec{\boldsymbol{r}}) \quad \text{(III-39)}$$

$$\boldsymbol{m}(\vec{\boldsymbol{r}}) = \boldsymbol{\rho}_{\uparrow}(\vec{\boldsymbol{r}}) - \boldsymbol{\rho}_{\downarrow}(\vec{\boldsymbol{r}}) \quad \text{(III-40)}$$

$$\boldsymbol{E} = \boldsymbol{E}[\boldsymbol{\rho}, \boldsymbol{m}] = \boldsymbol{E}[\boldsymbol{\rho}_{\uparrow}, \boldsymbol{\rho}_{\downarrow}] \quad \text{(III-41)}$$

$$E_{XC}^{LSDA}[\boldsymbol{\rho}_{\uparrow}, \boldsymbol{\rho}_{\downarrow}] = \int \rho(\vec{r})\, \varepsilon_{XC}[\boldsymbol{\rho}_{\uparrow}(\vec{r}), \boldsymbol{\rho}_{\downarrow}(\vec{r})] d\vec{r} \quad \text{(III-42)}$$

Here: $\varepsilon_{XC}[\boldsymbol{\rho}_{\uparrow}(\vec{r}), \boldsymbol{\rho}_{\downarrow}(\vec{r})]$ is the functional of the exchange-correlation energy per particle of a uniform electron gas. The equation of Kohn and Sham (III-32) for the two spin is written:

$$\left[-\frac{1}{2}\nabla^2 + V_{eff}^{\uparrow}(\vec{r})\right]\phi_i(\vec{r}) = \varepsilon_i^{\uparrow}\phi_i(\vec{r}) \quad \text{(III-43)}$$

$$\left[-\frac{1}{2}\nabla^2 + V_{eff}^{\downarrow}(\vec{r})\right]\phi_i(\vec{r}) = \varepsilon_i^{\downarrow}\phi_i(\vec{r}) \quad \text{(III-44)}$$

Within the effective potential of equation (III-33), only the exchange-correlation contribution depends on the spin. On the other hand, the other terms of Coulomb energy remain functional of the total density. We then write:

$$V_{eff}^{\uparrow}(\vec{r}) = V_{ext}(\vec{r}) + V_H[\rho(\vec{r})] + \frac{\delta E_{XC}(\boldsymbol{\rho}_{\uparrow}, \boldsymbol{\rho}_{\downarrow})}{\delta \rho^{\uparrow}(\vec{r})} \quad \text{(III-45)}$$

$$V_{eff}^{\downarrow}(\vec{r}) = V_{ext}(\vec{r}) + V_H[\rho(\vec{r})] + \frac{\delta E_{XC}(\boldsymbol{\rho}_{\uparrow}, \boldsymbol{\rho}_{\downarrow})}{\delta \rho^{\downarrow}(\vec{r})} \quad \text{(III-46)}$$

III.7.3. Generalized gradient approximation (GGA)

In order to take into account the inhomogeneity of the electronic density of real systems to improve the estimation of the exchange-correlation functional, some authors had the idea of taking into consideration not only the local density within a unit of volume but also its variation, estimated from other neighboring volumes. The exchange-correlation energy will therefore be expressed as a function of the electron density $\boldsymbol{\rho}$ ($\boldsymbol{r}^{\rightarrow}$) and of the gradient of this one $\boldsymbol{\nabla\rho}$ ($\boldsymbol{r}^{\rightarrow}$) also:

$$E_{XC}^{GGA}[\rho] = \int \rho(\vec{r}).\{\varepsilon_X^{GGA}[\rho, \Delta\rho], \varepsilon_C^{GGA}[\rho, \Delta\rho]\}\, d\vec{r} \quad \text{(III-47)}$$

GGA functional are built according to two different procedures. The first one is of an empirical nature and consists of a numerical interpolation of the experimental results like the exchange functions denoted B (Becke88) **[14]**, PW (Perdew-Wang) **[15]** or even mPW (Modified Perdew-Wang) **[16].** The second procedure consists of building the functional on the basis of the principles of quantum mechanics (they are more rational), such as functional exchange P (Perdew86) **[17]** or PBE (Perdew-Burke-Ernzerhof) **[18]**.

Compared to the LSDA approximation, the GGA approximation can improve the precision on the total energy value **[18]**, the atomization energies **[19]**, the barrier energies or deviations of energy between different bands **[20**,**21]**. It also makes a correction on the chemical links. It tends to make them weaker and longer **[22]**. However, this correction is sometimes overestimated compared to the LSDA approximation **[23]**. As expected, the GGA approximation gives relatively better results for materials with spatial variations in electron density; this is particularly the case of oxides of transition metal, such as perovskites which have very localized electrons.

Although the GGA approximation and its various variants have largely shown their efficiency in calculations (magnetism in metals, cohesion, electronic properties of metals surface and semiconductors, etc.), they do not always give satisfactory results. They still fail to determine the width of the gap. The underestimation of the gap can reach 50% compared to experimental data **[24-26]**.

III.7.4.Potential of Becke-Johnson (BJ) and its modification (mBJ)

A revised version of the exchange potential, initially proposed by Becke and Johnson **[42]**, was subsequently presented by Tran and Blaha **[27]**. Tran and Blaha **[28]** conducted tests on the Becke-Johnson (BJ) exchange potential, designed by Becke and Johnson to replicate the shape of the exact exchange potential, i.e., the optimized effective potential (OEP). They observed that employing the BJ potential in conjunction with the correlation potential of LDA consistently led to underestimated gap energies. To enhance these outcomes, Tran and Blaha **[27]** introduced a straightforward modification to the original BJ potential, resulting in improved agreement with more computationally intensive approaches such as hybrid functionals **[26,29,30]**, and the GW method **[31-33]**.

This modified potential is known as the mBJ potential (or TB potential: Tran-Blaha) and has been incorporated into the ab-initio Wien2k code. The mBJ potential is formulated as follows:

$$V_{x,\sigma}^{TB-mBJ}(\vec{r}) = c.V_{x,\sigma}^{BR}(\vec{r}) + (3c-2)\frac{1}{\pi}\sqrt{\frac{5}{6}}\sqrt{\frac{t_\sigma(\vec{r})}{\rho_\sigma(\vec{r})}} \qquad \text{(III-49)}$$

Where

The electron density for a given spin $\sigma = \pm \frac{1}{2}$:

$$\rho_\sigma(\vec{r}) = \sum_{i=1}^{n_\sigma} \left|\phi_{i,\sigma}(\vec{r})\right|^2 \qquad \text{(III-50)}$$

The density of kinetic energy:

$$t_\sigma(\vec{r}) = \frac{1}{2}\sum_{i=1}^{n_\sigma} \nabla\phi_{i,\sigma}^{*}(\vec{r}).\nabla\phi_{i,\sigma}(\vec{r}) \quad \text{(III-51)}$$

The potential of Becke-Roussel

$$V_{x,\sigma}^{BR}(\vec{r}) = -\frac{1}{b_\sigma(\vec{r})}\left(1 - e^{-x_\sigma(\vec{r})} - \frac{1}{2}x_\sigma(\vec{r}).e^{-x_\sigma(\vec{r})}\right) \quad \text{(III-52)}$$

Becke-Roussel (BR) **[34]** is suggested as a representation for the Coulomb potential generated by the exchange hole.

x_σ in equation (III.52) is determined from $\rho_\sigma(\vec{r})$, $\nabla\rho_\sigma(\vec{r}), \nabla^2\rho_\sigma(\vec{r})$, and $t_\sigma(\vec{r})$; while $b_\sigma(\vec{r})$ is calculated using the following relation:

$$b_\sigma(\vec{r}) = \left[\frac{x_\sigma^3(\vec{r})e^{-x_\sigma(\vec{r})}}{8\pi\rho_\sigma(\vec{r})}\right]^{\frac{1}{3}} \quad \text{(III-53)}$$

In equation (III-49), (c) was chosen to depend linearly on the square root of the mean of $\nabla\rho(\vec{r})/\rho(\vec{r})$ **[43]**:

$$c = \alpha + \beta\left(\frac{1}{\Omega_{cell}}\int_{\Omega_{cell}} \frac{\nabla\rho(\overrightarrow{r'})}{\rho(\overrightarrow{r'})} d^3\overrightarrow{r'}\right)^{\frac{1}{2}} \quad \text{(III-54)}$$

α and β are adjustable parameters (α = -0.012 (dimensionless) and β = 1.023 Bohr1 / 2) and Ω_{cell} is the volume of the unit cell.

Equation (III-49) was chosen so as to restore the exchange potential of LDA for a density electron constant (regardless of the value of parameter c):

. $$V_x^{LDA}[\rho(\vec{r})] = -\left(\frac{3}{\pi}\right)^{\frac{1}{3}}\left(2\rho_\sigma(\vec{r})\right)^{\frac{1}{3}} \quad \text{(III-55)}$$

This formulation is highly appealing since obtaining the exchange potential at a specific point, denoted as $\vec{r}$, only requires knowledge of the density at that same point, represented as $\rho(\vec{r})$. Although the expression for the correlation potential is somewhat more intricate, it similarly relies solely on the local density. In other words, determining the correlation potential at a given point is solely contingent on the density value at that specific point.

In addition, the potential $V_{x,\sigma}^{BR}(\vec{r})$ is considered equal to the Slater potential, $V_{x,\sigma}^{Slater}(\vec{r})$ which represents the mean of the Hartree-Fock potential **[35]**:

$$V_{x,\sigma}^{BR}(\vec{r}) \approx V_{x,\sigma}^{Slater}(\vec{r}) \quad \text{(III-56)}$$

As a result, the BR potential is reduced to (3/2) of the potential V_x^{LDA}, and the second term of equation (III-49) (without the term (3c-2)) is reduced to $-\frac{1}{2}V_x^{LDA}$ since

$$t_\sigma = \left(\frac{3}{20}\right).(3\pi^2)^{\frac{3}{2}}.(2\rho_\sigma)^{\frac{5}{3}} \quad \text{(III-57)}$$

For a constant density

When *c*=1, the original Becke-Johnson (BJ) potential is replicated. Through varying *c* for a particular material, it was observed **[27]** that for several solids, the gap energy consistently increases with *c*. Specifically, for solids with small gaps, the optimal value C_{opt} (the value of *c* leading to perfect agreement with experimental results) falls within the range of 1.1 to 1.3, while for solids with larger gaps, C_{opt} is higher (varying from 1.4 to 1.7).

Drawing inspiration from the screened hybrid functional (HSE14) **[36]** principle, Tran and Blaha **[27]** utilized equation (III-49) to adjust *c* relative to C_{opt}. Therefore, this equation (III-49) is considered a type of hybrid potential in which the "Exact" exchange potential value is determined by *c*.

III.8. Calculation method

III.8.1. Introduction

In the framework of the Kohn-Sham equations (III-32), the exchange-correlation component can be determined through approximations like Local Density Approximation (LDA) and Generalized Gradient Approximation (GGA), as discussed earlier. Defining the remaining portion of the effective potential in the system becomes necessary.

Given the option to separately address valence and core electronic states (refer to Section III.3: Born-Oppenheimer Approximation), various choices emerge. Two major classes of potentials are identified: "all-electron" potentials and "pseudo-potentials."

- An all-electron potential may be either comprehensive (FP: Full Potential), encompassing all electrons in the system without any simplification, or of the Muffin-Tin (MF) variety, assuming a spherical potential within each atom of the crystal and a constant value in the region between these atoms (see **Figure. III. 2**).
- In the context of a pseudo-potential, only valence electrons are explicitly considered during the computation, while other core states are held fixed within a constant potential.

The selection of an appropriate potential for the specific type of calculation being conducted significantly influences the accuracy of the obtained results.

Much like the decision regarding the potential, the careful selection of the "wave function basis" is crucial as it directly impacts the efficiency of the calculation, depending on the properties under investigation. Various methodologies utilizing diverse types of basis have been established within the context of Density Functional Theory (DFT). Despite the method employed, a commonality is the self-consistent resolution of the Kohn-Sham equations.

In a crystal characterized by a periodic potential $V(\vec{\boldsymbol{r}} + \vec{\boldsymbol{a}}) = V(\vec{\boldsymbol{r}})$, where $\vec{\boldsymbol{a}}$ represents the crystal's periodicity), the solutions to the Kohn-Sham equations adopt the form of Bloch waves [37]

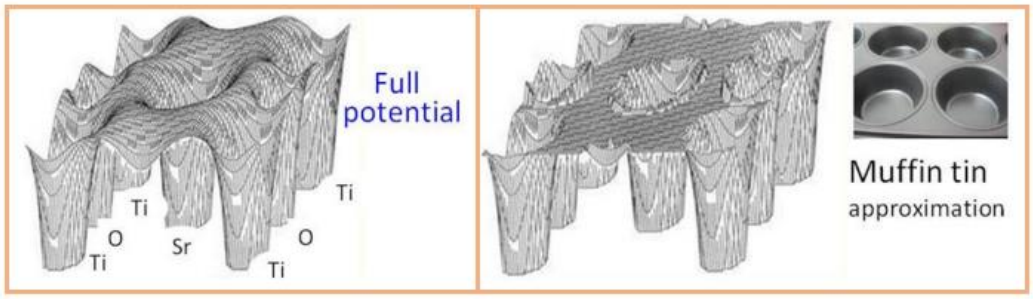

Figure. III. 2: Crystalline potential in $SrTiO_3$: (a) total potential and (b) muffin-tin potential.

III.8.2.Bloch theorem

One of the fundamental characteristics of a crystal is translation symmetry. In a crystal, the ions are arranged in such a way that the crystalline structure repeats periodically and infinitely in space. The infinitely sized system can therefore be described finitely through the concept of periodicity. If $\vec{R}$ denotes a vector of the crystal lattice, the effective potential $V_{eff}(\vec{r})$ the electron density $\rho(\vec{r})$, and the wave functions $\emptyset(\vec{r})$ obey to :

$$V_{eff}(\vec{R} + \vec{r}) = V_{eff}(\vec{r}) \quad \text{(III-58)}$$

$$\rho(\vec{R} + \vec{r}) = \rho(\vec{r}) \quad \text{(III-59)}$$

$$\phi(\vec{R} + \vec{r}) = \phi(\vec{r}) \quad \text{(III-60)}$$

Applying this condition of translation symmetry invariance to the solutions of the Kohn-Sham equations allows us to write the wave functions $\emptyset_i(\vec{r})$in the form of Bloch functions **[37]**.

$$\emptyset_i(\vec{r}) = f(\vec{r})e^{i\vec{k}.\vec{r}} \quad \text{(III-61)}$$

Where,

$\vec{k}$: vector belonging to the reciprocal space and characterizing the wave function. Due to translation symmetry, only vectors belonging to the first Brillouin zone are considered.

$f(\vec{r})$: periodic function, which can be expanded in a Fourier series, i.e., on a basis of plane waves whose wave vectors G are those of the reciprocal lattice

$$f(\vec{r}) = \sum_G C_{i,G} e^{i\vec{G}.\vec{r}} \quad \text{(III-62)}$$

One can then write the wave function $\phi(\vec{r})$ as a sum of plane waves:

$$\emptyset_i(\vec{r}) = \sum_G C_{i,k+G} e^{i(\vec{k}+\vec{G}).\vec{r}} \quad \text{(III-63)}$$

At this stage, the only unknowns are the coefficients $C_{i,k+G}$ In principle, expressing a periodic function as a Fourier series requires an infinite number of terms. However, here we can truncate the series defined by a cutoff kinetic energy. The kinetic energy is defined as:

$$E_{cin}(\vec{k}+\vec{G}) = \frac{\hbar^2}{2m_e}(\vec{k}+\vec{G})^2 \quad \text{(III-64)}$$

Where m_e is the mass of the electron. Thus, when a wave function is expanded over a basis of plane waves for each *k* point, the sum will be truncated from a certain kinetic energy $E_{cut-off}$

$$E_{cin}(\vec{k}+\vec{G}) < E_{cut-off} \quad \text{(III-65)}$$

This truncation will introduce an error in the calculation of the total energy; however, this error can be reduced by increasing the value of $E_{cut-off}$. The more oscillatory the wave function $\phi(\vec{r})$ is, the more significant the truncation energy and consequently the number of plane waves must be to provide an accurate description. Thus, Bloch's theorem allows one to transition from N Kohn-Sham equations, where N is the infinite number of electrons, to N_{cell}*N_k equations (where Ncell is the number of electrons in the unit cell and Nk is the number of reciprocal space

vectors chosen to sample the first Brillouin zone, following, for example, the Monkhorst and Pack method).

III.8.3. Linearized augmented plane waves (LAPW or FP-LAPW)

III.8.3.1. Augmented Plane waves (APW)

A stationary plane wave is a periodically repeating wave in physical space, with periodicity defined for any wave vector $\vec{k}$ in reciprocal space.

$$f(\vec{r}) = C_{\vec{k}} e^{i\vec{k}.\vec{r}} \qquad \text{(III-66)}$$

Here, $C_{\vec{k}}$ represents the complex amplitude of the wave.

Opting for a basis comprising plane waves offers advantages owing to the straightforward nature of these functions, negating the requirement for assumptions regarding the ultimate wave function's structure. The formulation of the system's equations becomes considerably simpler in comparison to employing localized basis localized around atoms.

In 1937, Slater **[38]** suggested an improvement to this model by partitioning space into two regions: discrete "Muffin-Tin" spheres with a radius $R\alpha$ surrounding atoms and an interstitial region between atoms (**Figure. III. 3**). These two regions are addressed separately.

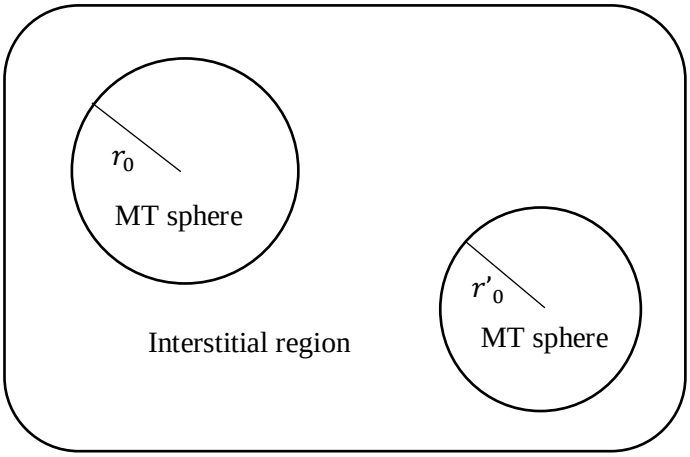

Figure. III. 3: Diagram illustrating the distribution of the elementary cell into atomic spheres and interstitial regions.

In regions proximal to the atomic nucleus (where $r < R\alpha$), electrons exhibit behavior akin to being within isolated atoms, subject to a spherically symmetric potential. The wave functions in these areas serve as solutions to the radial component of the Schrödinger equation. Conversely, in the interstitial regions between the spheres (where $r > R\alpha$), electrons are relatively "free", and the potential is treated as constant.

$$V(\vec{r}) = \begin{cases} V(r) & r \leq R_\alpha \\ V_0 & r > R_\alpha \end{cases} \quad \text{(III-67)}$$

In this scenario, the wave functions utilized to describe them adopt the form of plane waves.

The augmented plane waves (APW) wave functions embody both characteristics, acting as plane waves in the interstitial region and having a radial envelope in the spherical portion:

$$\begin{cases} \phi(\vec{r}) = \sum \; A_{lm} Y_{lm}(\vec{r}) U_l(\vec{r}, E_l) & pour\ r < R_\alpha \\ \phi(\vec{r}) = \frac{1}{\sqrt{\Omega}} \sum_K C_{\vec{k}} e^{i(\vec{k}+\vec{K}).r} & pour\ r > R_\alpha \end{cases} \quad \text{(III-68)}$$

Here, $\phi(\vec{r})$ represents the wave function, Ω is the unit cell volume, Y_{lm} denotes spherical harmonics, A_{lm} are coefficients, and $U_l(\vec{r}, E_l)$ signifies the radial solution to the Schrödinger equation:

$$\left[-\frac{\partial}{\partial \vec{r}^2} + \frac{l(l+1)}{\vec{r}^2} + V(\vec{r}) - E_l\right] \vec{r}.\dot{U}_l(\vec{r}, E_l) = 0 \quad \text{(III-69)}$$

E_l: energy parameter

$V(\vec{r})$: the spherical component of the potential in the sphere

The radial functions defined by the preceding equation are orthogonal to any eigenstate of the core, but this orthogonality disappears at the boundary of the sphere **[38].**As shown in the following equation:

$$(E_1 - E_2) r U_1 U_2 = U_2 \frac{d^2 r U_1}{dr^2} - U_1 \frac{d^2 r U_2}{dr^2} \quad \text{(III-70)}$$

U_1, U_2: are the radial solutions for energies $E_1$and E_2, respectively.

Slater made a particular choice for the wave functions, showing that plane waves are solutions of the Schrödinger equation in a constant potential. Meanwhile, radial functions are the solution

in the case of a spherical potential. Therefore, he proves that E_l is equal to the eigenvalue E. This approximation is very good for materials with a cubic face-centered structure and becomes less satisfactory as the material's symmetry decreases **[38].** To ensure the continuity of the function $\phi(\vec{r})$ at the surface of the MT sphere, the A_{lm} coefficients must be expanded in terms of the C_G coefficients of plane waves existing in the interstitial regions. Thus, after some algebraic calculations :

$$A_{lm} = \frac{4\pi i^l}{\Omega^{1/2} U_l(R_{MT})} \sum C_G J_l(|k+G|R_{MT}) Y_{lm}^*(k+G) \qquad \text{(III-71)}$$

J_l: Bessel function

Where, the origin is taken at the center of the sphere and r_l is its radius. Thus, the A_{lm} coefficients are completely determined by the coefficients of the plane waves, and the energy parameters E_l are variational coefficients in the (APW) method. The wave functions behave like plane waves in the interstitial region, and they increase in the core region and behave like radial functions. For the energy E_l, the APWs functions are solutions of the Schrödinger equation, with E_l equal to the energy band indexed by G. This meant that the energy bands cannot be obtained by simple diagonalization, and this implies treating the secular determinant as a function of energy. The function appearing in equation (III.68) depends on E_l, and may become zero at the surface of the MT sphere, leading to the separation between radial functions and plane waves. To solve this problem, several modifications have been made to the APW method. Among these, we mention the work of Anderson **[39]**, as well as that of Koelling and Abrman **[25]**.

III.8.3.2. All-electron methods (FP-LAPW)

LAPW, which ensures the continuity of the potential at the surface of the muffin-tin sphere MT, expands the potential in the form:

$$V(\vec{r}) = \begin{cases} \sum_{lm} V_{lm}(r) Y_{lm}(r) \\ \sum_K V_K e^{ikr} \end{cases} \qquad \text{(III-72)}$$

In 1975, Anderson proposed a method in which the basis functions and their derivatives are continuous for a given energy E_l. This choice resolves the issues encountered in the APW method, thus providing a flexible and accurate band structure method. This method is called the Linear Augmented Plane Wave (LAPW) method.

The modification consists of representing the wave function $\phi(\vec{r})$ inside the sphere by a linear combination of the radial functions $U_l(\vec{r})$ and their derivatives $\dot{U}_l(\vec{r})$ with respect to energy multiplied by spherical harmonics Y_{lm}.

The basis functions inside the sphere are linear combinations of the radial functions) $U_l(r)Y_{lm}(r)$ and their derivatives) $\dot{U}_l(r)Y_{lm}(r)$ with respect to energy.

The functions $U_l(r)$ are defined as in the APW method, and the function) $\dot{U}_l(r)Y_{lm}(r)$ must satisfy the following condition:

$$\left[-\frac{\partial}{\partial \vec{r}^2}+\frac{l(l+1)}{\vec{r}^2}+V(\vec{r})-E_l\right]\vec{r}.\dot{U}_l(\vec{r})=\vec{r}.U_l(\vec{r}) \qquad \text{(III-73)}$$

The combination of the radial functions $U_l(r)$ and $\dot{U}_l(r)$ ensures continuity with the plane waves of the interstitial region at the surface of the muffin-tin sphere. The augmented wave functions are then used as the basis functions of the FP-LAPW method, thus we have:

$$\begin{cases}\phi(\vec{r})=\sum_{lm}A_{lm}U_l(r,E_l)+B_{lm}\dot{U}_l(r,E_l) & pour\ r<R_\alpha \\ \phi(\vec{r})=\frac{1}{\sqrt{\Omega}}\sum_G C_G e^{i(\vec{k}+\vec{G}).\vec{r}} & pour\ r>R_\alpha\end{cases} \qquad \text{(III-74)}$$

Where:

- A_{lm} are coefficients corresponding to the function $U_l(r)$.
- B_{lm} are coefficients corresponding to the function $\dot{U}_l(r)$.

The FP-LAPW functions are plane waves only in the interstitial regions as in the APW method. The radial functions can be expanded around E_l as follows **[59]**:

$$U_l(E,r)=U_l(E_l,r)+(E-E_l)\dot{U}_l(E,r)+O(E-E_l)^2 \qquad \text{(III-75)}$$

With:

- $O(E-E_l)^2$ denotes the quadratic error committed.

The FP-LAPW method results in an error on the wave functions of the order of $O(E-E_l)^2$and another one on the band energy of the order $O(E-E_l)^4$ **[60]**.

. Despite these minor drawbacks, LAPW functions form a good basis, allowing, with a single E_l, to obtain all valence bands within a fairly wide energy range. However, it is sometimes necessary to divide the energy interval into several energy windows, each corresponding to an

energy E_l where the solution will be obtained separately **[40]**. Summarizing some advantages of the LAPW method compared to the APW method, we note:

- In the LAPW method, the band energy at the k point is obtained with a single diagonalization, whereas in the APW method, it is necessary to compute the energy for each band.
- The asymptote problem in the APW method is resolved by introducing the derivative of the radial function with respect to energy, which ensures that plane waves do not decouple from radial functions.

- The basis of the LAPW method has greater flexibility compared to that of the APW method inside the sphere. This stems from the fact that the basis functions of FP-LAPWs have more variational freedom than those of the APWs method where the parameter E_l is fixed instead of being variational. When transitioning from the LAPW method to the APW method, the introduced error is of the order $O(E - E_l)^2$ for the wave functions and $O(E - E_l)^4$for the band energies.

III.8.3.3. The roles of the linearization energies E_l

As seen previously, the error incurred on the wave function (charge density) is of the order $(E - E_l)^2$, and for the band energy, it is of the order $O(E - E_l)^4$. Therefore, the optimal choice for E_l should be at the center of the energy band. One can optimize the choice of the parameter E_l by computing the total energy of the system for several values of E_l and selecting the parameter that gives the lowest energy.

Unfortunately, while these strategies work well in many cases, they fail miserably in several others, especially in alkali metals, rare earths, recently transition metals, and actinides. The reason for this failure is described in the presence of high core levels and the extent of core state (only known as semi-core state) in several elements.

Within the muffin-tin sphere, the augmented functions $U_l(r)Y_{lm}(r)$ and $\dot{U}_l(r)Y_{lm}(r)$ are orthogonal to any strictly limited core state. However, this orthogonality requirement is only met when there aren't any core states that have the same *l*. Consequently, there is a chance that valence states and semi-core states will be confused. While the FP-LAPW technique demands a careful selection of E_l. due to the non-orthogonality of some core states, the APW method does not address this issue. In this instance, changing E_l. would prevent the computation from being completed.

The most critical case is where there is an overlap between the FP-LAPW basis and core states, introducing spurious core states into the energy spectrum E_l, known as ghost bands. These possess a core-state character, a very limited dispersion, and are highly confined within the sphere, making them clearly identifiable. The energy parameter E_l can be adjusted to the energy of the core state in order to remove ghost bands from the spectrum. Using a local orbital extension is the best course of action in these situations. For a given *l*, this adds more variational freedom by enabling the precise treatment of core states and valence states in a single energy window. Not all applications have this choice, so in that instance, the biggest sphere radius must be selected.

III.8.3.4. Construction of radial functions

In the FP-LAPW method, the basis functions $U_l(\vec{r})$ are radial functions inside the spheres, with the condition that they and their derivatives $\dot{U}_l(\vec{r})$ are continuous at the boundary of this sphere, and plane waves in the interstitial region. Thus, the construction of basis functions involves determining:

1- The radial functions $U_l(\vec{r})$ and their derivatives $\dot{U}_l(\vec{r})$.

2- The coefficientsa_{lm} and b_{lm} that satisfy the boundary conditions.

The boundary conditions provide a simple way to determine the *cutoff* of the angular momentum $l_{max}$and to represent the $cutoff - G_{max}$ of the plane waves in the muffin-tin sphere for a radiusR_{MT}. A reasonable strategy is to choose these *cutoffs* such that $R_{MT}G_{max} = l_{max}$, which is achieved in practice. Since FP-LAPW calculations are generally very convergent for $R_{MT}G_{max}$ in the range 7.5-9, this is a result of the value of $lmax \approx 8$.

A-Non-relativistic radial functions

In the non-relativistic case, the radial functions $U_l(\vec{r})$ are solutions of the Schrödinger equation with a spherical potential and a fixed energy E_l.

$$\left\{-\frac{d^2}{dr^2} + \frac{l(l+1)}{r^2} + V(\vec{r}) - E_l\right\} rU_l(\vec{r}) = 0 \qquad \text{(III-76)}$$

Where

$V(\vec{r})$: is the radial part of the lattice harmonic for *l*=0. The boundary condition $rU_l(\vec{r}) = 0$ having been imposed.

The derivative with respect to energy $\dot{U}_l(\vec{r})$ according to **[60]** is:

$$\left\{-\frac{d^2}{dr^2}+\frac{l(l+1)}{r^2}+V(\vec{r})-E_l\right\}r\dot{U}_l(\vec{r})=rU_l(\vec{r}) \quad \text{(III-77)}$$

The normalization of $U_l(\vec{r})$ and $\dot{U}_l(\vec{r})$ according to **[60]** is given by:

$$\int_0^{R_\alpha} r^2\, U_l^2(\vec{r})d\vec{r}=1 \quad \text{(III-78)}$$

The function $\dot{U}_l(\vec{r})$ is normalized.

$$N_l \equiv \int_0^{R_\alpha} r^2\, \dot{U}_l^2(\vec{r})d\vec{r}=1 \quad \text{(III-79)}$$

This normalization condition in the FP-LAPW method can be replaced by the following equation:

$$R_{MT}^2\left[U_l'(R_{MT})\dot{U}_l(R_{MT})-U_l(R_{MT})\dot{U}_l(R_{MT})\right]=1 \quad \text{(III-80)}$$

With:

$$U_l'(E,r)=\left(\frac{\partial U_l(E,r)}{\partial r}\right) \text{ and } \dot{U}_l(E,r)=\left(\frac{\partial U_l(E,r)}{\partial E}\right) \quad \text{(III-81)}$$

This equation is used to numerically determine the functions $U_l(\vec{r})$ and $\dot{U}_l(\vec{r})$. With this normalization, $U_l(\vec{r})$ can be expanded in the form:

$$U_l(E+\delta)=U_l(E)+\partial\dot{U}_l(E)+\cdots \quad \text{(III-82)}$$

Choosing the norm of $\dot{U}_l(r)$ indicates the range for which the linearization of energy will be a good approximation. In particular, the errors on the linearization energy are deemed acceptable according to Anderson **[39]**.

$$\left\|\dot{U}_l(r)\right\|.|E_l-E|\leq 1 \quad \text{(III-83)}$$

Where: E_l is the energy parameter and E is the band energy. If such a choice is not possible, several options are available:

1. Divide the energy ranges into windows, and each of these windows is treated separately.
2. Use a development in the form of local orbitals (this is effectively the quadratic method).

3. Reduce the size of the sphere. Thus, reduce the norm of the derivative. In the following, we will discuss the first two methods, the third option was applied by Goedeker **[41]**.

B- Relativistic radial functions

In the case of heavy elements with high atomic numbers, relativistic effects need to be considered. Relativistic effects only concern the radial functions within the muffin-tin spheres. To introduce this effect, equations (III-76) and (III-77) need to be replaced by the Dirac equations and their derivatives with respect to energy. In order to solve these equations, Koelling and Harmon **[42]** devised a technique that neglects the spin-orbit effect, as done by Roskey **[61]**, Wood and Boring **[43]**, Tekeda **[44]**, Macdonald et al. **[45]**. The solutions of the Dirac equation are.

$$\psi_{kv} = \begin{bmatrix} g_k \chi_{kv} \\ -i f_k \sigma_r \chi_{kv} \end{bmatrix} \tag{III-84}$$

Where k is the relativistic quantum number given by l and j. χ_{kv} represents the spin operator (the radial coordinate has been suppressed). Koelling and Harmon **[42]** use a new function:

$$\phi_k = \frac{1}{2MC} g_k \tag{III-85}$$

With

$$M = m + \frac{1}{2C^2}(E - V) \tag{III-86}$$

g is the radial derivative of k times g. m is the mass and C is the speed of light in vacuum. We rewrite the solution at the energy level E, with the usual quantum numbers lm **[39]**, while neglecting the spin-orbit term:

$$\phi_k = \begin{bmatrix} g_l Y_{lm} \chi_s \\ \frac{l}{2MC} \sigma_r \left(-g' + \frac{1}{r} g_l \sigma \right) Y_{lm} \chi_s \end{bmatrix} \tag{III-87}$$

Where χ_s is the non-relativistic spin-orbit component (spin up, spin down).

Defining $P_l = r g_l$ and $Q_l = rC\phi_l$, the relativistic secular equation becomes:

$$P_l' = 2MQ_l + \frac{1}{r} P_l \tag{III-88}$$

$$Q_l' = \frac{1}{r} Q_l + \left[\frac{l(l+1)}{2Mr^2} + (V - E_l)\right] P_l \quad \text{(III-89)}$$

This last equation can be numerically solved similarly to the case of the non-relativistic Schrödinger equation using, for example, the predictor-corrector method, by providing the boundary conditions.

$$\lim_{r \to 0} \frac{Q}{P} = C \frac{\left[l(l+1)+1-\left({}^{2Z}/_{C}\right)\right]^2 - 1}{\left({}^{2Z}/_{C}\right)} \quad \text{(III-90)}$$

The spin-orbit term is then added to equation (III-88). The derivative with respect to energy leads to equations similar to those in the non-relativistic case, namely:

$$\dot{P}_l = 2\left(\dot{M} Q_l + M \dot{Q}_l\right) + \frac{1}{r} P_l \quad \text{(III-91)}$$

$$\dot{Q}_l = -\frac{1}{r} Q_l + \left[\frac{l(l+1)}{2Mr^2} + (V - E_l)\right] \dot{P}_l - \left[\frac{l(l+1)\dot{M}}{2M^2 r^2} + 1\right] P_l \quad \text{(III-92)}$$

We determine the components g_l and f_l from the solutions of P_l and Q_l. These same components will be used for the calculation of the charge density and the matrix elements. Thus, the quantity $U^2$is replaced in equation (III-78) by $g_l^2 + f_l^2$. However, at the boundary of the sphere, the f_l component disappears, leaving only the g_l component and its derivative.

C- Determination of A_{lm} and B_{lm} coefficients

The coefficients A_{lm} and B_{lm} are determined for each wave vector and for each atom by imposing that the basis functions, as well as their first derivatives, are continuous at the boundaries of the MT spheres. The basis functions are plane waves in the interstitial region.

$$\phi(k_n) = \Omega^{-\frac{1}{2}} e^{ik_n r} \quad \text{(III-93)}$$

With $K_n \equiv K + K_n$, they are written in the form of a linear combination of spherical solutions within the MT spheres.

$$\phi(k_n) = \sum\left[A_{lm} U_l(E_l) + B_{lm} \dot{U}_l(E_l)\right] Y_{lm}(r) \quad \text{(III-94)}$$

In this equation, Ω is the volume of the cell, k is the wave vector, and K_n is a vector of the reciprocal lattice. In contrast to the formalism of the standard APW method, in which the energy

E_l is constant, the FP-LAPW method allows for choosing different values of the parameter El depending on the angular momentum value.

The boundary condition at the surface of the MT sphere allows for the use of a Rayleigh plane wave expansion.

$$\phi(K_n + R_{MT}) = 4\pi\Omega^{-\frac{1}{2}} \sum_{lm} i^l j_l (K_n, R_{MT}) Y_{lm}^*(K_n) Y_{lm}(R_{MT}) \quad \text{(III-95)}$$

Taking into account the continuity of the angular momentum, we obtain:

$$A_{lm}(K_n) = 4\pi R_{MT}^2 \Omega^{-\frac{1}{2}} i^l Y_{lm}^*(k_n) a_l(k_n) \quad \text{(III-96)}$$

$$a_l(K_n) = \frac{\dot{U}_l (d/dr) j_l(K_n R_{MT}) - (d\dot{U}_l/dr) j_l(K_n R_{MT})}{R_{MT}^2 [(dU_l/dr)\dot{U}_l - U_l(d\dot{U}_l/dr)]} \quad \text{(III-97)}$$

$$B_{lm}(k_n) = 4\pi R_{MT}^2 \Omega^{-\frac{1}{2}} i^l Y_{lm}(k_n) b_l(k_n) \quad \text{(III-98)}$$

$$b_l(K_n) = \frac{(dU_l/dr) j_l(K_n R_{MT}) - U_l (d/dr) j_l(K_n R_{MT})}{R_{MT}^2 [(dU_l/dr)\dot{U}_l - U_l(d\dot{U}_l/dr)]} \quad \text{(III-99)}$$

And considering equation (III-79), (III-99) becomes:

$$b_l(K_n) = U_l' J_l(n) - U_l J_l'(n) \quad \text{(III-100)}$$

Where $j_l(K_n R_{MT})$ is replaced by $J_l(n)$.

This procedure in the FP-LAPW method has thus eliminated the asymptote problem that appeared

III.8.3.5. Potential determination

A- Poisson equation resolution

The potential used in the Kohn-Sham equations contains the exchange-correlation term and the Coulomb term $V_c(r)$. The latter is the sum of the Hartree potential $V_H(r)$ and the nuclear potential.

$V_c(r)$ is determined by the Poisson equation from the charge density (electronic and nuclear).

$$\nabla^2 V_c(\vec{r}) = 4\pi\rho(\vec{r}) \quad \text{(III-101)}$$

One can solve this equation in reciprocal space. To do this, Hamann **[46]** and Weinert **[47]** proposed a resolution method called "pseudo-charge", which is essentially based on the following two observations:

1. The charge density is continuous and varies slowly in the interstitial regions. However, it varies rapidly in the core region.
2. The Coulomb potential in the interstitial region depends not only on the charges in that region but also on the charges in the core region.

The charge density is described by a Fourier series in the interstitial region as follows:

$$\rho(\vec{r}) = \sum_G \rho(G)\, e^{iGr} \tag{III-102}$$

and the plane waves e^{iGr} are calculated using the Bessel function j.

$$\int_0^R r^{l+2} j_l(Gr)dr = \begin{cases} R^{l+3}\frac{j_l(Gr)}{Gr} & G \neq 0 \\ \frac{R^3}{3}\sigma_{l,0} & G = 0 \end{cases} \tag{III-103}$$

Then,

$$e^{iGr} = 4\pi e^{iGr_\alpha} \sum_{lm} i^l j_l(|G|.|r - r_\alpha|)\, Y_{lm}^*(G) Y_{lm}(r - r_\alpha) \tag{III-104}$$

Where r is the radial coordinate, $r\alpha$ is the position of sphere α, and R_{MT} is its radius. The Coulomb potential becomes:

$$V_c(G) = \frac{4\pi\rho(G)}{G^2} \tag{III-105}$$

Integrating equation (III-103), we find:

$$V_{pw} = \sum_{lm} V_{lm}^{pw}(r) Y_{lm}(r) = \sum_V V_V^{pw}(r) K_V(r) \tag{III-106}$$

Where: V_{pw} is the interstitial potential.

Let:

$$K_V(r) = \sum_m C_{Vm}(r) Y_{lm}(r) \tag{III-107}$$

So,

$$V_V^{pw}(r) = \sum_{lm} C_{Vm}(r)\, V_{lm}^{pw}(r) \quad \text{(III-108)}$$

The potential inside the MT sphere is determined by using the Green's function.

$$V_V(r) = V_{lm}^{pw}(r)\left[\frac{r}{R}\right]' + \frac{4\pi}{2l+1}\left\{\frac{1}{r^{l+1}}\int_0^r dr' r'^{l+2}\rho_V(r') + r'\int_r^R dr' r'^{l-1}\rho_V(r') - \frac{r'}{R^{2l+1}}\int_0^R dr' r'^{l+2}\rho_V(r')\right\} \quad \text{(III-109)}$$

Where: $\rho_V(r')$ are the radial parts of the charge density.

B- Exchange and correlation potential

In the local density approximation (LDA) and generalized gradient approximation (GGA), the exchange-correlation potential is linear unlike the Coulomb potential. Therefore, it needs to be calculated in real space where it is fortunately diagonal. The representation of the interstitial charge in real space is obtained directly from the Fourier transformation **[48,49]**. In the case of magnetic materials, the procedure mentioned above is generalized with the introduction of polarized spins. This involves transforming both the up-spin and down-spin densities into real space, computing the two components of V_{xc}, and subsequently transforming them into the LAPW representation.

The fast Fourier transform (FFT) allows obtaining the real space representation of the interstitial charge, from which we construct the coefficients of the plane waves defined by this equation:

$$D(r) = (-1)^{lp} D(\alpha, \beta, \gamma) \quad \text{(III-110)}$$

The exchange-correlation potential is calculated at each point of the mesh. Fast Fourier transform is then used to transform V_{xc} from real space to the plane wave representation, from which the star coefficients are obtained.

Mattheiss [40] used the Wigner formula [50] to obtain the exchange-correlation interstitial potential as follows:

$$V_{xc} = -\rho^{\frac{1}{2}}\left[0.984 + \frac{0.943656 + 8.8963\rho^{\frac{1}{3}}}{\left(1+12.57\rho^{\frac{1}{3}}\right)^2}\right] \quad \text{(III-111)}$$

Inside the spheres, the same procedure is applied with different values of ρ and a spherically symmetric potential.

III.8.4.Improvement of the FP-LAPW method

The energy of linearization E_l is of great importance in the FP-LAPW method. Near E_l , one can compute the band energy with very acceptable precision, and in most materials, it suffices to choose these energies near the band center. However, this is not always possible, and in some cases, choosing a single value of E_l is not sufficient for the calculation of all energy bands. This problem is encountered, for example, with materials with *4f* orbitals **[51,52]**, as well as with transition metal elements **[53-55]**. This is the fundamental problem of the so-called semi-core state: an intermediate state between the valence state and the core state.

However, in semi-core states, it is useful to use one of two methods: the use of multiple energy windows or the development of local orbitals.

III.8.4.1. Multiple energy windows

The most commonly used technique to address the semi-core problem is to divide the energy spectrum into windows, each corresponding to an energy E_l **[62,39]**. This processing procedure is illustrated in **Figure. III. 4**.

In this windowing treatment, a separation is made between the valence and semi-core states where a set of E_l is chosen for each window to handle the corresponding states. This amounts to performing two independent FP-LAPW calculations, but still with the same potential.

The FP-LAPW method is based on the fact that the functions $U_l(r)$ and $\dot{U}_l(r)$ are orthogonal to any core eigenstate and, in particular, to those located at the surface of the sphere. However, semi-core states often satisfy this condition, except in the presence of "ghost" bands between the semi-core and valence states.

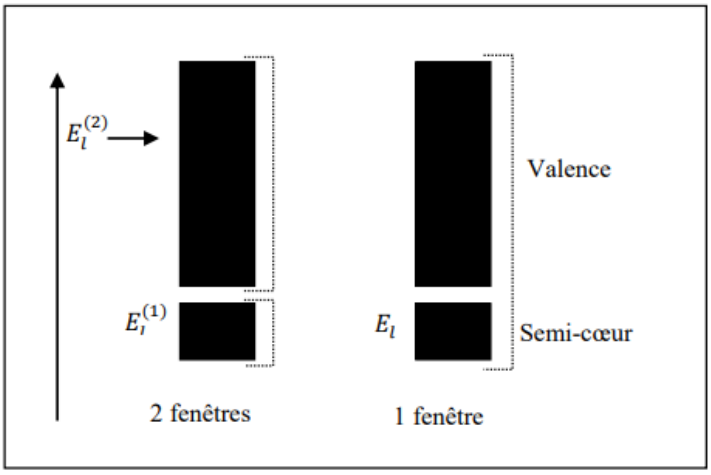

Figure. III. 4: Diagram representing multiple energy windows

III.8.4.2. LAPW+LO method

In the linearization of the secular equation, a problem arises: for a given value of *l*, only states with a given principal quantum number can be described. This can be a significant limitation for treating low-energy valence states (i.e., semi-core states). For example, consider the *p*-states of iron **[56]**: One solution is to treat the low-energy 3*p* states as core states by constructing a basis that includes 4*p* states among the valence states. However, in this case, there will be a portion of the total charge outside the MT sphere because the 3*p* states have energies that are too high. This occurs especially when bond lengths are too short and do not allow the MT sphere to be enlarged sufficiently. This is particularly evident when the compound is under pressure or subject to lattice vibrations. If both 3*p* and 4*p* states are considered as valence states, the basis will be less flexible in handling such situations. This difficulty is apparent in calculating electric field gradients at copper positions in superconductors, such as YBa2Cu3O7-x **[57]**.

To overcome this drawback of the LAPW method, two energy windows are used, and the resulting secular equations are solved separately. However, this method suffers from the risk that the corresponding eigenfunctions for the two windows may not be orthogonal.

Another method, called LAPW+LO **[55]**, uses a third category of basis functions. These functions are local orbitals, denoted as (LO):.

$$\emptyset(r) = \begin{cases} 0 & r > R_\alpha \\ \sum_{lm}\left[A_{lm}^{LO} U_l(r, E_{1,l}) + B_{lm}^{LO} \dot{U}_l(r, E_{1,l}) + C_{lm}^{LO} \dot{U}_l(r, E_{2,l})\right] & r < R_\alpha \end{cases} \quad \text{(III-112)}$$

With this choice, we can treat all bands from a single energy window. A local orbital is defined for a given atom for each *l* and *m*.

III.8.4.3. APW+lo method

The problematic issue of the APW method is its basis dependence on energy. In the LAPW+LO method, this dependence is eliminated, but the price to pay is a significant increase in the basis set used, which imposes limitations on both APW and LAPW+LO methods. Sjöstedt, Nordström, and Singh **[58]** recently introduced a further improvement by introducing a basis that combines the advantages of the APW method and those of the LAPW+LO method. This new method is called APW+lo and corresponds to an energy-independent basis similar to the LAPW+LO method, but it only requires a very slightly higher plane wave cutoff energy than that needed in the APW method. It involves using a standard APW basis but considering for a fixed energy E_l to retain the advantage provided by the linearization of the eigenvalue problem. Since it has been demonstrated previously that a fixed-energy basis does not provide a satisfactory description of eigen functions, local orbitals are also added to ensure variational flexibility in radial basis functions.

An APW+lo basis is defined by the combination of the following functions:

1) APW functions for a set of fixed energies E_l,

$$\emptyset(r) = \begin{cases} \frac{1}{\Omega^{\frac{1}{2}}} \sum_G C_G e^{i(G+k)r} \\ \sum_{lm} A_{lm} U_l(r) Y_{lm}(r) \end{cases} \quad \text{(III-113)}$$

2) Local orbitales

$$\emptyset(r) = \begin{cases} 0 \\ \sum_{lm} \left[A_{lm}^{LO} U_l\left(r, E_{1,l}\right) Y_{lm}(r) \right] \end{cases} \quad \text{(III-114)}$$

The local orbitals are no longer denoted as (LO) as in the LAPW+LO method, but as (lo) to distinguish them. The local orbitals (lo) are relatively similar to the (LO) orbitals, but they differ in that the coefficients A_{lm} and B_{lm} no longer depend on *k* and are now determined by the condition that these orbitals (lo) are zero on the sphere and normalized. Thus, both the APW orbitals and the (lo) orbitals are continuous at the sphere boundary, while their first derivatives are discontinuous.

This basis provides results as satisfactory as those of the LAPW+LO method while allowing to reduce the product $R_{\alpha}^{min} * k_{max}$to a value approximately equal to one.

III.8.5.Valence charge density

The wave function of a valence electron in a crystal is not an observable entity, but it allows obtaining the values of observable physical quantities. The wave function obtained from solving the Schrödinger equation is used to calculate the electronic charge density of a material. The square of its modulus represents the probability of finding the electron in a given volume:

$$\sum_{nk}|\psi_{nk}(r)|^2 d\Omega \qquad \text{(III-115)}$$

This concept of electron presence probability was first considered in the study of the hydrogen molecule: it was observed that the charge distribution of electrons largely depends on the considered state. Consequently, the bonding orbital in molecules always presents a maximum electronic charge density at the center of the bond between the two atoms. Conversely, the antibonding orbital is characterized by a maximum charge density between the nuclei.

The total charge density is obtained by summing over all occupied orbitals:

$$\rho(r) = 2e\sum_{nk}|\psi_{nk}(r)|^2 \qquad \text{(III-116)}$$

Where $\psi_{nk}(r)$ is the wave function of the valence electron, *n* is the band index, and *k* is the wave vector.

The valence charge density calculated by the LAPW method has two components:

1. The interstitial charge density, expanded in plane waves, given by:

$$\rho(r) = \sum_{kj} W(k,j) \sum_{GG'} \phi^*_{G,k,j}\, \phi_{G,k,j} e^{i(G-G').r} \qquad \text{(III-117)}$$

where the vector $\vec{\boldsymbol{r}}$ is limited to interstitial regions, $\phi_{G,k,j}$ are the coefficients of the band eigenvector, $i(G-G') * r$ and $W(k,j)$ represent the weight associated with point **k**.

2. A charge density located within the sphere, given by:

$$\rho(r) = \sum_V \rho(r) K_V(r) =$$

$$\sum_{kj} W(k,j) \sum_{Glm} \sum_{Gl'm'} \begin{Bmatrix} a^*_{lm}(G) a_{l'm'}(G') U_l(r) U'_l(r) \\ +a^*_{lm}(G) a_{l'm'}(G') U_l(r) U'_l(r) \\ +a^*_{lm}(G) a_{l'm'}(G') U_l(r) U'_l(r) \\ +a^*_{lm}(G) a_{l'm'}(G') U_l(r) U'_l(r) \end{Bmatrix} Y^*_{lm}(r) Y_{l'm'}(r) \qquad \text{(III-118)}$$

Avec $A_{lm} = \sum C_G a_{lm}(G)$ $B_{lm} = \sum C_G b_{lm}(G)$. The summation over *k* must be done over the entire *Brillouin zone*.

The charge density within the spheres is determined in the radial mesh using the harmonic coefficients of the lattice. The charge densities inside the spheres are constructed from the band eigenvectors of the first Brillouin zone.

III.9. Wien2k : code overview

Density functional theory (DFT) can be used to compute the electronic structure of solids with the computer package WIEN2k. It is based on one of the most precise approaches for band structure calculations: the full-potential (linearized) augmented plane-wave (LAPW) + local orbitals (lo) method. WIEN2k is a multi-featured all-electron system with relativistic effects included. More than 3600 user groups have licensed it, and according to Blaha WIEN2k, it has roughly 19000 citations on Google Scholar.

Wien2k, with its predecessors WIEN95 and WIEN97, is a collection of independent subprograms interconnected through C-SHELL scripts. Developed in FORTRAN90 by Blaha, Schwarz, Madsen, and collaborators at the University of Vienna (Austria), this code has seen continuous enhancements and updates up to its latest version, Wien2k-2019. Wien2k is widely recognized for its successful application in studying various organic and inorganic systems. Its ab initio computation process comprises four major stages:

In the first step, the initialization phase focuses on generating the initial electron density based on an atomic calculation. Several operations are executed using the following subprograms:

- **NN** calculates distances between nearest neighbors and equivalent positions, enabling the determination of atomic sphere radii (Muffin-Tin spheres).
- **SGROUP** identifies the space group of the structure.

- **SYMMETRY** is responsible for creating symmetry operations for the space group and determining the point group for individual atomic sites.
- **INSTKGEN** specifies the spin polarization of each atom.
- **LSTART** generates atomic densities and dictates how different atomic orbitals are treated in the band structure calculations (core or valence states).
- **KGEN** generates a k-point mesh within the Brillouin zone.
- **DSTART** produces an initial density for the self-consistent (SCF) cycle by combining atomic densities generated in LSTART.

In the second step, unit cell parameters of the structure are optimized by minimizing the total energy. Initially, the initial structure undergoes pressure and decompression constraints several times, producing structures with varying volumes. The ground-state energy for each structure is determined through a self-consistent calculation. The minimum energy, following curve fitting (energies vs. volumes), reveals the most energetically stable structure.

The third step involves calculating the energy, electron density, and magnetic moments of the ground state for the most stable structure (obtained in the previous step) during an SCF cycle. This cycle is initiated and repeated until convergence criteria are met. This stage utilizes another set of subprograms:

- **LAPW0** generates the Poisson potential based on the charge density.
- **LAPW1** computes valence bands, their eigenvalues, and eigenvectors.
- **LAPW2** calculates valence densities using eigenvectors.
- **LCORE** determines core states and densities.
- **MIXER** derives the new density value by blending the current cycle's density (i) with that of the previous cycle (i-1).

For spin-polarized computations, LAPW1, LAPW2, and LCORE subprograms are run twice, once for each spin (↑ and ↓).

In the final step, Upon concluding the self-consistent calculation, various properties of the ground state are determined, encompassing characteristics such as charge density, density of states, band structure, as well as mechanical, optical, thermodynamic, thermoelectric properties, and more.

This summary offers a broad perspective on the key elements of the Wien2k code and its ab initio computational procedure.

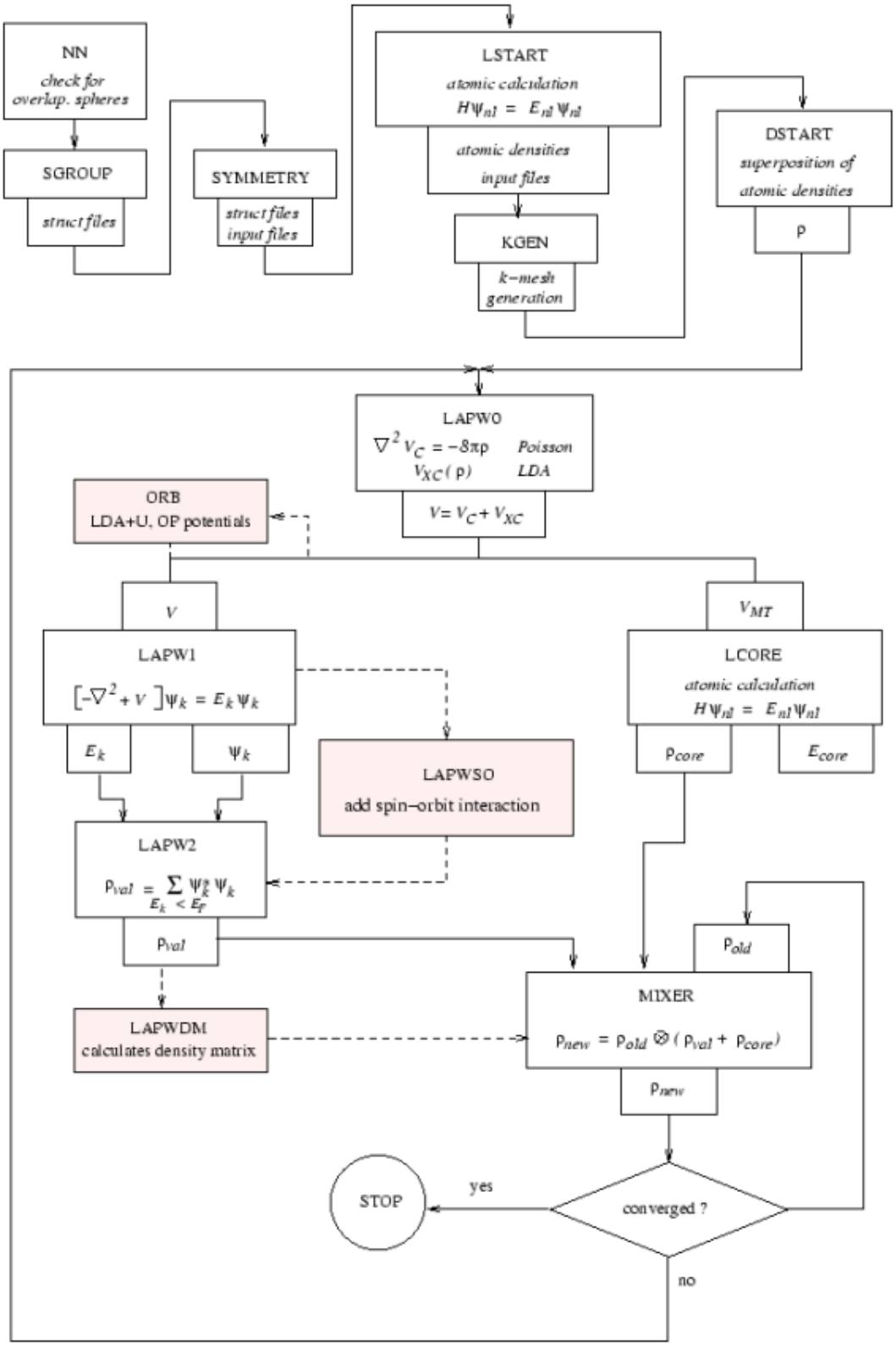

Figure. III. 5: Wien2k organigram

References

[1] M. Born and R. Oppenheimer, "Zur Quantentheorie der Molekeln," *Annalen der Physik*, vol. 389, no. 20, pp. 457–484, Jan. 1927, doi: 10.1002/andp.19273892002.

[2] D. R. Hartree, "The Wave Mechanics of an Atom with a Non-Coulomb Central Field. Part I. Theory and Methods," *Math. Proc. Camb. Phil. Soc.*, vol. 24, no. 1, pp. 89–110, Jan. 1928, doi: 10.1017/S0305004100011919.

[3] L. H. Thomas, "The calculation of atomic fields," *Math. Proc. Camb. Phil. Soc.*, vol. 23, no. 5, pp. 542–548, Jan. 1927, doi: 10.1017/S0305004100011683.

[4] E. Fermi, "Eine statistische Methode zur Bestimmung einiger Eigenschaften des Atoms und ihre Anwendung auf die Theorie des periodischen Systems der Elemente," *Z. Physik*, vol. 48, no. 1–2, pp. 73–79, Jan. 1928, doi: 10.1007/BF01351576.

[5] P. Hohenberg and W. Kohn, "Inhomogeneous Electron Gas," *Phys. Rev.*, vol. 136, no. 3B, pp. B864–B871, Nov. 1964, doi: 10.1103/PhysRev.136.B864.

[6] P. A. M. Dirac, "Note on Exchange Phenomena in the Thomas Atom," *Math. Proc. Camb. Phil. Soc.*, vol. 26, no. 3, pp. 376–385, Jul. 1930, doi: 10.1017/S0305004100016108.

[7] W. Kohn and L. J. Sham, "Self-Consistent Equations Including Exchange and Correlation Effects," *Phys. Rev.*, vol. 140, no. 4A, pp. A1133–A1138, Nov. 1965, doi: 10.1103/PhysRev.140.A1133.

[8] E. Wigner, "Effects of the electron interaction on the energy levels of electrons in metals," *Trans. Faraday Soc.*, vol. 34, p. 678, 1938, doi: 10.1039/tf9383400678.

[9] D. M. Ceperley and B. J. Alder, "Ground State of the Electron Gas by a Stochastic Method," *Phys. Rev. Lett.*, vol. 45, no. 7, pp. 566–569, Aug. 1980, doi: 10.1103/PhysRevLett.45.566.

[10] F. Becca and S. Sorella, *Quantum Monte Carlo approaches for correlated systems*. Cambridge, United Kingdom ; New York, NY: Cambridge University Press, 2017.

[11] P. M. Marcus, "Variational methods in the computation of energy bands," *Int. J. Quantum Chem.*, vol. 1, no. S1, pp. 567–588, Jun. 2009, doi: 10.1002/qua.560010659.

[12] N. Elyashar and D. D. Koelling, "Effect of non-muffin-tin terms on the electronic structure of transition metals: Niobium," *Phys. Rev. B*, vol. 13, no. 12, pp. 5362–5372, Jun. 1976, doi: 10.1103/PhysRevB.13.5362.

[13] D. J. Singh and L. Nordström, *Planewaves, pseudopotentials, and the LAPW Method*, 2. ed. New York, NY: Springer, 2006.

[14] A. D. Becke, "Density-functional exchange-energy approximation with correct asymptotic behavior," *Phys. Rev. A*, vol. 38, no. 6, pp. 3098–3100, Sep. 1988, doi: 10.1103/PhysRevA.38.3098.

[15] J. P. Perdew, K. Burke, and Y. Wang, "Generalized gradient approximation for the exchange-correlation hole of a many-electron system," *Phys. Rev. B*, vol. 54, no. 23, pp. 16533–16539, Dec. 1996, doi: 10.1103/PhysRevB.54.16533.

[16] C. Adamo and V. Barone, "Exchange functionals with improved long-range behavior and adiabatic connection methods without adjustable parameters: The mPW and mPW1PW models," *The Journal of Chemical Physics*, vol. 108, no. 2, pp. 664–675, Jan. 1998, doi: 10.1063/1.475428.

[17] J. P. Perdew and W. Yue, "Accurate and simple density functional for the electronic exchange energy: Generalized gradient approximation," *Phys. Rev. B*, vol. 33, no. 12, pp. 8800–8802, Jun. 1986, doi: 10.1103/PhysRevB.33.8800.

[18] J. P. Perdew, K. Burke, and M. Ernzerhof, "Generalized Gradient Approximation Made Simple," *Phys. Rev. Lett.*, vol. 77, no. 18, pp. 3865–3868, Oct. 1996, doi: 10.1103/PhysRevLett.77.3865.

[19] E. I. Proynov, E. Ruiz, A. Vela, and D. R. Salahub, "Determining and extending the domain of exchange and correlation functionals," *Int. J. Quantum Chem.*, vol. 56, no. S29, pp. 61–78, Feb. 1995, doi: 10.1002/qua.560560808.

[20] D. R. Hamann, "Generalized Gradient Theory for Silica Phase Transitions," *Phys. Rev. Lett.*, vol. 76, no. 4, pp. 660–663, Jan. 1996, doi: 10.1103/PhysRevLett.76.660.

[21] B. Hammer and M. Scheffler, "Local Chemical Reactivity of a Metal Alloy Surface," *Phys. Rev. Lett.*, vol. 74, no. 17, pp. 3487–3490, Apr. 1995, doi: 10.1103/PhysRevLett.74.3487.

[22] V. Ozoliņš and M. Körling, "Full-potential calculations using the generalized gradient approximation: Structural properties of transition metals," *Phys. Rev. B*, vol. 48, no. 24, pp. 18304–18307, Dec. 1993, doi: 10.1103/PhysRevB.48.18304.

[23] C. Filippi, D. J. Singh, and C. J. Umrigar, "All-electron local-density and generalized-gradient calculations of the structural properties of semiconductors," *Phys. Rev. B*, vol. 50, no. 20, pp. 14947–14951, Nov. 1994, doi: 10.1103/PhysRevB.50.14947.

[24] M. T. Yin and M. L. Cohen, "Theory of static structural properties, crystal stability, and phase transformations: Application to Si and Ge," *Phys. Rev. B*, vol. 26, no. 10, pp. 5668–5687, Nov. 1982, doi: 10.1103/PhysRevB.26.5668.

[25] D. R. Hamann, M. Schlüter, and C. Chiang, "Norm-Conserving Pseudopotentials," *Phys. Rev. Lett.*, vol. 43, no. 20, pp. 1494–1497, Nov. 1979, doi: 10.1103/PhysRevLett.43.1494.

[26] J. Heyd, J. E. Peralta, G. E. Scuseria, and R. L. Martin, "Energy band gaps and lattice parameters evaluated with the Heyd-Scuseria-Ernzerhof screened hybrid functional," *The Journal of Chemical Physics*, vol. 123, no. 17, p. 174101, Nov. 2005, doi: 10.1063/1.2085170.

[27] F. Tran and P. Blaha, "Accurate Band Gaps of Semiconductors and Insulators with a Semilocal Exchange-Correlation Potential," *Phys. Rev. Lett.*, vol. 102, no. 22, p. 226401, Jun. 2009, doi: 10.1103/PhysRevLett.102.226401.

[28] F. Tran, P. Blaha, and K. Schwarz, "Band gap calculations with Becke–Johnson exchange potential," *J. Phys.: Condens. Matter*, vol. 19, no. 19, p. 196208, May 2007, doi: 10.1088/0953-8984/19/19/196208.

[29] J. Paier, M. Marsman, K. Hummer, G. Kresse, I. C. Gerber, and J. G. Ángyán, "Screened hybrid density functionals applied to solids," *The Journal of Chemical Physics*, vol. 124, no. 15, p. 154709, Apr. 2006, doi: 10.1063/1.2187006.

[30] J. Paier, M. Marsman, K. Hummer, G. Kresse, I. C. Gerber, and J. G. Ángyán, "Erratum: 'Screened hybrid density functionals applied to solids' [J. Chem. Phys. 124, 154709 (2006)]," *The Journal of Chemical Physics*, vol. 125, no. 24, p. 249901, Dec. 2006, doi: 10.1063/1.2403866.

[31] W. G. Aulbur, M. Städele, and A. Görling, "Exact-exchange-based quasiparticle calculations," *Phys. Rev. B*, vol. 62, no. 11, pp. 7121–7132, Sep. 2000, doi: 10.1103/PhysRevB.62.7121.

[32] S. V. Faleev, M. Van Schilfgaarde, and T. Kotani, "All-Electron Self-Consistent G W Approximation: Application to Si, MnO, and NiO," *Phys. Rev. Lett.*, vol. 93, no. 12, p. 126406, Sep. 2004, doi: 10.1103/PhysRevLett.93.126406.

[33] M. Shishkin and G. Kresse, "Self-consistent G W calculations for semiconductors and insulators," *Phys. Rev. B*, vol. 75, no. 23, p. 235102, Jun. 2007, doi: 10.1103/PhysRevB.75.235102.

[34] A. D. Becke and M. R. Roussel, "Exchange holes in inhomogeneous systems: A coordinate-space model," *Phys. Rev. A*, vol. 39, no. 8, pp. 3761–3767, Apr. 1989, doi: 10.1103/PhysRevA.39.3761.

[35] J. C. Slater, "A Simplification of the Hartree-Fock Method," *Phys. Rev.*, vol. 81, no. 3, pp. 385–390, Feb. 1951, doi: 10.1103/PhysRev.81.385.

[36] A. V. Krukau, G. E. Scuseria, J. P. Perdew, and A. Savin, "Hybrid functionals with local range separation," *The Journal of Chemical Physics*, vol. 129, no. 12, p. 124103, Sep. 2008, doi: 10.1063/1.2978377.

[37] F. Bloch, "ber die Quantenmechanik der Elektronen in Kristallgittern," *Z. Physik*, vol. 52, no. 7–8, pp. 555–600, Jul. 1929, doi: 10.1007/BF01339455.

[38] J. C. Slater, "Wave Functions in a Periodic Potential," *Phys. Rev.*, vol. 51, no. 10, pp. 846–851, May 1937, doi: 10.1103/PhysRev.51.846.

[39] O. K. Andersen, "Linear methods in band theory," *Phys. Rev. B*, vol. 12, no. 8, pp. 3060–3083, Oct. 1975, doi: 10.1103/PhysRevB.12.3060.

[40] L. F. Mattheiss and D. R. Hamann, "Linear augmented-plane-wave calculation of the structural properties of bulk Cr, Mo, and W," *Phys. Rev. B*, vol. 33, no. 2, pp. 823–840, Jan. 1986, doi: 10.1103/PhysRevB.33.823.

[41] S. Goedecker, "Treatment of semicore states in the linearized augmented-plane-wave method and other linearized electronic-structure methods," *Phys. Rev. B*, vol. 47, no. 15, pp. 9881–9883, Apr. 1993, doi: 10.1103/PhysRevB.47.9881.

[42] D. D. Koelling and B. N. Harmon, "A technique for relativistic spin-polarised calculations," *J. Phys. C: Solid State Phys.*, vol. 10, no. 16, pp. 3107–3114, Aug. 1977, doi: 10.1088/0022-3719/10/16/019.

[43] J. H. Wood and A. M. Boring, "Improved Pauli Hamiltonian for local-potential problems," *Phys. Rev. B*, vol. 18, no. 6, pp. 2701–2711, Sep. 1978, doi: 10.1103/PhysRevB.18.2701.

[44] T. Takeda, "Linear methods for fully relativistic energy-band calculations," *J. Phys. F: Met. Phys.*, vol. 9, no. 5, pp. 815–829, May 1979, doi: 10.1088/0305-4608/9/5/009.

[45] A. H. MacDonald, W. E. Picket, and D. D. Koelling, "A linearised relativistic augmented-plane-wave method utilising approximate pure spin basis functions," *J. Phys. C: Solid State Phys.*, vol. 13, no. 14, pp. 2675–2683, May 1980, doi: 10.1088/0022-3719/13/14/009.

[46] D. R. Hamann, "Semiconductor Charge Densities with Hard-Core and Soft-Core Pseudopotentials," *Phys. Rev. Lett.*, vol. 42, no. 10, pp. 662–665, Mar. 1979, doi: 10.1103/PhysRevLett.42.662.

[47] M. Weinert, "Solution of Poisson's equation: Beyond Ewald-type methods," *Journal of Mathematical Physics*, vol. 22, no. 11, pp. 2433–2439, Nov. 1981, doi: 10.1063/1.524800.

[48] R. Singleton, "An algorithm for computing the mixed radix fast Fourier transform," *IEEE Trans. Audio Electroacoust.*, vol. 17, no. 2, pp. 93–103, Jun. 1969, doi: 10.1109/TAU.1969.1162042.

[49] A. D. McLaren, "Optimal numerical integration on a sphere," *Math. Comp.*, vol. 17, no. 84, pp. 361–383, 1963, doi: 10.1090/S0025-5718-1963-0159418-2.

[50] E. Wigner, "On the Interaction of Electrons in Metals," *Phys. Rev.*, vol. 46, no. 11, pp. 1002–1011, Dec. 1934, doi: 10.1103/PhysRev.46.1002.

[51] D. J. Singh, "Adequacy of the local-spin-density approximation for Gd," *Phys. Rev. B*, vol. 44, no. 14, pp. 7451–7454, Oct. 1991, doi: 10.1103/PhysRevB.44.7451.

[52] S. Goedecker, M. Teter, and J. Hutter, "Separable dual-space Gaussian pseudopotentials," *Phys. Rev. B*, vol. 54, no. 3, pp. 1703–1710, Jul. 1996, doi: 10.1103/PhysRevB.54.1703.

[53] P. Blaha, D. J. Singh, P. I. Sorantin, and K. Schwarz, "Electric-field-gradient calculations for systems with large extended-core-state contributions," *Phys. Rev. B*, vol. 46, no. 3, pp. 1321–1325, Jul. 1992, doi: 10.1103/PhysRevB.46.1321.

[54] D. J. Singh, K. Schwarz, and P. Blaha, "Electric-field gradients in YBa 2 Cu 3 O 7 : Discrepancy between experimental and local-density-approximation charge distributions," *Phys. Rev. B*, vol. 46, no. 9, pp. 5849–5852, Sep. 1992, doi: 10.1103/PhysRevB.46.5849.

[55] D. Singh and H. Krakauer, "*H* -point phonon in molybdenum: Superlinearized augmented-plane-wave calculations," *Phys. Rev. B*, vol. 43, no. 2, pp. 1441–1445, Jan. 1991, doi: 10.1103/PhysRevB.43.1441.

[56] L. J. Sham and W. Kohn, "One-Particle Properties of an Inhomogeneous Interacting Electron Gas," *Phys. Rev.*, vol. 145, no. 2, pp. 561–567, May 1966, doi: 10.1103/PhysRev.145.561.

[57] K. Schwarz, C. Ambrosch-Draxl, and P. Blaha, "Charge distribution and electric-field gradients in YBa 2 Cu 3 O 7 − x," *Phys. Rev. B*, vol. 42, no. 4, pp. 2051–2061, Aug. 1990, doi: 10.1103/PhysRevB.42.2051.

[58] E. Sjöstedt, L. Nordström, and D. J. Singh, "An alternative way of linearizing the augmented plane-wave method," *Solid State Communications*, vol. 114, no. 1, pp. 15–20, Mar. 2000, doi: 10.1016/S0038-1098(99)00577-3.

[59] S. Cottenier, ISBN 807215, 2002, 90.

[60] M. B. Kanoun, Doctorate thesis, Tlemcen university, 2004.

[61] F. Rosicky, P. Weinberg and F. Mark, J. Phys. B 9, 1976.

[62] R. Gaspar ,Acta. Phys. Hung. 3, 85. 1954.

Chapter IV : Results and discussion

IV.1. Introduction

The vacancy ordered double perovskites (VODP) exhibit noteworthy optoelectronic properties, making them suitable for solar cell applications due to their superior stability, long carrier diffusion lengths. Although recent studies have explored their potential in photovoltaic applications, challenges persist in synthesizing high-quality lead-free VODPs, and their performance in photovoltaic solar cells still falls behind lead-based counterparts.

Furthermore, VODPs show promise in thermoelectric applications due to properties like low lattice thermal conductivity. Research efforts have centered on materials such as Cs_2SnX_6 leveraging strategies like atomic doping and nanostructuring to enhance their exceptional thermoelectric performance.

This study aims to presenting crucial structural, thermoelectric, optoelectronic, and thermodynamic properties for vacancy-ordered double perovskites K_2SnX_6 (X=I, Br, and Cl). These parameters include thermal conductivity, electrical conductivity, power factor (PF), Seebeck coefficient, figure of merit, dielectric function, absorption coefficient, reflectivity, refractive index and optical conductivity….

The electronic configuration of each element of the studied compounds is:

[K]: $1s^2\ 2s^2\ 2p^6\ 3s^2\ 3p^6\ 4s^1$

[Sn]: $1s^2\ 2s^2\ 2p^6\ 3s^2\ 3p^6\ 3d^{10}\ 4s^2\ 4p^6\ 4d^{10}\ 5s^2\ 5p^2$

[Cl]: $1s^2\ 2s^2\ 2p^6\ 3s^2\ 3p^5$

[Br]: $1s^2\ 2s^2\ 2p^6\ 3s^2\ 3p^6\ 3d^{10}\ 4s^2\ 4p^5$

[I]: $1s^2\ 2s^2\ 2p^6\ 3s^2\ 3p^6\ 3d^{10}\ 4s^2\ 4p^6\ 4d^{10}\ 5s^2\ 5p^5$

IV.2. Computational details

One of the widely recognized approaches for assessing the structural properties of crystalline materials is density functional theory (DFT). The ground-state structural features of the compounds are determined through the optimization and relaxation of the unit cell design. The optimized structural parameters are then used to calculate the thermodynamic, electronic, optical, and thermoelectric properties of the compound. In this study, all computations were performed using first-principle methodologies, involving the iterative solution of Kohn-Sham's equation with the Wien2k **[1]** code and other integrated simulation tools. The Perdew-Burke-Ernzerhof sol based on Generalized Gradient Approximation (PBEsol -GGA) **[2**,**3]** is applied, utilizing the modified Becke-Johnson potential (mBJ) **[4]**. Muffin-tin spheres are also considered to encapsulate the researched components of double perovskites. Additionally, muffin-tin spheres are taken into account to enclose the researched components of double

perovskites. To achieve the desired behaviour of atomic-like waves inside the spheres and wave-like behaviour outside, the linearized augmented-plane wave technique (LAPW) is employed .

The Kohn-Sham wave functions are expanded in terms of spherical harmonics inside the muffin-tin spheres, and in a Fourier series in the interstitial region. In this region, the wave functions are extended into plane waves with a cutoff RMT.Kmax (RMT is the smallest radius of the muffin-tin spheres, and Kmax is the maximum value of the wave vector used in the plane wave expansion of the eigenfunctions).After conducting a convergence test, the value of RMTxKmax = 9 is chosen. A reduced Brillouin zone (BZ) technique is used to replicate the crystal structure under standard periodic boundary conditions. Integration across the Brillouin zone is performed with a dense mesh of 1100 k-points. The iterative process self-consistently terminates when the convergence conditions of 0.0001 e for charge and 0.000001 Ry for energy are met. For the determination of optical characteristics, up to 10,000 k-points are considered. Transport properties are calculated and analyzed using the BoltzTrap **[5]**

IV.3. Structural description

It is hypothesised that vacancy-ordered double perovskites K_2SnX_6 (X= Cl, Br, I) undergo a transition from a cubic (Fm3m) phase to a tetragonal (P4/mnc) phase, and finally a transition to a monoclinic (P21/n) phase when the temperature increases **[6**,**7]**.

The current investigation focused on the optimisation of the crystal structures of the compounds K_2SnX_6 (where X represents the halogens Cl, Br, and I) in their three phases cubic, tetragonal, and monoclinic. This optimisation was carried out using the PBEsol-GGA functional. In the initial stage, the K_2SnX_6 (X= Cl, Br, I) compounds undergo complete relaxation through the implementation of force optimisation. This step is called 'minimisation of atoms positions'. In **Tables. IV. 1-3** are summarized the atomic positions specific to each phase. In the next stage, the total energy is calculated as a function of volume, and the results were then interpolated using the Murnaghan equation of state **[8]**:

$$E(V) = E_0 + \frac{B_0}{B'(B'-1)}\left[V\left(\frac{V_0}{V}\right)^{B'} - V_0\right] + \frac{B_0}{B'}(V - V_0) \qquad \text{(IV-1)}$$

Where : E_0, V_0, B_0 et B' are respectively : the total energy, the equilibrium volume, the bulk modulus and its derivative. The bulk modulus is given by :

$$B_0 = -V\left(\frac{\partial P}{\partial V}\right)_T \qquad \text{(IV-2)}$$

$$P = -\left(\frac{\partial E}{\partial V}\right)_S \quad \text{(IV-3)}$$

$$B_0 = V\frac{\partial^2 E}{\partial V^2} \quad \text{(IV-4)}$$

The equilibrium volume is then given by the minimum of the curve $E(V)$. Subsequently, the structural lattice parameters are sequentially optimised.

The calculated parameters are displayed in **Table. IV. 4**. The results obtained in this study indicate that the predicted equilibrium lattice parameters align with the existing experimental and computational data **[6**,**7,9]**.

The crystallographic visualization of the structures of the three phases (cubic, tetragonal, monoclinic) was obtained using the 3D visualization program VESTA (Visualization for Electronic and Structural Analysis). The **Figures. IV. 1-3** illustrate the structures of cubic, tetragonal, and monoclinic phases, respectively.

Figure. IV. 4 presents the graphs depicting the optimised relationship between energy and volume. Upon examining the different volume optimisation graphs, it becomes evident that the monoclinic phase has the highest level of stability among the three phases. Hence, our investigation will primarily concentrate on the **monoclinic phase**.

IV.3.1. The cubic phase (Fm̄3m)

Description

Cubic K_2SnX_6 (X=Cl, Br, I) crystallizes in Fm̄3m space group. It crystallizes in the cubic structure with four formula units per unit cell (36 atoms per unit cell).

K^{+1} forms bonds with twelve equivalent X^{-1} ions creating KX_{12} cuboctahedra that share corners with twelve equivalent KX_{12} cuboctahedra, faces with six equivalent KX_{12} cuboctahedra, and faces with four equivalent SnX_6 octahedra. The $K-X$ bond lengths are 3.52 Å, 4.55 Å, 4.99 Å in K_2SnCl_6, K_2SnBr_6, and K_2SnI_6 respectively. Sn^{4+} is bonded to six equivalent X^{-1} ions to form SnX_6 octahedra that share faces with eight equivalent KX_{12} cuboctahedra. The Sn–X bond lengths are 2.45 Å, 2. 62 Å, 2.84 Å in K_2SnCl_6, K_2SnBr_6, K_2SnI_6 respectively. X^{-1} is bonded in a distorted single-bond geometry to four equivalent K^{1+} and one Sn^{4+} ion.

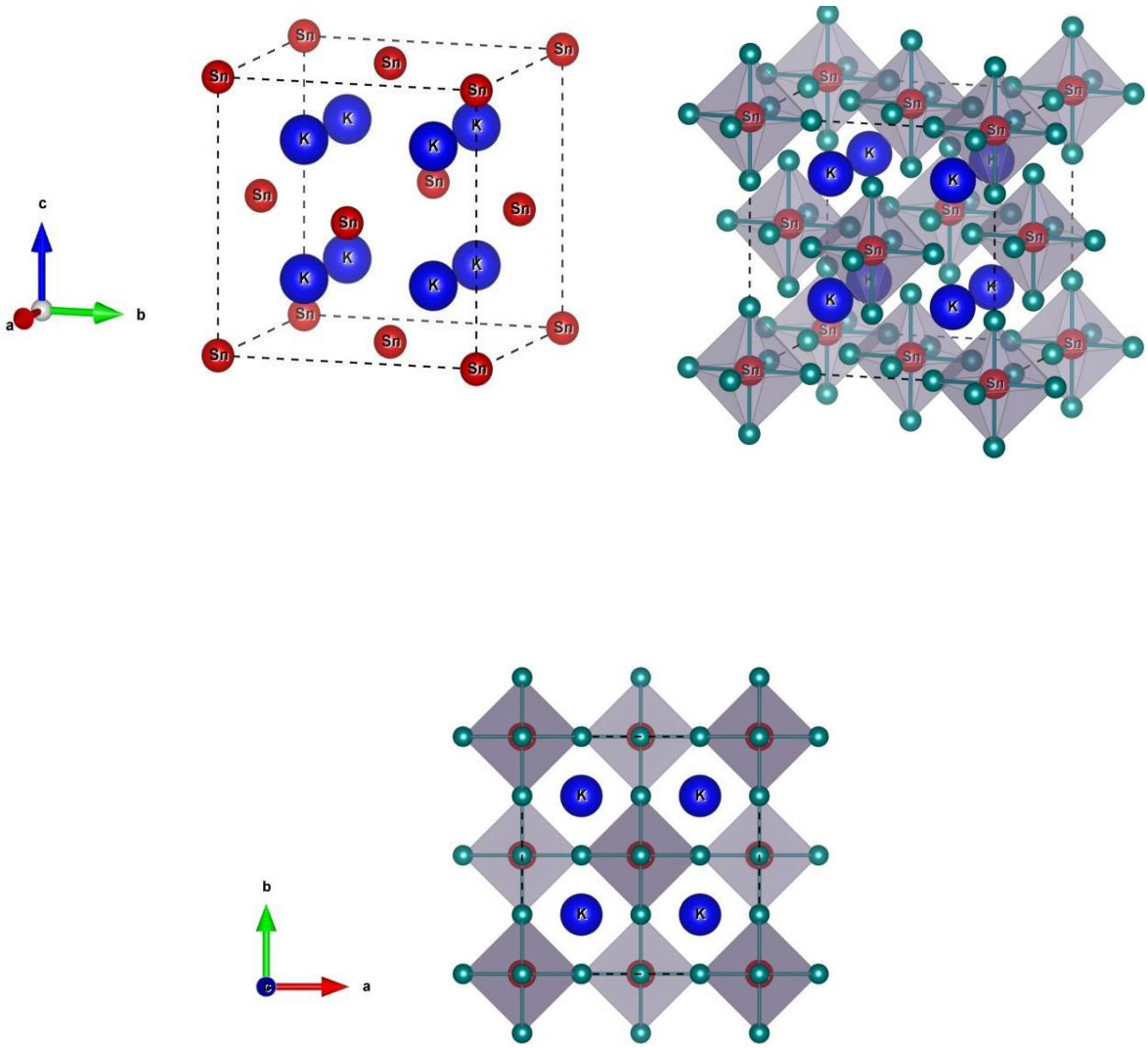

Figure. IV. 1: Representation of the cubic structure of K_2SnX_6 (X= Cl, Br, I): (a) without X; (b) Polyhedral structure (X atom is in green).

Table. IV. 1: Computed atomic positions of K_2SnX_6:(X= Cl, Br, I) in cubic phase.

Compound	atom	Atomic positions (cubic)
K_2SnCl_6	K	(0.25000000, 0.25000000, 0.25000000) (0.75000000, 0.75000000, 0.75000000)
	Sn	(0.00000000, 0.00000000, 0.00000000)
	Cl	(0.24541158, 0.00000000, 0.00000000) (0.75458842, 0.00000000, 0.00000000) (0.00000000, 0.24541158, 0.00000000) (0.00000000, 0.75458842, 0.00000000) (0.00000000, 0.00000000, 0.24541158) (0.00000000, 0.00000000, 0.75458842)
K_2SnBr_6	K	(0.25000000, 0.25000000, 0.25000000) (0.75000000, 0.75000000, 0.75000000)
	Sn	(0.00000000, 0.00000000, 0.00000000)
	Br	(0.24921708, 0.00000000, 0.00000000) (0.75078292, 0.00000000, 0.00000000) (0.00000000, 0.24921708, 0.00000000) (0.00000000, 0.75078292, 0.00000000) (0.00000000, 0.00000000, 0.24921708) (0.00000000, 0.00000000, 0.75078292)
K_2SnI_6	K	(0.25000000, 0.25000000, 0.25000000) (0.75000000, 0.75000000, 0.75000000)
	Sn	(0.00000000, 0.00000000, 0.00000000)
	I	(0.24665789, 0.00000000, 0.00000000) (0.75334211, 0.00000000, 0.00000000) (0.00000000, 0.24665789, 0.00000000) (0.00000000, 0.75334211, 0.00000000) (0.00000000, 0.00000000, 0.24665789) (0.00000000, 0.00000000, 0.75334211)

IV.3.2. The tetragonal phase (P4/mnc)

Description

Tetragonal K_2SnX_6 (X=Cl, Br, I) crystallizes in P4/mnc space group. It crystallizes in the tetragonal structure with two formula units per unit cell (18 atoms per unit cell).

K^{+1} is bonded in a eight-coordinate geometry to eight X^{-1} ions. There are four shorter and four longer K-X bond lengths as it is depicted in **Table. IV. 2**. Sn^{+4} is bonded in an octahedral geometry to six X^{-1} ions. There are four shorter and two longer Sn-Cl bond lengths (**Table. IV. 2)**.

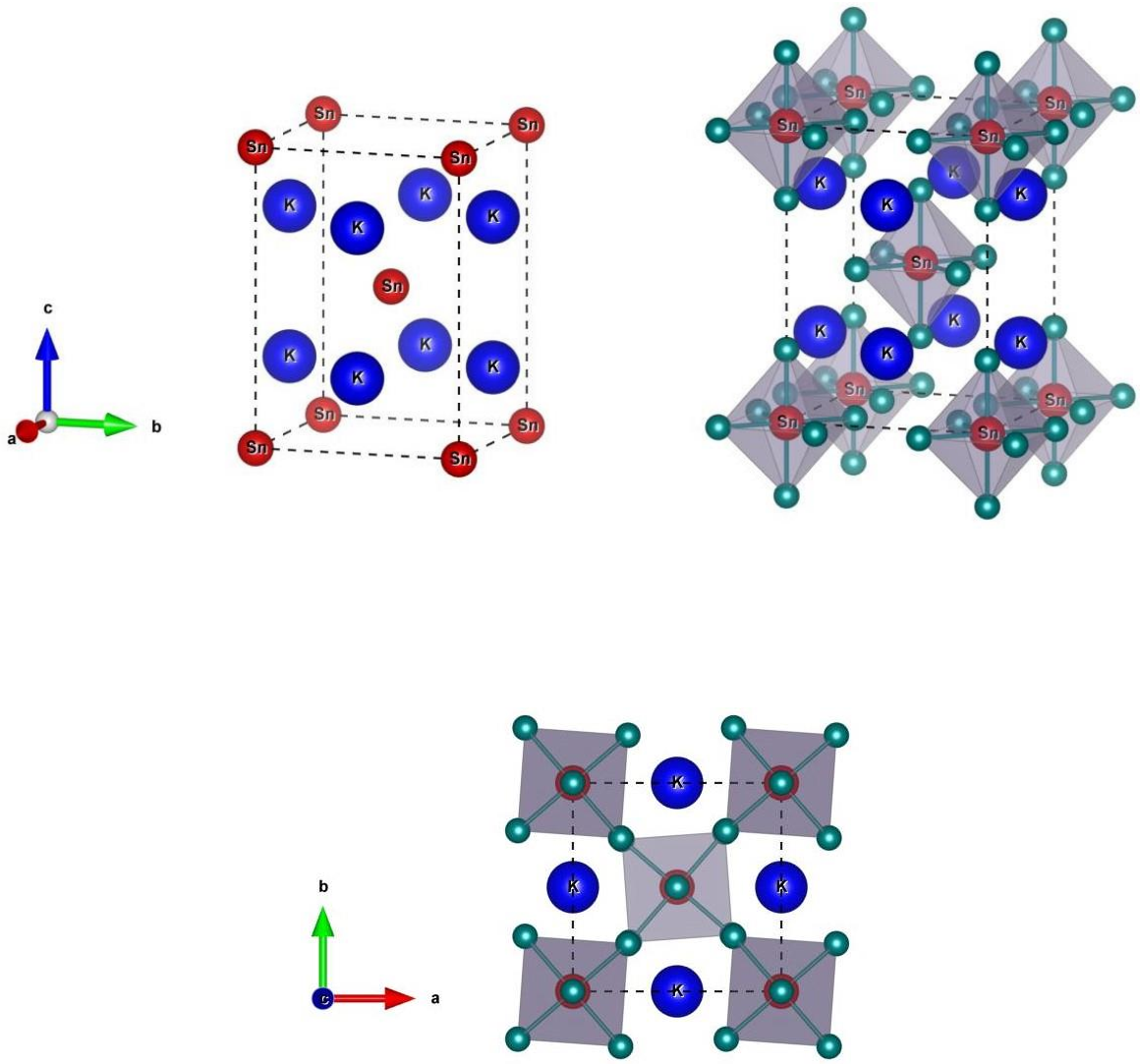

Figure. IV. 2: Representation of the tetragonal structure of K_2SnX_6 (X= Cl, Br, I): (a) without X; (b) Polyhedral structure (X atom is in green).

Table. IV. 2: Computed atomic positions of K_2SnX_6:(X= Cl, Br, I) in tetragonal phase.

Compound	atom	Atomic positions (tetragonal)
K_2SnCl_6	K	(0.50000000, 0.00000000, 0.00000000)
		(0.50000000, 0.00000000, 0.75000000)
		(0.00000000, 0.50000000, 0.25000000)
		(0.00000000, 0.50000000, 0.75000000)
	Sn	(0.00000000, 0.00000000, 0.00000000)
		(0.50000000, 0.50000000, 0.50000000)
	Cl	(0.26119472, 0.22801501, 0.00000000)
		(0.73880528, 0.77198499, 0.00000000)
		(0.77198499, 0.26119472, 0.00000000)
		(0.22801501, 0.73880528, 0.00000000)
		(0.23880528, 0.72801501, 0.50000000)
		(0.76119472, 0.27198499, 0.50000000)
		(0.27198499, 0.23880528, 0.50000000)
		(0.72801501, 0.76119472, 0.50000000)
	Cl	(0.00000000, 0.00000000, 0.24509595)
		(0.00000000, 0.00000000, 0.75490405)
		(0.50000000, 0.50000000, 0.74509595)
		(0.50000000, 0.50000000, 0.25490405)
K_2SnBr_6	K	(0.50000000, 0.00000000, 0.25000000)
		(0.50000000, 0.00000000, 0.75000000)
		(0.00000000, 0.50000000, 0.25000000)
		(0.00000000, 0.50000000, 0.75000000)
	Sn	(0.00000000, 0.00000000, 0.00000000)
		(0.50000000, 0.50000000, 0.50000000)
	Br	(0.26392305, 0.22886422, 0.00000000)
		(0.73607695, 0.77113578, 0.00000000)
		(0.77113578, 0.26392305, 0.00000000)
		(0.22886422, 0.73607695, 0.00000000)
		(0.23607695, 0.72886422, 0.50000000)
		(0.76392305, 0.27113578, 0.50000000)
		(0.27113578, 0.23607695, 0.50000000)
		(0.72886422, 0.76392305, 0.50000000)
	Br	(0.00000000, 0.00000000, 0.24576359)
		(0.00000000, 0.00000000, 0.75423641)
		(0.50000000, 0.50000000, 0.74576359)
		(0.50000000, 0.50000000, 0.25423641)

K_2SnI_6	K	(0.50000000, 0.00000000, 0.25000000) (0.50000000, 0.00000000, 0.75000000) (0.00000000, 0.50000000, 0.25000000) (0.00000000, 0.50000000, 0.75000000)
	Sn	(0.00000000, 0.00000000, 0.00000000) (0.50000000, 0.50000000, 0.50000000)
	I	(0.26306990, 0.22927567, 0.00000000) (0.73693010, 0.77072433, 0.00000000) (0.77072433, 0.26306990, 0.00000000) (0.22927567, 0.73693010, 0.00000000) (0.23693010, 0.72927567, 0.50000000) (0.76306990, 0.27072433, 0.50000000) (0.27072433, 0.23693010, 0.50000000) (0.72927567, 0.76306990, 0.50000000)
	I	(0.00000000, 0.00000000, 0.24527918) (0.00000000, 0.00000000, 0.75472082) (0.50000000, 0.50000000, 0.74527918) (0.50000000, 0.50000000, 0.25472082)

IV.3.3. Monoclinic phase ($P2_1/n$)

Description

Monoclinic K_2SnX_6 (X=Cl, Br, I) crystallizes in the monoclinic P21/n space group. It cristallizes in the monoclinic structure with two formula units per unit cell (18 atoms per unit cell).

K^{+1} is bonded in a 8-coordinate geometry to eight X^{-1} atoms. There are a spread of $K-X$ bond distances. Sn^{+4} is bonded in an octahedral geometry to six X^{-1}atoms. There are two shorter and four longer $Sn-X$ bond lengths.

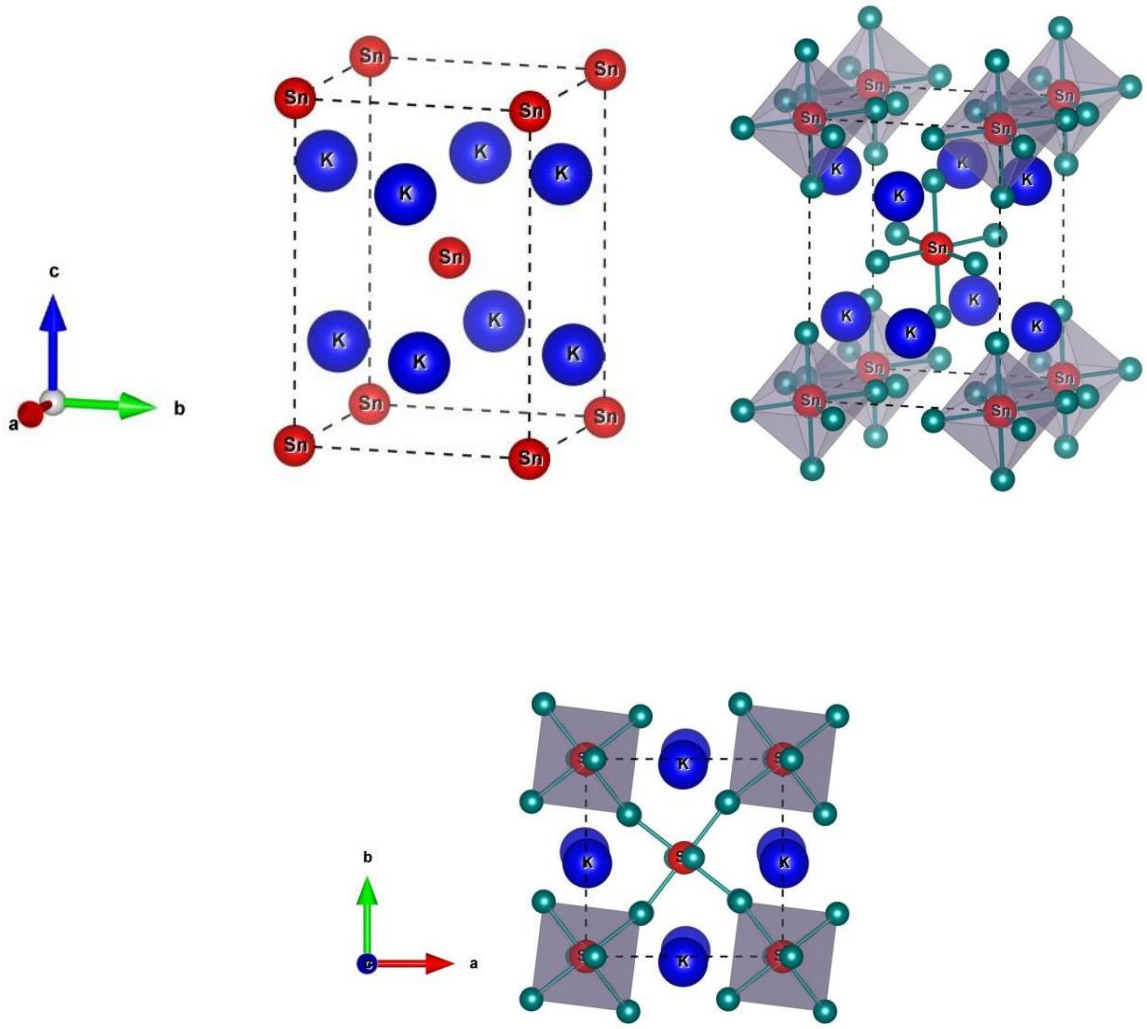

Figure. IV. 3 : Representation of the monoclinic structure of K_2SnX_6 (X= Cl, Br, I): (a) without X; (b) Polyhedral structure (X atom is in green).

Table. IV. 3 Computed atomic positions of K_2SnX_6:(X= Cl, Br, I) in monoclinic phase.

Compound	atom	Atomic positions (GGA)	Atomic positions (LDA)
K_2SnCl_6	K	(0.50565964, 0.02833677, 0.24328453)	(0.50560257, 0.02832600, 0.24161148)
		(0.49434036, 0.97166323, 0.75671547)	(0.49439743, 0.97167400, 0.75838852)
		(0.99434036, 0.52833677, 0.25671547)	(0.99439743, 0.52832600, 0.25838852)
		(0.00565964, 0.47166323, 0.74328453)	(0.00560257, 0.47167400, 0.74161148)
	Sn	(0.00000000, 0.00000000, 0.00000000)	(0.00000000, 0.00000000, 0.00000000)
		(0.50000000, 0.50000000,0.50000000)	(0.50000000, 0.50000000, 0.50000000)
	Cl	(0.27364449, 0.21422021, 0.97676213)	(0.27412822, 0.21278134, 0.97651637)
		(0.72635551, 0.78577979, 0.02323787)	(0.72587178, 0.78721866, 0.02348363)
		(0.22635551, 0.71422021, 0.52323787)	(0.22587178, 0.71278134, 0.52348363)
		(0.77364449, 0.28577979, 0.47676213)	(0.77412822, 0.28721866, 0.47651637)
	Cl	(0.21201502, 0.72380272, 0.98028404)	(0.21139308, 0.72544065, 0.98053621)
		(0.78798498, 0.27619728, 0.01971596)	(0.78860692, 0.27455935, 0.01946379)
		(0.28798498, 0.22380272, 0.51971596)	(0.28860692, 0.22544065, 0.51946379)
		(0.71201502, 0.77619728, 0.48028404)	(0.71139308, 0.77455935, 0.48053621)
	Cl	(0.04278908, 0.99966650, 0.24312417)	(0.04320727, 0.99921943, 0.24295356)
		(0.95721092, 0.00033350, 0.75687583)	(0.95679273, 0.00078057, 0.75704644)
		(0.45721092, 0.49966650, 0.25687583)	(0.45679273, 0.49921943, 0.25704644)
		(0.54278908, 0.50033350, 0.74312417)	(0.54320727, 0.50078057, 0.74295356)
K_2SnBr_6	K	(0.50653930, 0.02827698, 0.24213379)	(0.51014945, 0.05832155, 0.24810018)
		(0.49346070, 0.97172302, 0.75786621)	(0.48985055, 0.94167845, 0.75189982)
		(0.99346070, 0.52827698, 0.25786621)	(0.98985055, 0.55832155, 0.25189982)
		(0.00653930, 0.47172302, 0.74213379)	(0.01014945, 0.44167845, 0.74810018)
	Sn	(0.00000000, 0.00000000, 0.00000000)	(0.00000000, 0.00000000, 0.00000000)
		(0.50000000, 0.50000000, 0.50000000)	(0.50000000, 0.50000000, 0.50000000)
	Br	(0.27720669, 0.21618793, 0.97687889)	(0.28756990, 0.19731922, 0.96199186)
		(0.72279331, 0.78381207, 0.02312111)	(0.71243010, 0.80268078, 0.03800814)
		(0.22279331, 0.71618793, 0.52312111)	(0.21243010, 0.69731922, 0.53800814)
		(0.77720669, 0.28381207, 0.47687889)	(0.78756990, 0.30268078, 0.46199186)
	Br	(0.21505996, 0.72195655, 0.98125182)	(0.19331600, 0.70873863, 0.96832482)
		(0.78494004, 0.27804345, 0.01874818)	(0.80668400, 0.29126137, 0.03167518)
		(0.28494004, 0.22195655, 0.51874818)	(0.30668400, 0.20873863, 0.53167518)
		(0.71505996, 0.77804345, 0.48125182)	(0.69331600, 0.79126137, 0.46832482)
	Br	(0.04347127, 0.99951273, 0.24512571)	(0.07211840, 0.99125571, 0.24178815)
		(0.95652873, 0.00048727, 0.75487429)	(0.92788160, 0.00874429, 0.75821185)
		(0.45652873, 0.49951273, 0.25487429)	(0.42788160, 0.49125571, 0.25821185)

		(0.54347127, 0.50048727, 0.74512571)	(0.57211840, 0.50874429, 0.74178815)
K_2SnI_6	K	(0.50740102, 0.06480694, 0.24271751)	(0.50700000, 0.02500000, 0.24100000)
		(0.49259898, 0.93519306, 0.75728249)	(0.49300000, 0.97500000, 0.75900000)
		(0.99259898, 0.56480694, 0.25728249)	(0.99300000, 0.52500000, 0.25900000)
		(0.00740102, 0.43519306, 0.74271751)	(0.00700000, 0.47500000, 0.74100000)
	Sn	(0.00000000, 0.00000000, 0.00000000)	(0.00000000, 0.00000000, 0.00000000)
		(0.50000000, 0.50000000, 0.50000000)	(0.50000000, 0.50000000, 0.50000000)
	I	(0.28429956, 0.19209609, 0.95769045)	(0.27100000, 0.21100000, 0.97900000
		(0.71570044, 0.80790391, 0.04230955)	(0.72900000, 0.78900000, 0.02100000
		(0.21570044, 0.69209609, 0.54230955)	(0.22900000, 0.71100000, 0.52100000
		(0.78429956, 0.30790391, 0.45769045)	(0.77100000, 0.28900000, 0.47900000
	I	(0.18542494, 0.71155300, 0.96338218)	(0.21800000, 0.72900000, 0.98500000
		(0.81457506, 0.28844700, 0.03661782)	(0.78200000, 0.27100000, 0.01500000
		(0.31457506, 0.21155300, 0.53661782)	(0.28200000, 0.22900000, 0.51500000
		(0.68542494, 0.78844700, 0.46338218)	(0.71800000, 0.77100000, 0.48500000
	I	(0.08206899, 0.98539973, 0.23983421)	(0.04100000, 0.99900000, 0.24000000
		(0.91793101, 0.01460027, 0.76016579)	(0.95900000, 0.00100000, 0.76000000
		(0.41793101, 0.48539973, 0.26016579)	(0.45900000, 0.49900000, 0.26000000
		(0.58206899, 0.51460027, 0.73983421)	(0.54100000, 0.50100000, 0.74000000

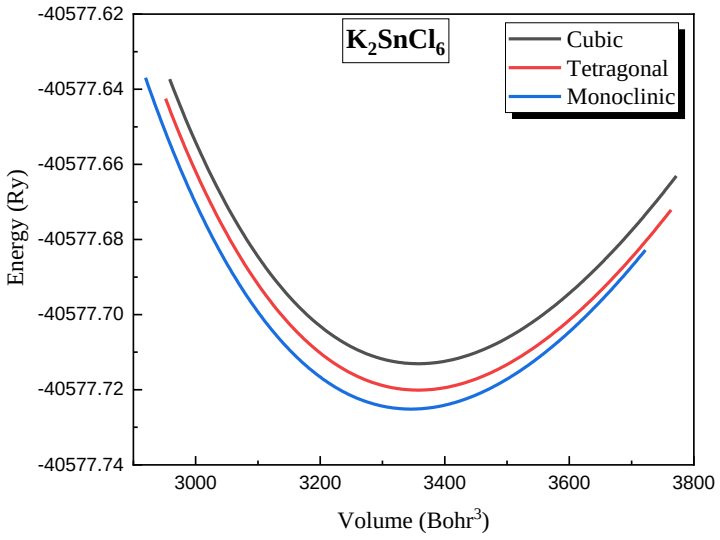

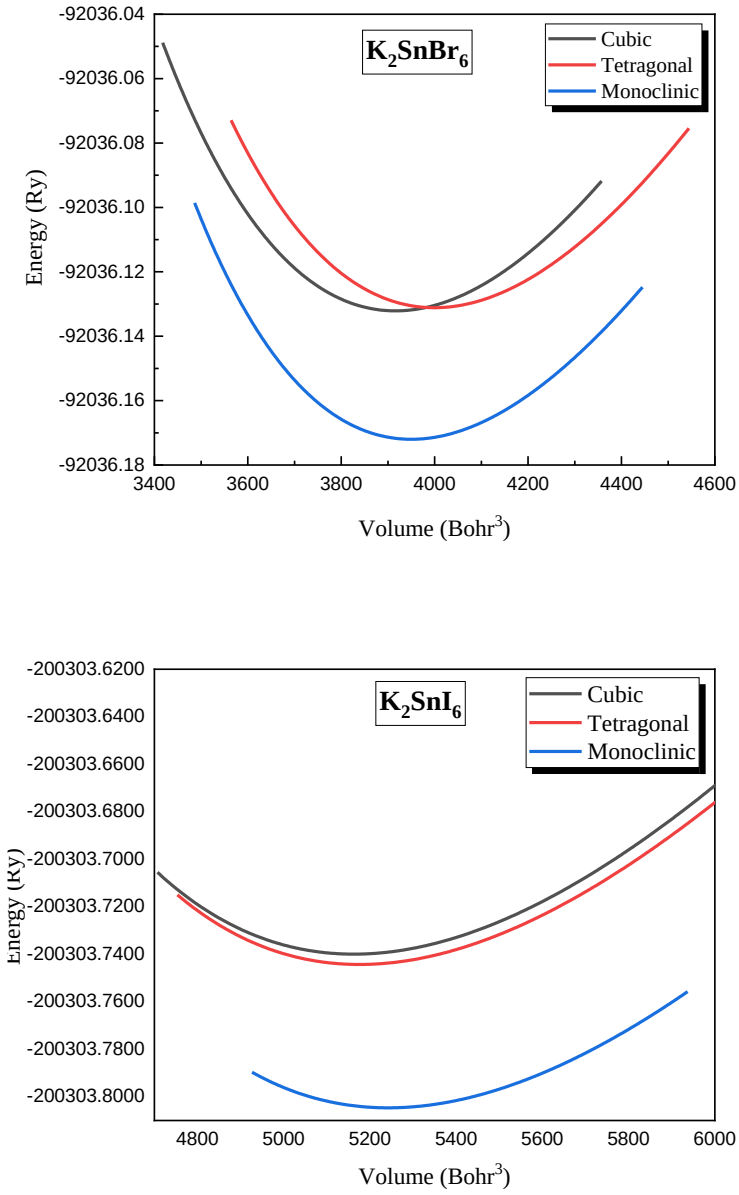

Figure. IV. 4: Total energy of a unit cell in terms of its volume computed for the compounds K_2SnX_6 (X=Cl, Br, I), in: cubic (black line), tetragonal(red line), and monoclinic(blue line) phases.

Table. IV. 4: Computed and experimental lattice parameters values

Materials	Phases	Calculated parameters by GGA-PBEsol	Calculated parameters by LDA	Calculated parameters by GGA-PBE [9]	Experimental parameters [6], [7]
K_2SnCl_6	**Cubic**	a = 9.9834 Å B =36.0755 GPa B' =5.0474 V_0 =995.028080 Å^3 E_{min} = -20288.856533 Ryd		a = 10.02Å	a = 9.99 Å
	Tetragonal	a =b= 7.0599 Å, c = 9.9963 Å B = 35.7786 GPa B'=4.9392 V_0 = 498.2343 Å^3 E_{min} = - 40577.720090 Ryd		a = b=7.09Å, c = 10.01 Å	a =b= 7.06 Å, c= 9.98 Å
	Monoclinic	a = 7.0399 Å, b = 7.0299 Å, c = 10.0183 Å, β = 90.23° B = 36.1102 GPa B'=4.9442 V_0 = 494.8939 Å^3 E_{min} = - 40577.725147 Ryd	a = 6.94 Å, b = 6.93Å c = 9.87Å, β = 90.41°	a = 7.07 Å, b = 7.05 Å, c = 10.03 Å, β = 90.11°	a = 7.02 Å, b = 7.01 Å, c = 9.99 Å, β = 90.13°
K_2SnBr_6	**Cubic**	a = 10.5091 Å B = 29. 2572 GPa B'=4.9089 V_0 = 1160.637737 Å^3 E_{min} = - 46018.066061 Ryd		a = 10.51 Å	a = 10.48 Å
	Tetragonal	a = b = 7.4687 Å, c = 10.6268 Å B = 28.3798 GPa B'=5.0768 V_0 = 592.7842 Å^3 E_{min} = - 92036.131139 Ryd		a = b = 7.50 Å, c = 10.67 Å	
	Monoclinic	a = 7.4228 Å , b = 7.4328 Å, c = 10.6097 Å, β = 90.42° B = 29.2196 GPa	a = 7.30 Å, b = 7.37 Å c = 10.44 Å, β = 90.36°	a = 7.45 Å, b = 7.47 Å, c = 10.68 Å, β = 90.17°	a = 7.43 Å, b = 7.44 Å, c = 10.62 Å, β =90.18°

		B'=6.0121 V_0 = 585.3447 Å^3 E_{min} = - 92036.172004 Ryd		
K_2SnI_6	**Cubic**	a = 11.5230 Å B = 20.7168 GPa B'=5.2102 V_0 = 1530.0188 Å^3 E_{min} = - 100151.869977 Ryd		a = 11.66 Å
	Tetragonal	a = b = 8.1334 A, c = 11.5938 Å B = 20.7228 GPa B'=5.4586 V_0 = 767.0450 Å^3 E_{min} = - 200303.744305 Ryd		a = b = 8.25 Å , c = 11.76 Å
	Monoclinic	a = 8.1866 Å, b = 8.2532 Å, c = 11.4979 Å, β = 90.50° B = 20.2292 GPa B'=5.4260 V_0 = 776.833563 Å^3 E_{min} = - 200303.804663 Ryd	a = 8.03 Å, b = 8.06 Å c = 11.55 Å, β = 90.73°	a = 8.29 Å, b = 8.32 Å, c = 11.69 Å , β = 90.25°

Table. IV. 5: Interatomic distances

compound	phase	atoms	GGA	LDA
K_2SnCl_6	Cubic	Sn-Cl	2.450 Å	
		Sn-K	4.323 Å	
		K-Cl	3.529 Å	
		K-K	4.991 Å	
		Cl-Cl	3.465 Å	
	Tetragonal	Sn-Cl	2x2.450 Å /4x2.448 Å	
		Sn-K	4.325 Å	
		K-Cl	4x3.530 Å /4x 3.65 Å	
		K-K	4.998 Å	
		Cl-Cl	3.463 Å	
	Monoclinic	Sn-Cl	2x2.449 Å /4x2.457 Å	2x2.524 Å /2x2.527 Å
		Sn-K	4.308 Å	/2x2.518 Å
		K-Cl	3.192 Å -3.500 Å	
		K-K	4.920 Å	3.267 Å -3.626 Å
		Cl-Cl	3.466 Å	
K_2SnBr_6	Cubic	Sn-Br	2.619 Å	
		Sn-K	4.551 Å	
		K-Br	3.716 Å	
		K-K	5.255 Å	
		Br-Br	3.704 Å	
	Tetragonal	Sn-Br	2x2.612 Å /4x 2.609 Å	
		Sn-K	4.583 Å	
		K-Br	4x3.734 Å / 4x3.618 Å	
		K-K	5.208 Å	
		Br-Br	3.691 Å	
	Monoclinic	Sn-Br	2x2.618 Å /4x2.62 Å	2x2.709 Å /4x2.707 Å
		Sn-K	4.448 Å	
		K-Br	3.366 Å -3.711 Å	3.386 Å -3.747 Å
		K-K	5.186 Å	
		Br-Br	3.712 Å	
K_2SnI_6	Cubic	Sn-I	2.842 Å	
		Sn-K	4.989 Å	
		K-I	4.074 Å	
		K-K	5.762 Å	
		I-I	4.020 Å	
	Tetragonal	Sn-I	2x2.844 Å / 4x2.838 Å	
		Sn-K	4.994 Å	
		K-I	4x4.067 Å / 4x3.949 Å	
		K-K	5.751 Å	
		I-I	4.018 Å	
	Monoclinic	Sn-I	2x2.835 Å /4x2.86 Å	2x2.916 Å /2x2.989 Å /
		Sn-K	4.654 Å / 4.953 Å	2x2.955 Å
		K-I	3.543 Å -3.933 Å	
		K-K	5.729 Å	3.848 Å -4.098 Å
		I-I	4.033 Å	

The lattice parameters of K_2SnX_6 (X= Cl, Br, I) increases from Cl to Br to I with a decrease in the compressibility modulus *B*. Interestingly, the compressibility modulus *B* remains relatively stable when transitioning from cubic to tetragonal to monoclinic phases for each of these compounds.

IV.4. Electronic properties

In this section, we present the electronic properties of the three compounds under study, which include band structures and density of states.

IV.4.1. Band structure

The discrete energy levels of isolated electrons split and form allowed bands interspersed with forbidden bands when these atoms are brought close together in a crystal. The most meaningful description of the energy bands available to the electrons is carried out in reciprocal space or the wave vector space k. This description is generally simplified by considering variations in energy E as a function of k along the directions of highest symmetry in the first Brillouin zone.

One of the fundamental characteristics we can extract from the band structure is the **band gap**. It serves as a method for evaluating the suitability of materials in relation to their prospective use in solar power cells along with other optoelectronic equipment.

In the current work, once the structural optimization was completed, we used the collected information (ground state lattice parameters) to perform a self-consistent cycle, allowing us to determine the energy bands of our materials. The band structures of K_2SnX_6 (X = Cl, Br, or I) were determined using the PBEsol-GGA functional **[2,3]. A**dditionally, in order to improve the bandgap estimation, the modified Becke-Johnson potential (mBJ) **[4]** was employed. The band structures of the three compounds were computed using a selected k-path of Z – C – D – Γ – Y – A – Γ - E within the Brillouin zone. The profiles of the band structures are depicted in **Figure. IV. 5.**

Table. IV. 6 presents the estimated bandgaps alongside other calculated gap energy for comparison. The band gaps, as determined using the mBJ-GGA potential, exhibit a descending trend, with values of 4.126 eV, 2.581 eV, and 1.707 eV for K_2SnCl_6, K_2SnBr_6, and K_2SnI_6, respectively. In addition, the medium values of bandgap for K_2SnBr_6, and K_2SnI_6 gives the compounds the property of being semiconductors material. The calculated band gaps of K_2SnX_6 (X= Cl, Br, I) exhibit considerable importance for future investigations because of their strong agreement with the theoretical band gaps **[9]** of 4.04 eV and 2.57 eV to 1.16 eV, respectively.

The valence band maximum (VBM) and conduction band minimum (CBM) of K_2SnCl_6 and K_2SnBr_6 are located at the identical high-symmetry special point of the Brillouin zone Γ. This observation establishes that investigated K_2SnCl_6 and K_2SnBr_6 possess the characteristic of being direct band gap. Whereas, for K_2SnI_6 the valence band maximum is located at point Y of the BZ and conduction band minimum is located at point Γ, so that, it exhibits an indirect bandgap.
The band gaps of K_2SnX_6 (X= Br, I) exhibit favourable characteristics for implementation in single-junction and tandem photovoltaic cells, as well as various other optoelectronic uses.

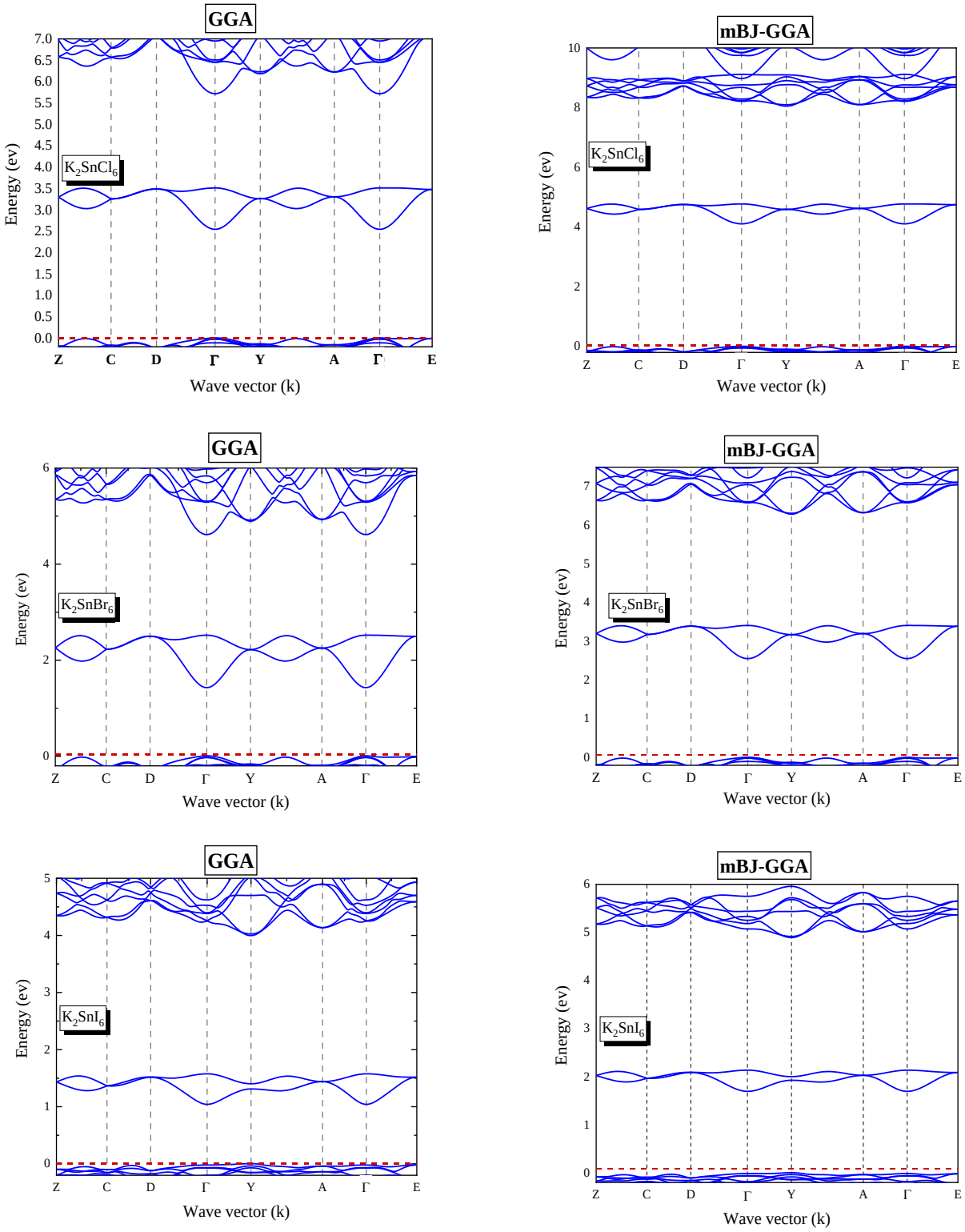

Figure. IV. 5: Band structure of K_2SnX_6 (X= Cl, Br, I) computed with GGA and mBJ-GGA functionals

Table. IV. 6: Computed band gaps E_g compared to theoretical results

	Eg		
Compounds	PBEsol-GGA	mBJ-PBEsol-GGA	Theoretical **[9]**
K_2SnCl_6	2.577 eV	4.126 eV	4.04 eV
K_2SnBr_6	1.465 eV	2.581 eV	2.57 eV
K_2SnI_6	1.060 eV	1.707 eV	1.16 eV

IV.4.1.1. The effective mass

The concept of effective mass and its relationship to band curvature is particularly relevant in the study of electronic transport properties, such as charge carrier mobility. Materials with flat bands (large effective masse) may exhibit unique electronic and transport behaviors, and understanding these properties is essential for various applications in electronics and materials science.

The effective mass of a carrier (m*) denotes the mass of an electron or hole in a solid when subjected to an external electrostatic force. It correlates with the curvature of the valence and conduction bands in the electronic band structure and is expressed in units of the rest mass of an electron (m_0). Predictions about whether a material will have a light or heavy effective mass for electrons or holes can be made based on the curvature of the conduction band minimum (CBM) or valence band maximum (VBM), respectively.

The parabolic model, assuming isotropy at the CBM or VBM, is a valuable tool for describing effective mass. The effective mass can be computed using the $E(k)$ relationship with the formula:

$$\frac{1}{m^*} = \frac{1}{\hbar^2}\frac{\partial^2 E}{\partial k^2} \qquad \text{(IV-5)}$$

Where energy and effective mass are inversely proportional at the wave vector (k).

Effective mass calculations, detailed in **Table. IV. 7**, reveal that electron effective masses are smaller compared to hole effective masses for all the studied compounds K_2SnX_6 (X= Cl, Br, I).

Table. IV. 7: Computed effective mass using PBEsol-GGA and mBJ- PBEsol-GGA approximations

	mBJ-GGA		**GGA**	
	$m_h^*\ (m_0)$	$m_e^*\ (m_0)$	$m_h^*\ (m_0)$	$m_e^*\ (m_0)$
K_2SnCl_6	-3.55	0.92	-2.77	0.59
K_2SnBr_6	-2.5	0.62	-2.15	0.44
K_2SnI_6	-3.11	1.14	-2.91	0.75

IV.4.2. Density of state

The density of electronic states (DOS) is an essential quantity for calculating the energy distribution of electrons in the valence and conduction bands. The DOS is used for a quick visual analysis of the energy band structure. It is often useful to know whether the main peaks in the DOS are of s, p, or d character. Analyses of partial density of states (PDOS) can address this issue by allowing the calculation of the contribution of each atomic orbital to a given energy band.

The determination of the total and partial density of states (DOS) for the three compounds under investigation has been carried out using the mBJ-PBEsol-GGA functional. This analysis was conducted in order to gain a deeper understanding of the intricate electronic characteristics of these compounds, as it is depicted in **Figures. 4 (a)-(c).**

The partial density of states (DOS) of K_2SnCl_6, K_2SnBr_6, and K_2SnI_6 exhibits certain shared properties.

The three compounds' valence band maximums (VBMs) are mostly determined by the p states of the halogen atoms (Cl-3p or Br-4p and I-5p).

On the other hand, the s states of Tin and the p states of the halogen atoms make up the majority of the conduction band minimum (CBM).

Moreover, it is evident that potassium has very little effect on the valence band maximum (VBM) and conduction band minimum (CBM).

The valence band (VB) is divided into three bands. The two lower bands (at -5.5 eV and -3 eV to EF approximately) are primarily formed by Sn-s and X-p states, and an upper band (at -1 eV approximately) is dominated by X-p states. The Sn-s electrons are closely associated with the X-p states, indicating sp_3 hybridization within the covalently bonded complex [SnX_6] structure.

Potassium (K) does not contribute to the valence band, indicating that K is ionized to K^+. Therefore, K_2SnX_6 exhibits characteristics of an ionic bond between K^+ ions and $[SnX_6]$ complex.

The conduction band is dominated by the s states of potassium (K) atoms. The results obtained are in good agreement with previous studies **[9]**.

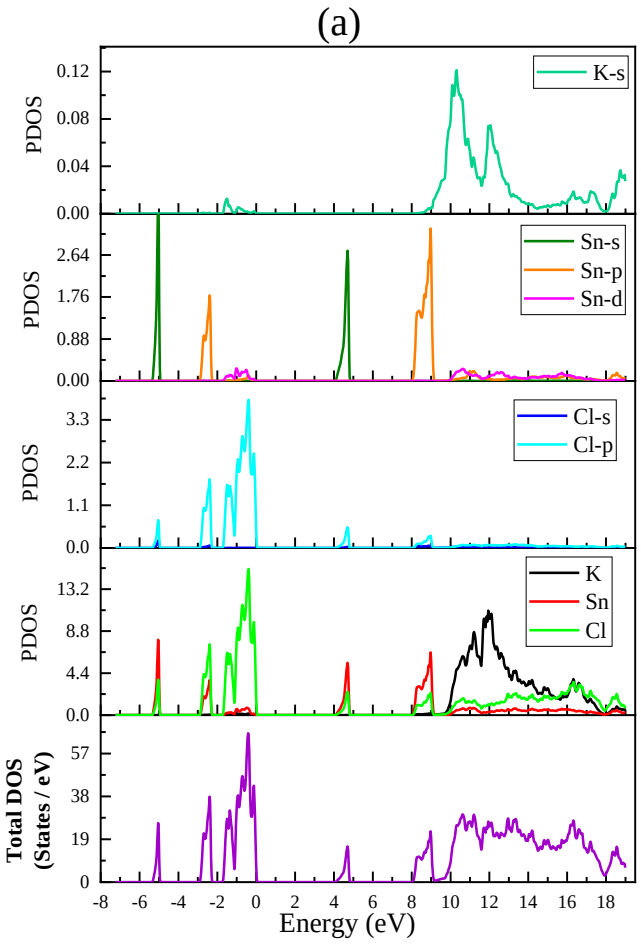

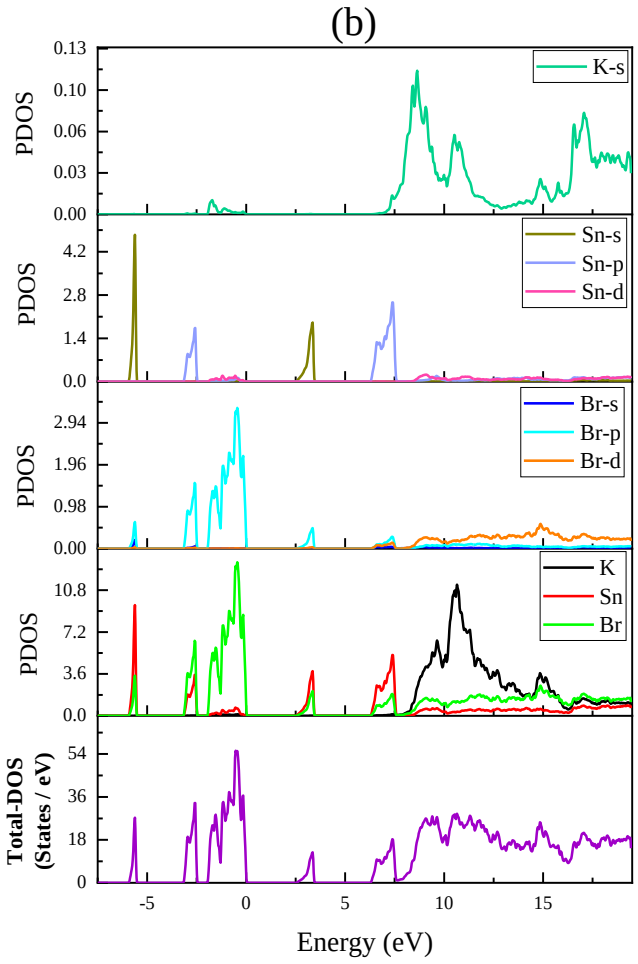
(b)
PDOS
K-s
Sn-s
Sn-p
Sn-d
Br-s
Br-p
Br-d
K
Sn
Br
Total-DOS
(States / eV)
Energy (eV)

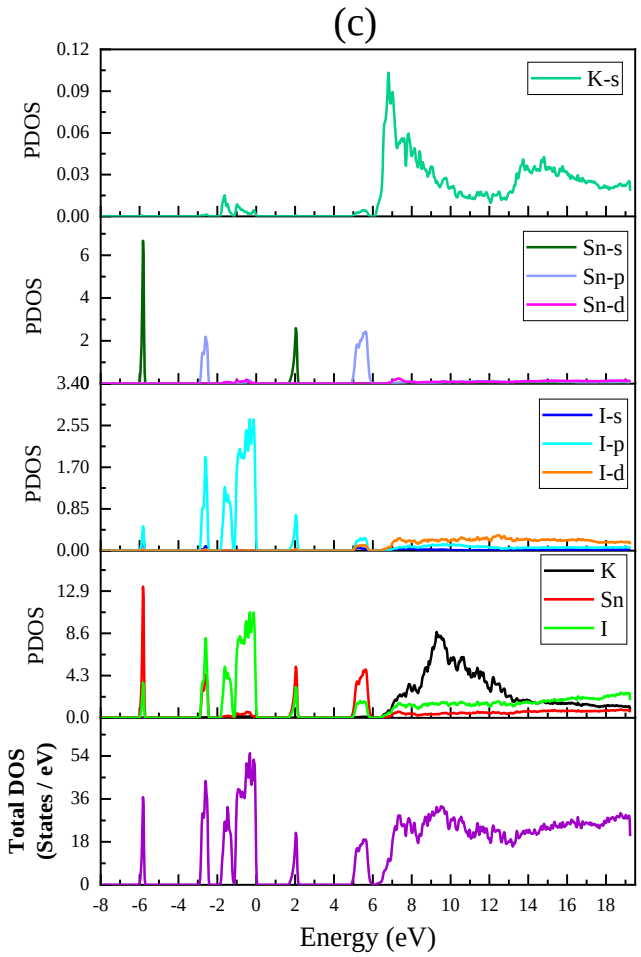

Figure. IV. 6: Total and partial density of state DOS of the monoclinic phase, computed by mBJ-GGA functional of: (a) K_2SnCl_6, (b) K_2SnBr_6, (c) K_2SnI_6.

IV.5. Optical properties

IV.5.1. Introduction

The study of optical properties in solids holds significant importance, encompassing both fundamental research and practical applications in various industries. While fundamental research seeks to understand the origins and characteristics of different excitation processes, industrial applications utilize this knowledge in optoelectronic devices. This broad spectrum of interests necessitates a synergy between experimental observations and theoretical frameworks, highlighting the need for reliable theoretical concepts to support these endeavors.

The study of the optical properties of a material can be conducted by examining its response to various external stimuli. In the following, we will focus specifically on the response of a system to light radiation and explore the resulting optical properties.

Interactions between radiation and matter, as is the case in optoelectronic components, are more appropriately described using a particle representation of radiation. Einstein suggested that the energy of radiation is not spread throughout space but concentrated in certain regions, propagating like particles that he called photons. The energy of a photon is given by:

$$E = h\nu = \hbar\omega \qquad \text{(IV-6)}$$

IV.5.2. Optical transitions

Due to the energy provided externally, electrons move from the valence band to the conduction band and vice versa. A portion of this energy is brought about by the interaction of electrons with the surrounding electromagnetic energy, specifically with photons. Indeed, an electron in the conduction band with energy E_1 can descend to the valence band of free states with energy E_2 by, spontaneously, emitting a photon with energy $h\nu = E_1 - E_2$. Conversely, an electron can move from the valence band to the conduction band by absorbing a photon with energy $h\nu$. The transition of an electron from one band to another through photon emission is commonly known as radiative recombination (recombination of an electron with a hole). During radiative recombination, there is conservation of energy and conservation of the wave vector.
In the case of compounds with direct band gaps, recombination is direct without a change in the wave vector (**Figure. IV. 7 left**). For materials with indirect band gaps, when an electron emits a photon, it must emit or absorb a lattice vibration called a phonon with energy E_{ph}. The phonon can have a wave vector of the same order of magnitude as that of electrons, facilitating the electron's transition from the bottom of the conduction band to the top of the valence band (**Figure. IV. 7 right**). In the case of materials with direct band gaps, they are much more suitable for optoelectronics because the rate of photon emission is much higher in these materials.

In a direct gap, the emission process involves only a photon, unlike in a material with an indirect gap **(Figure. IV. 7 right**) where a phonon and then a photon are involved. Electronic transitions are thus coupled with the vibrational transitions of systems. This process is less probable **[10]**.

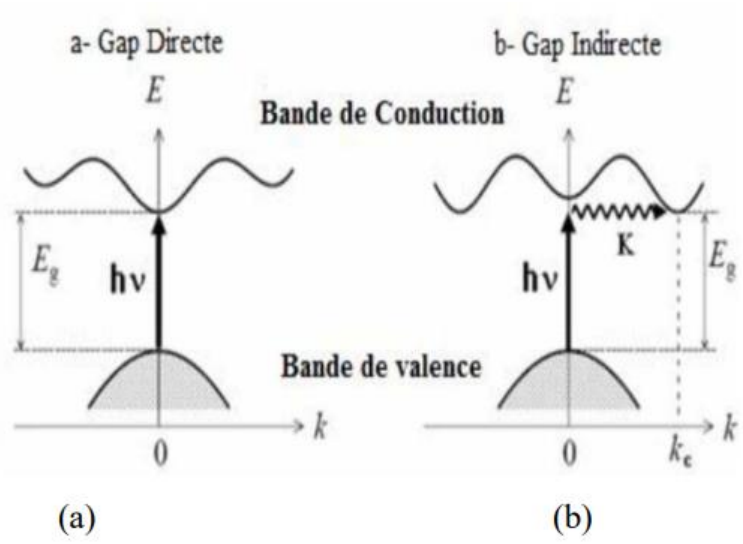

Figure. IV. 7: Transitions inter bandes a) Direct gap b) Indirect Gap **[10]**

IV.5.3. Theoretical study of optical properties

The optical characteristics of solids stem from how their electron system reacts to the changing electromagnetic field induced by incident light. Understanding these properties involves determining a response function. Linear optical properties are determined by the complex dielectric function $\varepsilon(\omega)$. However, deriving an exact expression for this function is challenging, leading to the use of approximations. One common approximation within this framework is the Random Phase Approximation (RPA) **[44]**.

The dielectric function is given by the expression

$$\varepsilon(\omega) = \varepsilon_1(\omega) + i\varepsilon_2(\omega) \qquad \text{(IV-7)}$$

where ε_1 (ω) is the real part and ε_2 (ω) is the imaginary part. The imaginary part $\varepsilon_2(\omega)$ reflects the material's absorption, while the real part $\varepsilon_1(\omega)$ is related to the polarization of the medium.

To compute the frequency-dependent dielectric function, ε(ω), we rely on obtaining energy eigenvalues and electron wave functions. These quantities are typically yielded as natural outcomes when calculating the band structure.

Imaginary part of the dielectric function

The imaginary part can be computed utilizing the expression provided in Reference **[44,45]:**

$$\varepsilon_2^{\alpha\beta}(\omega) = \frac{\hbar^2 e^2}{\pi m^2 \omega^2} \sum_{c,v} \int d^3k \langle c_k | P^\alpha | v_k \rangle \langle v_k | P^\beta | c_k \rangle \delta(\varepsilon_c^k - \varepsilon_v^k - \omega) \qquad \text{(IV-8)}$$

Real part of the dielectric function

The real part of the dielectric function $\varepsilon_1(\omega)$ can be extracted from the imaginary part $\varepsilon_2(\omega)$ using the Kramers-Kronig relations: **[13]**:

$$\varepsilon_1(\omega) = Re\varepsilon(\omega) = 1 + \frac{2}{\pi} P \int_0^{+\infty} \frac{\omega' \varepsilon_2(\omega')}{\omega'^2 - \omega^2} \, d\omega' \quad \text{(IV-9)}$$

Where ω is the frequency, and P is the principal part of the Cauchy integral, defined as:

$$P = \lim_{\alpha \to 0} \int_{-\infty}^{\omega - a} \frac{\varepsilon_2(\omega')}{\omega' - \omega} d\omega' + \int_{\omega + a}^{+\infty} \frac{\varepsilon_2(\omega')}{\omega' - \omega} d\omega' \quad \text{(IV-10)}$$

2-The absorption coefficient of light (α):

an optical medium is characterized by its absorption coefficient α. This is defined as the fraction of light absorbed in a unit length of the medium. If the ray propagates in the z direction, and the intensity at a position z is $I(z)$, the decay of intensity over a material of thickness dz is given by **[11]**:

$$dI = -\alpha \, dz . I(z) \quad \text{(IV-11)}$$

This can be integrated to obtain the Beer-Lambert law:

$$I(z) = I_0 e^{-\alpha z} \quad \text{(IV-12)}$$

Where I_0 is the optical intensity at $z = 0$. The absorption is dependent on the frequency of the light wave.

The absorption coefficient α(ω) obtained directly from the relation **[14,15]**:

$$\alpha(\omega) = \frac{\sqrt{2}}{c} \omega \sqrt{-\varepsilon_1(\omega) + \sqrt{\varepsilon_1(\omega)^2 + \varepsilon_2(\omega)^2}} \quad \text{(IV-13)}$$

3-The refractive index:

If a plane wave propagates through two media with different dielectric constants, it will be divided into two waves: a reflected wave and a refracted wave. The complex refractive index $N(\omega)$ is given by **[14,15]**:

$$N(\omega) = n(\omega) + ik(\omega) \quad \text{(IV-14)}$$

$n(\omega)$: being "the real refractive index".

$k(\omega)$: is the attenuation index, also called "the extinction coefficient".

From Fresnel equations:

$$n(\omega) = \left(\frac{\varepsilon_1(\omega)}{2} + \frac{\sqrt{\varepsilon_1(\omega)^2+\varepsilon_2(\omega)^2}}{2}\right)^2 \quad \text{(IV-15)}$$

In the other hand, and using Kramer and Kronig relations, the refractive index and the extinction coefficient can be expressed by **[46]**:

$$n(\omega) = 1 + \frac{2}{\pi} P \int_0^{+\infty} \frac{\omega' k(\omega')}{\omega'^2-\omega^2}\, d\omega' \quad \text{(IV-16)}$$

$$k(\omega) = -\frac{2\omega}{\pi} P \int_0^{+\infty} \frac{n(\omega')-1}{\omega'^2-\omega^2}\, d\omega' \quad \text{(IV-17)}$$

To better explain the physical consequences of these relations, let's simplify equation (IV-19) by writing it for $\omega = 0$ ($E = 0$):

$$n(0) = n_0 = 1 + \frac{2}{\pi}\int_0^{+\infty} \frac{k(\omega')}{\omega'} d\omega' \quad \text{(IV-18)}$$

The equation (IV-24) shows that n_0, also known as "the zero-loss index", is related to the integral over $k(\omega)$ across the entire spectrum, with a weighting factor of $\frac{1}{\omega'}$ From this formula, we deduce that the larger the compound's absorption, the stronger will be n_0. Additionally, due to the weighting factor $\frac{1}{\omega'}$, the more this absorption is situated at a low frequency ($\frac{1}{\omega'}$ large), the more significant the increase in n_0 will be

4- The reflectivity coefficient:

for normal incidence of radiation on the surface of a solid, the reflectivity coefficient is written as:

$$R = \left|\frac{N-1}{N+1}\right|^2 = \frac{(n-1)^2+k^2}{(n+1)^2+k^2} \quad \text{(IV-19)}$$

For $k = 0$, N is real, and the reflection coefficient becomes:

$$R = \left|\frac{N-1}{N+1}\right|^2 = \frac{(n-1)^2}{(n+1)^2} \quad \text{(IV-20)}$$

The reflectivity spectrum $R(\omega)$ for normal incidence on the surface of a crystal is deduced from the relation:

$$R = \left|\frac{\sqrt{\varepsilon(\omega)-1}}{\sqrt{\varepsilon(\omega)+1}}\right|^2 \quad \text{(IV-21)}$$

IV.5.4. Determination of the Dielectric Function by the Wien2k Code

To accurately represent optical properties, it is necessary to use the finest possible sampling of the Brillouin zone. To achieve this, after calculating the electronic structure through self-consistent field (SCF) procedures, the calculation of eigenvalues Ei and corresponding eigenvectors $|\varphi_{ik}\rangle$ is performed for a large number of *k* points.

We will now detail the method used in *Wien2k* for calculating the dielectric function, referring to **Figure. IV. 8.**

- The "**optic**" routine calculates, for each *k* point and for each combination of occupied/vacant bands, the components of the dipole moment matrix $\langle c_k|P^\alpha|v_k\rangle$.
- The calculation of the components of $\varepsilon_2(\omega)$ and the integration over the Brillouin zone are performed by the "**joint**" routine for a transition energy ranging from 0 to 14 eV. It is possible to choose the bands for which transitions are calculated. After determining the orbital character of each band, it is possible to separate the different components of the $\varepsilon_2(\omega)$ spectrum. This is valid only when the band characters are well-separated.
- The application of the Kramers-Kronig formula for the calculation of $\varepsilon_1(\omega)$ components is performed by the "**kram**" routine. At this stage, the value of the "scissors operator" Δc is given. This value is determined by the difference between the measured optical gap and the calculated optical gap. It is also possible to add a Lorentzian broadening, which accounts for experimental broadening with the Wien2k software. The different routines of the program are outlined, and on the right, the formula used.

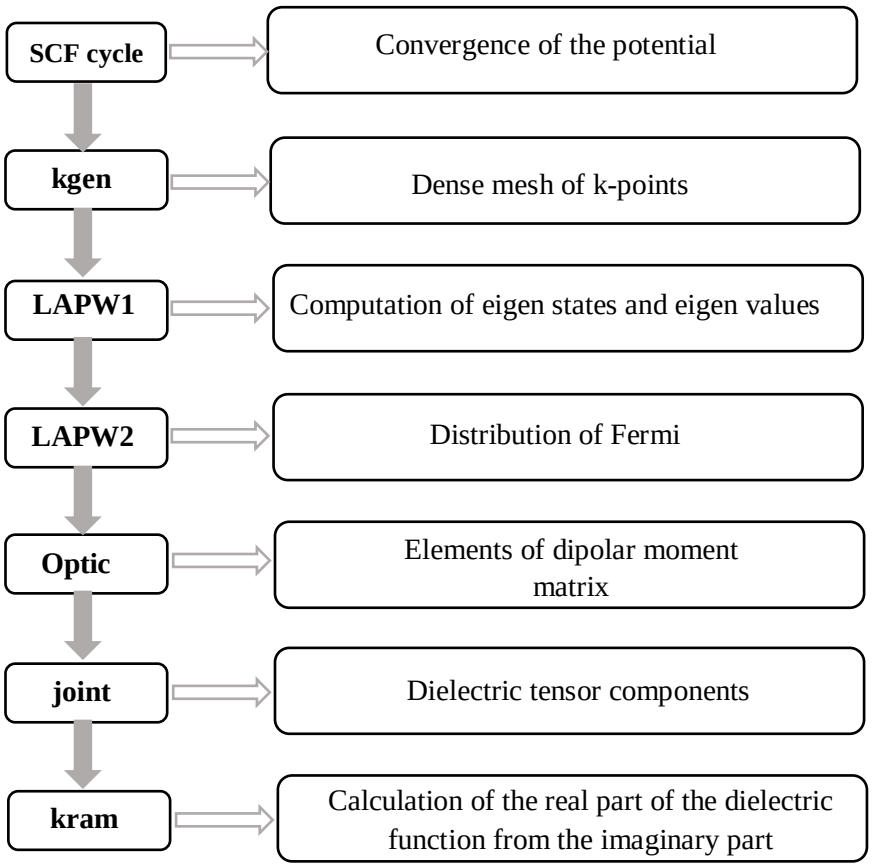

Figure. IV. 8: A diagram illustrating the various steps in the calculation of the complex dielectric constant.

IV.5.5. Results of optical properties computations

To evaluate the potential of K_2SnX_6 (X = Cl, Br, I) compounds as light-absorbing materials, we analysed several optical parameters, including dielectric function ($\varepsilon(\omega)$), refractive index ($n(\omega)$), light-absorption coefficients ($\alpha(\omega)$), extinction coefficient ($k(\omega)$), reflectivity coefficient ($R(\omega)$), and the energy associated with the loss function ($L(\omega)$), using the PBEsol-GGA functional with and without mBJ correction.

IV.5.5.1. Dielectric function

The optical properties of K_2SnCl_6, K_2SnBr_6, and K_2SnI_6 are primarily determined by the complex dielectric function $\varepsilon(\omega) = \varepsilon_1(\omega) + i\varepsilon_2(\omega)$, which characterizes the material's linear response to electromagnetic radiation. The imaginary part $\varepsilon_2(\omega)$ of the dielectric function represents optical absorption in the crystal. The imaginary part of $\varepsilon(\omega)$ is calculated by summing

the transitions from occupied to unoccupied states across the Brillouin zone. The real part $\varepsilon_1(\omega)$ of the dielectric function can be extracted from the imaginary part $\varepsilon_2(\omega)$ using the Kramers-Kronig relations.

The monoclinic symmetry of the reported crystal structures consent to four non-zero components of second order dielectric tensor: ε_{xx} (ω),ε_{yy} (ω),ε_{zz} (ω),ε_{xy} (ω). However, the ε_{xy} (ω) component is very small, therefore, we will not include it in this dissertation.

In order to identify all possible optical transitions, we used a dense mesh of 10000 k-points in the Brillouin zone, as the calculation of these properties requires a large number of eigenvalues corresponding to eigenvectors.

Using the optimized lattice parameters, the calculations were performed using the Generalized Gradient Approximation (GGA) and its modified Becke-Johnson potential correction in an energy range from 0 to 14 eV.

The imaginary part of the dielectric function

The **Figures. IV. 9-a** and **Figures. IV. 9-b** depict the imaginary part of the dielectric function for the indicated materials in the directions x- crystallographic, y- crystallographic and z- crystallographic, denoted $\varepsilon_{2xx}, \varepsilon_{2yy}$ and ε_{2zz}. In **Figures. IV. 9-a,** results are computed using GGA functional, and in **Figures. IV. 9-b** results are computed using mBJ-GGA.

We notice that dielectric functions in x-crystallographic, y-crystallographic and z-crystallographic directions are almost identical, excepting at the peaks where we notice slight differences between $\varepsilon_{2xx}, \varepsilon_{2yy},$ and ε_{2zz}. Hence we can deduce that the investigating compounds K_2SnX_6 (X= Cl, Br, I) show a considerable isotropy.

Moving from K_2SnCl_6 to K_2SnBr_6 to K_2SnI_6, the plots exhibit essentially indistinguishable trends, with a shift towards lower energy levels. The curves goes through several peaks and the maxima increase and reach a limit value before decreasing.

From these curves that reflects the material's absorption, we can extract information about the various interband transitions. The graphs represented in **Figures. IV. 9-b** (mBJ-GGA) exhibit their peaks values for K_2SnCl_6 at energy levels of 5.05, 7.09 eV, 9.12 eV, 11.03 eV, 13.13 eV. For K_2SnBr_6 the different peaks are at 3.6 eV, 5.9 eV, 7.5 eV, 9.6 eV, 11.7 eV, while for K_2SnI_6 the peaks are located at energy levels of 2.4 eV, 4.6 eV, 5.8 eV, 7.9 eV, 9.8 eV.

Moreover, it was subsequently shown in **Figures. IV. 9-a** and in **Figures. IV. 9-b** that the dielectric constants of K_2SnX_6 (X = Cl, Br, I) exhibit an increase when the ionic radius of the halogen anion increases.

The intensity of K_2SnI_6 in the $\varepsilon_2(\omega)$ spectra is observed to be higher compared to the other elements within the visible range, suggesting a notable level of absorptive activity in K_2SnI_6.

The real part of the dielectric function

Employing the Kramers- Kronig transformation [13], the real component of the dielectric function $\varepsilon_1(\omega)$ is derived from its imaginary component $\varepsilon_2(\omega)$. The real component $\varepsilon_1(\omega)$ is a measure of the degree of light polarization observed as light passes through a material.

The **Figures. IV. 9-c** depicts the real part of the dielectric function in the directions x-crystallographic, y- crystallographic and z- crystallographic, denoted $\varepsilon_{1xx}, \varepsilon_{1yy}$ and ε_{1zz} for the studied materials. The computations presented in this figure use GGA functional.

Figures. IV. 9-d shows the real part of the dielectric function for the studied materials in the directions x- crystallographic and z- crystallographic, denoted $\varepsilon_{1xx}, \varepsilon_{1yy}$ and ε_{1zz}. The computations presented in this figure adopt mBJ-GGA functional.

Whether in **Figure. IV. 9-c** or in **Figure. IV. 9-d**, the curves $\varepsilon_1(\omega)$ of all compounds show that $\varepsilon_{1xx}(\omega)$, ε_{1yy} and $\varepsilon_{1zz}(\omega)$ are almost identical for each compound. That fact shows a high level of isotropy.

The curves of the studied compounds in **Figure. IV. 9-c** and **-d** demonstrate the same trend with some differences, especially, in the position and height of the peaks. In fact**,** both figures show that starting from the values of $\varepsilon_1(0)$, the real part of the dielectric function increases with the increase in photon energy, and reach the major peak before decreasing. We note that, when decreasing, $\varepsilon_1(\omega)$ passes through zero to become negative for higher energies.

Considering mBJ-GGA computations, $\varepsilon_1(\omega)$ becomes null for K_2SnCl_6, K_2SnBr_6, and K_2SnI_6, at approximately 12.78 eV, 11.63 eV, and 8.80 eV, respectively.

Moreover, when the ionic radius of the halogen anion increases in K_2SnX_6 (X = Cl, Br, I) compounds, the curves shift towards lower energy levels.

For K_2SnCl_6, K_2SnBr_6, and K_2SnI_6, the static dielectric constants at the zero frequency limit are summarised in the **Table. IV. 8**. K_2SnI_6 exhibits a higher $\varepsilon_1(0)$ than the other compounds under study. This fact is explained by the Penn model:

$$\varepsilon_1(0) = 1 + \left(\frac{\hbar\omega p}{E_g}\right)^2 \qquad \text{(IV-22)}$$

In other words, a small energy gap results in a large value of $\varepsilon_1(0)$. In the case of our study, the bandgap of K_2SnI_6 is smaller than that of the compound K_2SnCl_6, K_2SnBr_6

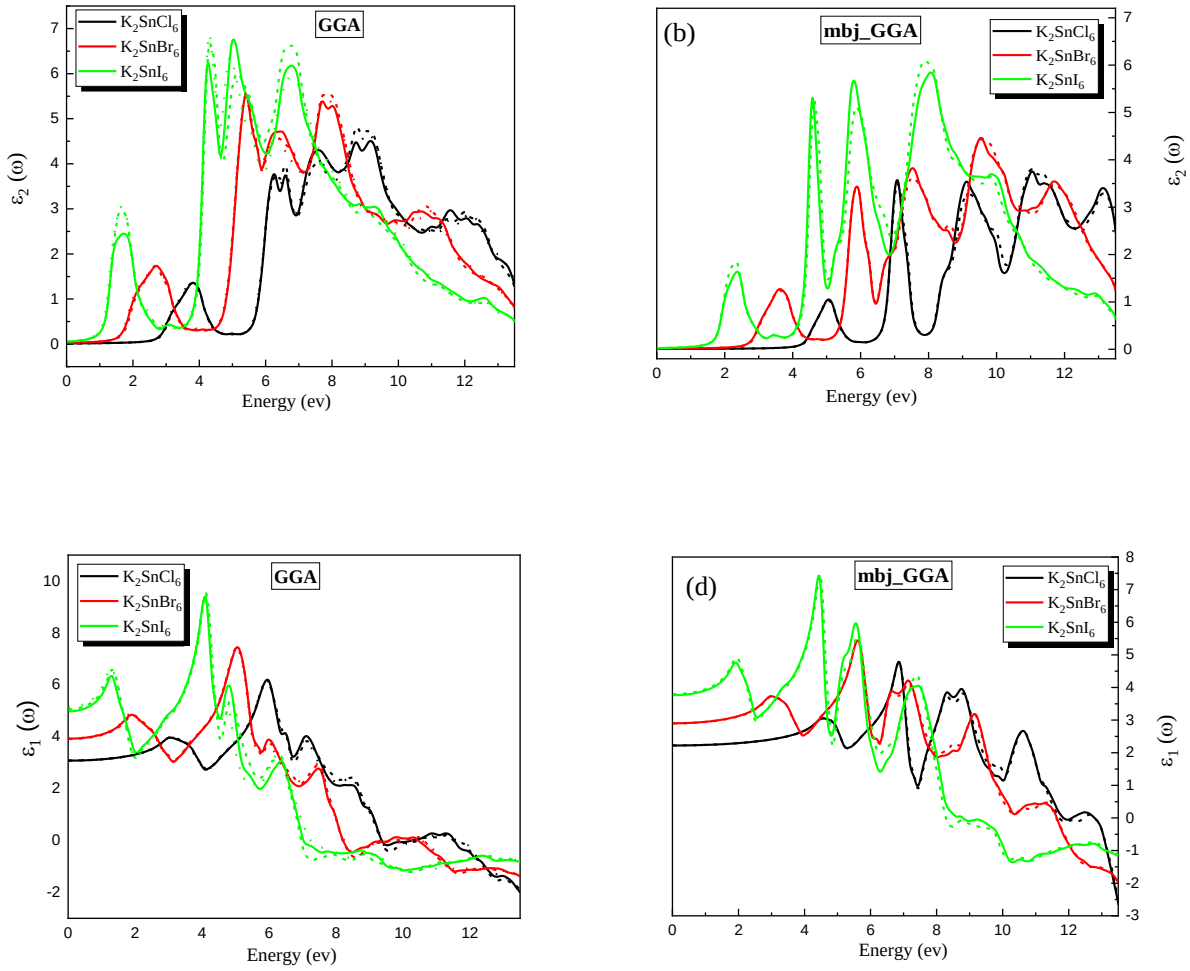

Figure. IV. 9: Calculated components of the dielectric function of the monoclinic phase of K_2SnCl_6, K_2SnBr_6, K_2SnI_6 computed by GGA and mBJ-GGA approximations, in x-crystallographic (solid line), y- crystallographic (dot lines)and z- crystallographic (dashed lines)

IV.5.5.2. Absorption coefficient

An important information for the application prospects can be found in the absorption coefficient ($\alpha(\omega)$). It represents the fraction of incident light absorbed per unit distance travelled through the material. It reflects the probability of a photon being absorbed as it passes through the material. The changes in the absorption coefficient in x-crystallographic, and z-crystallographic directions in terms of energy $\alpha_{xx}(\omega)$, and $\alpha_{zz}(\omega)$, are shown in **Figure. IV. 10-**

a and **Figure. IV. 10-b**. The computations in **a** and **b** were carried out using GGA and mBJ-GGA, respectively.

$\alpha_{xx}(\omega)$, and $\alpha_{zz}(\omega)$ are almost identical showing considerable isotropy of the compounds under study.

According to the figures, the absorption coefficient $\alpha(\omega)$ is larger than ($10^{4} cm^{-1}$) and increases rapidly. The absorption spectra indicates maxima throughout the energy interval from 0 to 14 ev

The energy band gap represents the threshold at which absorption initiates in a given material, as a result of the electronic transition from the valence band maximum (VBM) to the conduction band minimum (CBM). The optical gaps for K_2SnCl_6, K_2SnBr_6, and K_2SnI_6 were determined to be 4 eV, 2.3 eV, and 1 eV, respectively using mBJ-GGA potential. The optical bandgaps obtained from the calculations align with the theoretical bandgaps derived from the band structure analysis. Hence, validating the accuracy of the computational methodology employed in this study.

Due to their narrower band gaps, K_2SnI_6 and K_2SnBr_6 demonstrate superior light absorption in the visible light range than K_2SnCl_6, leading one to conclude that K_2SnBr_6 and K_2SnI_6 are more suitable as light-absorbing materials for solar cells. Whereas, K_2SnCl_6 can also be investigated as a promising semiconductor material for tandem photovoltaic applications and other optoelectronic devices because it exhibits good light absorption under the condition of photon energy larger than 3 eV.

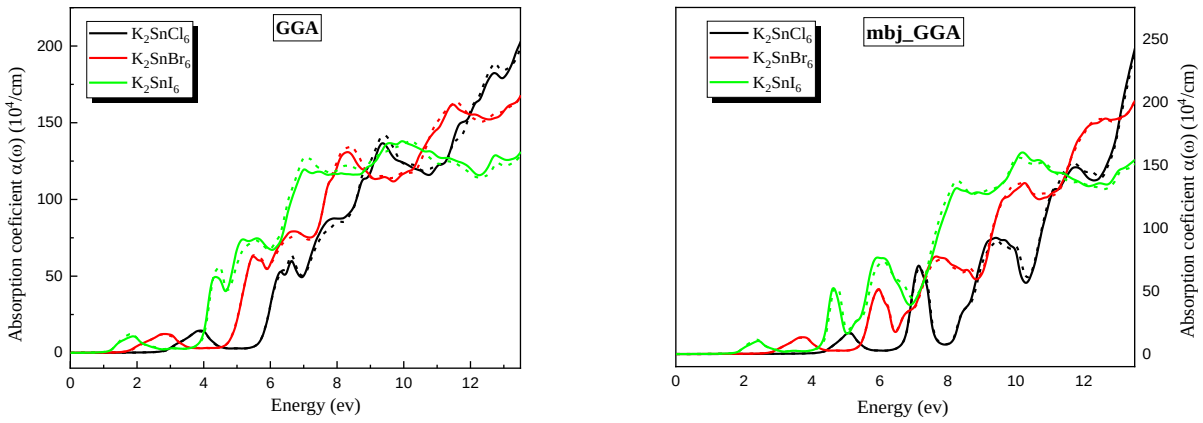

Figure. IV. 10: Calculated absorption coefficient of the monoclinic phase of K_2SnCl_6, K_2SnBr_6, K_2SnI_6 computed by GGA and mBJ-GGA approximations, in x- crystallographic (solid line) and z- crystallographic (dashed lines).

IV.5.5.3. Refractive index

Figure.IV. 12-a (**Figure.IV. 12-b**) shows the refractive index in terms of photon energy (ω) computed using GGA (mBJGGA) functional, in x-crystallographic $\left(n_{xx}(\omega)\right)$, and in z-crystallographic $\left(n_{zz}(\omega)\right)$. The calculated results show that the refractive index $n(\omega)$ is practically isotropic.

The curves depicted in Figure IV.12-a and -b follow a similar pattern with slight variations, particularly in the positioning and intensity of the peaks. Both figures illustrate that, starting from the initial values of $n(0)$, the refractive index increases with the rise in photon energy, reaching prominent peaks before undergoing a decrease.

Furthermore, an interesting observation is that as the ionic radius of the halogen anion increases in K_2SnX_6 compounds (X = Cl, Br, I), $n(\omega)$ experiences an augmentation, and a shift towards lower energy levels.

The calculated static refractive index $n(0)$ is summarized in the same table along with $\varepsilon_1(0)$. Note in **Table. IV. 8** as, an example, that K_2SnI_6, with its smaller energy gap compared to K_2SnBr_6 and K_2SnCl_6, has the highest values for both the static dielectric constant and the static refractive index.

In the mBJ-GGA curve, the first peak for K_2SnBr_6 is located at 3 eV, whereas for K_2SnI_6 it is set at 1.9 eV. These energy levels make them well-suited for solar applications. K_2SnCl_6 has a relatively low refractive index within the visible light spectrum.

Table. IV. 8: $\varepsilon_1(0)$ and $n(0)$ of K_2SnX_6 (X=Cl, Br, I) copmputed using GGA, and mBJ-GGA functionals

Compound	$\boldsymbol{\varepsilon_1(0)}$			$\boldsymbol{n(0)}$		
		GGA	mBJ-GGA		GGA	mBJ-GGA
K_2SnCl_6	ε_{1xx}	3.08	2.22	n_{xx}	1.75	1.49
	ε_{1zz}	3.08	2.22	n_{zz}	1.75	1.49
K_2SnBr_6	ε_{1xx}	3.91	2.90	n_{xx}	1.98	1.70
	ε_{1zz}	3.91	2.90	n_{zz}	1.98	1.70
K_2SnI_6	ε_{1xx}	4.97	3.76	n_{xx}	2.23	1.95
	ε_{1zz}	5.06	3.80	n_{zz}	2.25	1.94

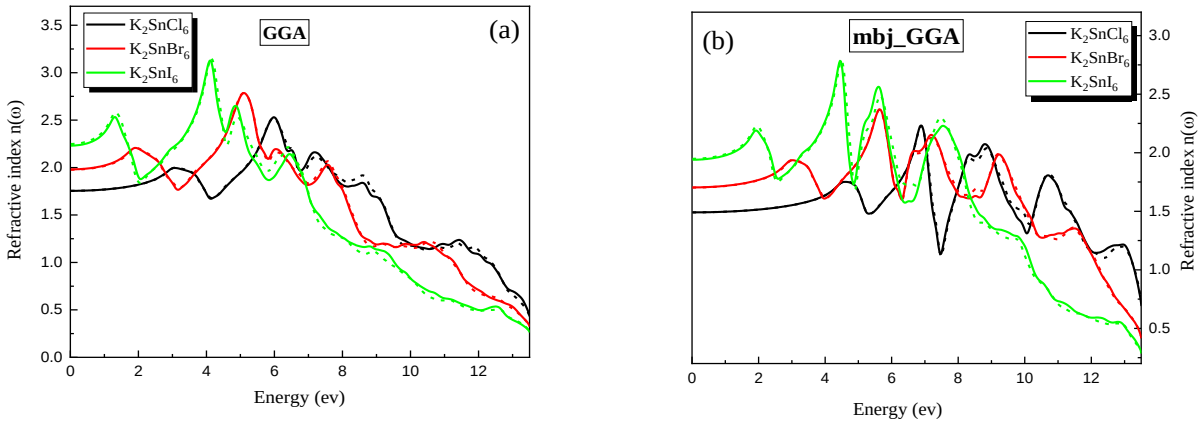

Figure. IV. 11: Calculated refractive index of the monoclinic phase of K_2SnCl_6, K_2SnBr_6, K_2SnI_6 computed by GGA and mBJ-GGA approximations, in x- crystallographic (solid line) and z- crystallographic (dashed lines)

IV.5.5.4. Extinction coefficient

The evolution of the extinction coefficient as a function of the energy for the studied compounds is shown in **Figure. IV. 12-a** (computed using GGA) and in **Figure. IV. 12-b** (computed using mBJ-GGA). The x-crystallographic ($k_{xx}(\omega)$), and z-crystallographic $k_{zz}(\omega)$ coefficients are almost identical except in the maxima where we notice slight differences. It is evident from the data presented in **Figure. IV. 12-a** and **Figure. IV. 12-b** that the variation in the extinction coefficient $k(\omega)$ follows a similar pattern to that of the absorption coefficient ($\alpha(\omega)$). The spectra are similar with small differences in the details.

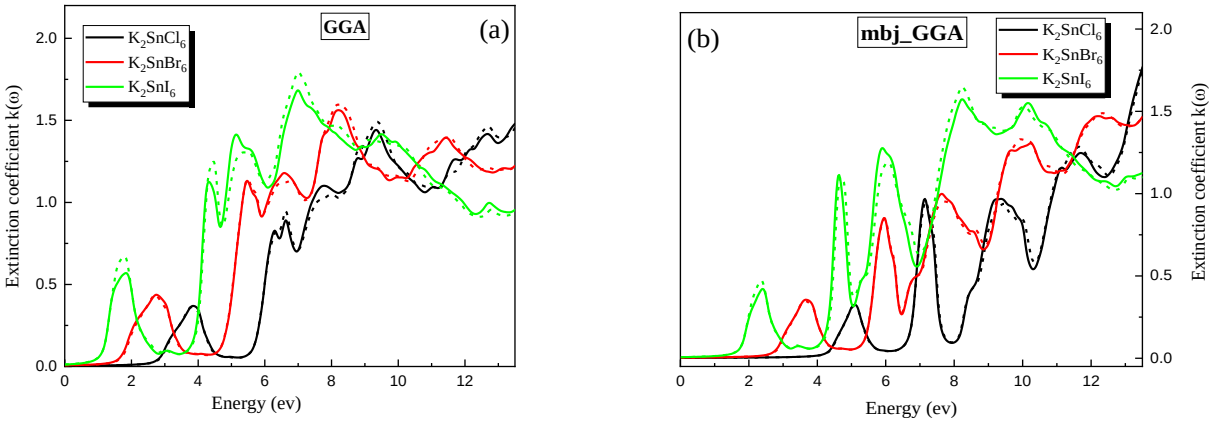

Figure. IV. 12: Calculated extinction coefficient of the monoclinic phase of K_2SnCl_6, K_2SnBr_6, K_2SnI_6 computed by GGA and mBJ-GGA approximations, in x- crystallographic (solid line) and z- crystallographic (dashed lines).

IV.5.5.5. Reflectivity

The reflectivity ($R(\omega)$) is a fundamental optical parameter that quantifies the amount of light reflected from a given surface. **Figure. IV. 13-a** and **Figure. IV. 13-b** display the reflectivity spectra of K_2SnCl_6, K_2SnBr_6, and K_2SnI_6 computed using GGA and mBJ-GGA respectively. The reflectivity in x-crystallographic $R_{xx}(\omega)$, and in z-crystallographic $R_{zz}(\omega)$ are depicted. $R_{xx}(\omega)$, and $R_{zz}(\omega)$ are almost identical showing a high level of isotropy.

It is observed that at low energies, these compounds have a low reflectivity. According to **Figure. IV. 13-a**, It starts at 5% for K_2SnCl_6, approximately 10% for K_2SnBr_6, and about 15% for K_2SnBr_6. Then, a rapid increase in reflection occurs at intermediate and high energies. These reflectivity maxima result from interband transitions.

It is noteworthy that, in the visible spectrum, the reflectivity of the investigated compounds is below 15% .

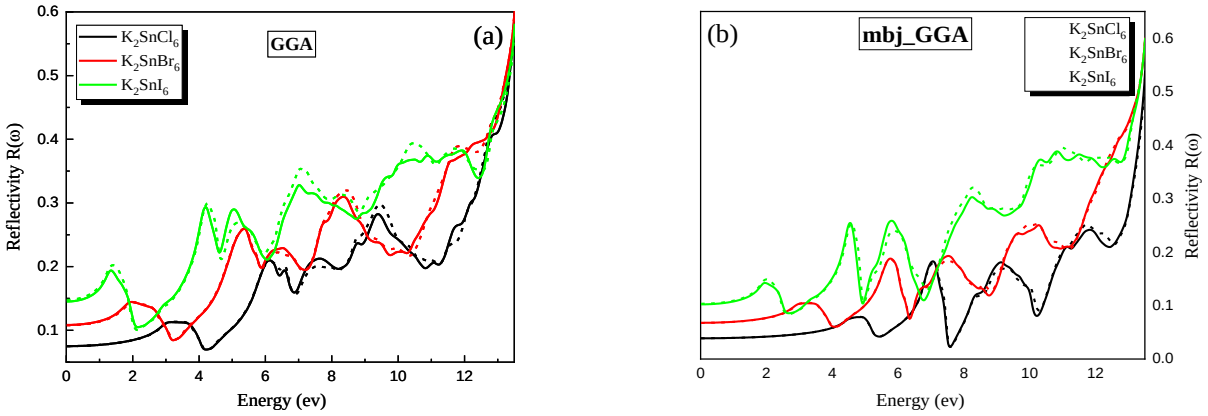

Figure. IV. 13: Calculated reflectivity of the monoclinic phase of K_2SnCl_6, K_2SnBr_6, K_2SnI_6 computed by GGA and mBJ-GGA approximations, in x- crystallographic (solid line) and z-crystallographic (dashed lines)

IV.5.5.6. Energy loss function

The energy-loss function ($L(\omega)$) characterizes the probability of light attenuation as it passes through a material. In the other hand, the energy loss function helps to identify electronic transitions between the energetic states of a material. In fact, peaks in the energy loss function correspond to energies where specific electronic transitions occur.

The energy loss function can be evaluated from the dielectric function. It can be described by the expression:

$$L(\omega) = Im\left(\frac{-1}{\varepsilon(\omega)}\right) \quad \text{(IV-23)}$$

Which can be written as :

$$L(\omega) = Im\left(\frac{\varepsilon_2(\omega)}{\varepsilon_1(\omega)^2+\varepsilon_2(\omega)^2}\right) \quad \text{(IV-24)}$$

Figure. IV. 14 presents the energy loss spectrum ($L(\omega)$). The extinction coefficient and energy-loss function curves clearly exhibit similar patterns.

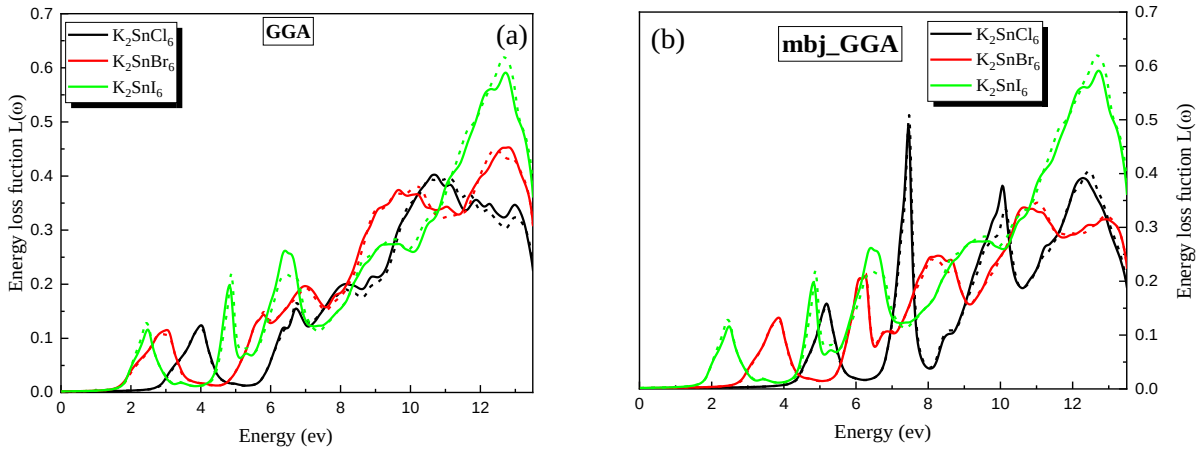

Figure. IV. 14: Calculated energy loss function of the monoclinic phase of K_2SnCl_6, K_2SnBr_6, K_2SnI_6 computed by GGA and mBJ-GGA approximations, in x- crystallographic (solid line) and z- crystallographic (dashed lines).

IV.5.5.7. Optical conductivity

The optical conductivity, which is a complex quantity, can be given by the following expression:

$$\sigma(\omega) = -\frac{i\omega}{4\pi}\,\varepsilon(\omega) \qquad \text{(IV-25)}$$

The optical conductivity $\sigma(\omega)$ includes various elements that explain the relationship between the oscillating electric field $\vec{E}$ and the current density $\vec{J}$. **Figure. IV. 15** illustrates the optical conductivity spectrum, which shows multiple peaks, each representing transitions between different bands.

The results computed using mBJ-GGA represented in **Figure. IV. 15-b** shows that the optical conductivity for our compounds begins around the values corresponding to the material's gap (4.17 eV, 2.73 eV, 1.65 eV for K_2SnCl_6, K_2SnBr_6 , K_2SnI_6, respectively). After these points, it increases and reaches its maximum value, then decreases. $\sigma(\omega)$ goes through several peaks. Its maximum value is 6018.61 $\Omega^{-1}.cm^{-1}$ at 13.13 eV for K_2SnCl_6, 5736.64 $\Omega^{-1}.cm^{-1}$ at 9.59 eV for K_2SnBr_6, and 6352.39 $\Omega^{-1}.cm^{-1}$ at 8.1 eV for K_2SnI_6 . The secondary peaks correspond to different transitions between the conduction band and the valence band. Moreover, the

variation in halogen in K_2SnX_6 from Cl to Br to I shifts the maximum values of conductivity to lower energies.

In **Figure. IV. 15-a**, the results computed using GGA are depicted. The curves show the same trend than those of **Figure. IV. 15-b** with a shift toward lower energies.

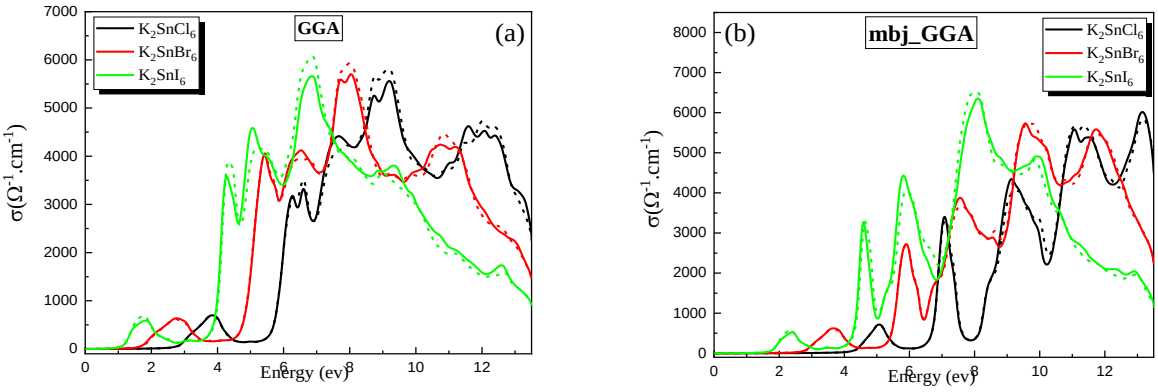

Figure. IV. 15: Calculated optical conductivity of the monoclinic phase of K_2SnCl_6, K_2SnBr_6, K_2SnI_6 computed by GGA and mBJ-GGA approximations, in x- crystallographic (solid line) and z- crystallographic (dashed lines)

IV.6. Thermoelectric properties

IV.6.1. Introduction

The evaluation of thermoelectric devices performance is conducted through the principal parameter called "the figure of merit" introduced by Altenkirch in 1911 **[16,17]**,

$$ZT = \frac{\sigma T S^2}{\kappa} \qquad \text{(IV-26)}$$

Where, the parameters are Seebeck coefficient (S), electrical conductivity (σ), total thermal conductivity (κ), and absolute kelvin temperature (T). Therefore, large S and σ with a small κ are characteristics of a good thermoelectric device. These parameters are also called "transport coefficients. The calculation of the figure of merit (ZT) involves the total thermal conductivity

$\kappa = \kappa_e + \kappa_L$, which is the sum of the electronic thermal conductivity (κ_e) and the lattice thermal conductivity (κ_L).

The intention of this study is to calculate the cited thermoelectric parameters of materials with ab initio methods.

The methodology for this study is divided into two main steps:

1) Performing a density functional theory (DFT) calculation (a detailed explanation of DFT is provided in Chapter III) to determine both the minimum energy structure and the ground-state electronic structure.
2) The application of the **Boltzmann transport theory [18-20]** implemented in BoltzTraP code **[5,21]**, using data from a density functional theory calculation to determine the thermoelectric properties.

Before presenting any results concerning the thermoelectric properties of studied compounds, we will, first, expose the transport coefficients derivation from Boltzmann transport theory, as well as the Slack equation used to determine the lattice thermal conductivity near the Debye temperature. Then, we will also give a simple overview of The BoltzTrap code.

IV.6.1.1. Transport coefficients derivation

In order to study thermoelectricity, it is crucial to be able to calculate the transport properties of a system. At the macroscopic level, the disturbance caused by an electric field or temperature gradient prompts the generation of electrical or thermal currents within the material. The local associations between the electric field $\vec{E}$ and the temperature gradient $\vec{\nabla}T$ along with their respective electrical current $\vec{J}$ and heat current $\vec{J}_Q$, for an isotropic solid, are as follows:

$$\vec{J} = \sigma.\vec{E} - S\sigma.\vec{\nabla}T \quad \text{(IV-27)}$$

$$\vec{J}_Q = S\sigma T.\vec{E} - \kappa_0.\vec{\nabla}T \quad \text{(IV-28)}$$

where σ is the electrical conductivity, S the Seebeck coefficient. The electronic component of thermal conductivity, denoted as κ_e, is defined as the heat current generated per unit temperature gradient in the absence of an electrical current:

$$\kappa_e = \kappa_0 - T\sigma S^2 \quad \text{(IV-29)}$$

The total thermal conductivity of the material results from combining this electronic contribution with the corresponding contribution from the lattice. In real materials, the currents may not align

perfectly with the electric field or thermal gradient, and the transport coefficients are tensor quantities. This adds complexity to the relations mentioned above, but the fundamental definitions remain unchanged.

To assess the transport coefficients, we require a microscopic model of the transport phenomenon. We adopt the semi-classical approach provided by solving Boltzmann's equation within the relaxation time approximation. For a detailed explanation of the method, refer to the book by Nag. **[37]**. Here, we provide a concise overview. Typically, the electrical current of carriers (electrons or holes) is characterized as follows.

$$\vec{J} = e \sum_{\vec{k}} f_{\vec{k}} \vec{v}_{\vec{k}} \tag{IV-30}$$

where e is the elementary charge. The summation encompasses all quantum numbers of the system, which, in the scenario of a crystalline solid, correspond to the three components of the crystal momentum $\vec{k}$. $f_{\vec{k}}$ represents the population of the quantum state labeled with $\vec{k}$, while $\vec{v}_{\vec{k}}$ signifies the group velocity linked to that state. This velocity is defined as the gradient in reciprocal space of the dispersion relation (band structure) of the electrons within the crystal.

$$\vec{v}_{\vec{k}} = \frac{1}{\hbar} \frac{\partial \varepsilon_{\vec{k}}}{\partial \vec{k}} \tag{IV-31}$$

There is here a need for an analytical expression of the distribution function, which is the solution of the Boltzmann equation:

: $$\frac{\partial f_{\vec{k}}}{\partial t} = -\vec{v}_{\vec{k}} . \frac{\partial f_{\vec{k}}}{\partial \vec{r}} - \frac{e}{\hbar} \left(\vec{E} + \frac{1}{c} \vec{v}_{\vec{k}} \times \vec{H} \right) . \frac{\partial f_{\vec{k}}}{\partial \vec{k}} + \left(\frac{df_{\vec{k}}}{dt} \right)_{scattering} \tag{IV-32}$$

This statement suggests that the rate of change of the population depends on diffusion, the influence of electric field $\vec{E}$ or magnetic fields $\vec{H}$, or scattering. When fields are absent, the stationary solution of Boltzmann's equation for fermions yields the Fermi distribution function $f_0(\varepsilon_{\vec{k}})$. This distribution ensures that the population remains the same for $\vec{k}$ and -$\vec{k}$, resulting in a cancellation in the summation in Equation (IV-30), and thus, zero net current flow.

By linearizing the equation and employing the relaxation time approximation for the scattering term, and assuming the absence of magnetic fields and temperature gradients, the population can be expressed by:

$$f_{\vec{k}} = f_0(\varepsilon_{\vec{k}}) + e\left(\frac{\partial f_0}{\partial \varepsilon}\right)\tau_{\vec{k}}\vec{v}_{\vec{k}}.\vec{E} \quad \text{(IV-33)}$$

In this equation, τ represents the relaxation time, and the complete spatial variation of f is determined by the thermal gradient. Utilizing this expression to compute the current, we obtain the electrical conductivity tensor:

$$\sigma = e^2 \sum_{\vec{k}} \left(-\frac{\partial f_0}{\partial \varepsilon}\right) \vec{v}_{\vec{k}}\vec{v}_{\vec{k}}\tau_{\vec{k}} \quad \text{(IV-34)}$$

Equivalent formulas can be generated for both the Seebeck coefficient and electronic thermal conductivity. Nonetheless, for the sake of simplicity, we opt to delineate the transport distribution (TD).

$$\Xi = \sum_{\vec{k}} \vec{v}_{\vec{k}}\vec{v}_{\vec{k}}\tau_{\vec{k}} \quad \text{(IV-35)}$$

The transport coefficients in a unit cell crystal of volume **Ω** can then be calculated, for a specific chemical potential μ and temperature, by integrating this conductivity distribution:

$$\sigma = e^2 \int \Xi(\varepsilon)\left[-\frac{\partial f_0}{\partial \varepsilon}\right] d\varepsilon \quad \text{(IV-36)}$$

$$S = \frac{ek_B}{\sigma} \int \Xi(\varepsilon)\left(\frac{\varepsilon-\mu}{k_B T}\right)\left[-\frac{\partial f_0}{\partial \varepsilon}\right] d\varepsilon \quad \text{(IV-37)}$$

$$\kappa_0 = k_B^2 T \int \Xi(\varepsilon)\left(\frac{\varepsilon-\mu}{k_B T}\right)^2\left[-\frac{\partial f_0}{\partial \varepsilon}\right] d\varepsilon \quad \text{(IV-38)}$$

Here, μ represents the chemical potential, and k_B denotes Boltzmann's constant. Equations (IV-36) to (IV-38) illustrate that the transport distribution encompasses all material-specific details pertinent to transport properties.

IV.6.1.2. Lattice thermal conductivity near the Debye temperature

Near the Debye temperature, interactions among phonons themselves, via anharmonic Umklapp processes, are significant. Several initial approximations of the lattice thermal conductivity within this regime have been deliberated by Slack **[23]** and Berman **[36]**. These approximations can be viewed as rough representations for the thermal conductivity at temperatures relatively close to the Debye temperature of the solid. They all follow a similar structure:

. $$\kappa_L = A \cdot \frac{M_a \theta_a^3 \delta}{\gamma^2 T} \quad \text{(IV-39)}$$

where M_a is the atomic mass of the atom, δ^3 is the volume per atom, and A is a constant. Leibfried and Schlömann **[35]** give the constant as A = 5.72×10^{-8} for δ in *Angstroms* and M_a in

atomic mass units. Julian **[22]** pointed out an error in their calculation and determined the following value for A:

$$A = \frac{2.43 \cdot 10^{-8}}{1 - 0.514/\gamma + 0.228/\gamma^2} \quad \text{(IV-40)}$$

Slack **[23]** put $\gamma \approx 2$ in this expression and used $A = 3.04 \times 10^{-8}$. The γ-dependence of A is slight and we will allow this parameter to assume its value appropriate to the value of γ used to calculate the thermal conductivity.

The lattice thermal conductivity κ_L computation, using the Slack equation, is implemented in the Gibbs code **[24,25]**.

Equation (IV-39) is applicable to structures with a single atom in the primitive unit cell. By employing a straightforward counting approach, Slack **[23]** expanded the model to encompass crystals with *n* atoms per unit cell:

$$\kappa = A \cdot \frac{M_a \theta_a^3 \delta}{\gamma^2 T n^{2/3}} \quad \text{(IV-41)}$$

IV.6.1.3. BoltzTrap code: a BTE based computational software

It contains the program Boltzmann Transport Properties for calculating the semi-classic transport coefficients.

The BoltzTrap code **[5,21]** simplifies the computation of these transport coefficients with minimal computational resources. This code employs Fourier expansions to solve the Boltzmann equation within the relaxation time approximation. Utilizing the interpolated band structure, it calculates the necessary derivatives for evaluating transport properties such as group velocities. Therefore, it is crucial to ensure accurate band energy computations through Wien2k before employing BoltzTrap. The BoltzTrap code operates under the Rigid Band Approximation (RBA) **[38,39]** and the Constant Scattering Time Approximation (CSTA), and these approximations have been successfully applied for several thermoelectric materials **[40-42]**. For ease of computing transport coefficients, BoltzTrap considers the relaxation time as constant (i.e. temperature and energy-independent) and the average value is taken as 10^{14}s. However, it also offers the option to introduce energy and temperature-dependent relaxation times corresponding to specific electron scattering processes, enabling the computation of their respective transport properties.

IV.6.2. Electrical conductivity

The electrical conductivity (σ) changes with temperature are depicted in **Figure. IV. 16**. The behavior of σ as a function of T shows the increasing trends from 0.44/0.28/0.52 ($10^4.\omega^{-1}.m^{-1}$)

at 50 K to 7.64/6.78/4.36 ($10^5.\omega^{-1}.m^{-1}$) at 500 K for K_2SnCl_6, K_2SnBr_6, and K_2SnI_6, respectively. This evidences the semiconductor nature of K_2SnX_6 vacancy-ordered double perovskites. The following relationship links σ with carrier concentration *n*:

$$\sigma = ne\mu \qquad \text{(IV-42)}$$

Where: *n* is the electrons concentration, μ: is the mobility and *e* is the electrical charge. The rise in carrier concentration when the temperature increases is the cause of the positive temperature dependence of σ.

It is also notable that for temperatures larger than 200 K, the values of electrical conductivity of K_2SnI_6 are considerably less than those of K_2SnCl_6 and K_2SnBr_6, while for temperatures lower than 200 K, the reverse trend is observed. This fact can be explained by the high level of scattering which occurs in the three compounds, however, the scattering properties are influenced by the size and mass of the halide ions (Cl^-, Br^-, I^-) surrounding the tin (Sn) ions. Generally, the likelihood of scattering increases with the mass and size of the ions because larger and heavier ions can cause more significant disruptions to the movement of charge carriers. Considering the trends in ion size and mass, K_2SnI_6 is has the highest level of scattering among the three compounds and K_2SnCl_6 has the smallest one.

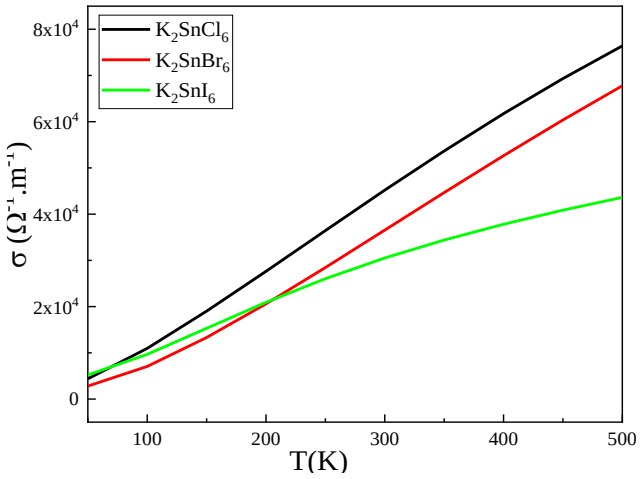

Figure. IV. 16: The computed electrical conductivity σ in terms of temperature, for K_2SnCl_6(X=Cl, Br, I) compounds.

IV.6.3. Thermal conductivity

The charge carrier's contribution to heat transfer is represented by κ_e. **Figure. IV. 17 (a)** displays the electronic thermal conductivity (κ_e) behavior against the temperature. For the three compounds, κ_e value augments as the temperature increases from 0.015/0.009/0.013 ($W.m^{-1}.K^{-1}$) at 50 K to 1.94/1.92/0.92 ($W.m^{-1}.K^{-1}$) at 500 K for K_2SnCl_6, K_2SnBr_6, and K_2SnI_6, respectively. This trend of electronic thermal conductivity is expected, since the electrons concentration increases with temperature.

On the other hand, electronic thermal conducticity decreases from K_2SnCl_6 to K_2SnBr_6, to K_2SnI_6. In fact, larger and heavier ions lead to increased scattering and lower carrier mobility, affecting the electronic thermal conductivity of the material.

Figure. IV. 17 (b) shows the lattice contribution to thermal conductivity (κ_L) as a function of temperature, determined using the Slack equation **[23]**. The values of κ_L decrease with increasing temperature. This behavior indicates a reduction in phonon heat transfer as the temperature rises., from 6.02/ 2.48/ 1.97 ($W.m^{-1}.K^{-}$) at 50 K to 0.60/0.25/0.197 ($W.m^{-1}.K^{-1}$) at 500 K for K_2SnCl_6, K_2SnBr_6, and K_2SnI_6, respectively. In fact, the phenomenon of decreasing lattice thermal conductivity with an increase in temperature is often attributed to increased phonon-phonon scattering at higher temperatures. As the temperature rises, thermal vibrations (phonons) become more pronounced, leading to increased collisions and scattering between phonons. This increased scattering reduces the mean free path of phonons, hindering their ability to transport heat through the material efficiently.

On the other hand, thermal conductivity decrease from K_2SnCl_6 to K_2SnBr_6 to K_2SnI_6 . In fact, lighter atoms transfer heat more effectively through vibrations in the lattice. As mass increases, the ability of atoms to vibrate decreases, leading to lower thermal conductivity.

Figure. IV. 17 (c) depicts the relationship between the temperature and the total heat transfer by charge carriers and phonons (κ). The thermal conductivity values decline until reaching 200 K for K_2SnCl_6, while they decrease until 250 K for K_2SnBr_6, and decrease until 350 K for K_2SnI_6. After these temperatures respectively, the total thermal conductivity (κ) shows a little increase with increasing temperature. This increase is a result of the fact that the number of charge carriers augments with temperature. Whereas, in the case of low tempertaures, the electronic thermal conductivity is low, such as the calculated value of κ_e accounts for less than 2 % of κ. Therefore, the electronic part is negligible and the lattice thermal conductivity is approximately equal to the total thermal conductivity, $\kappa \approx \kappa_L$.

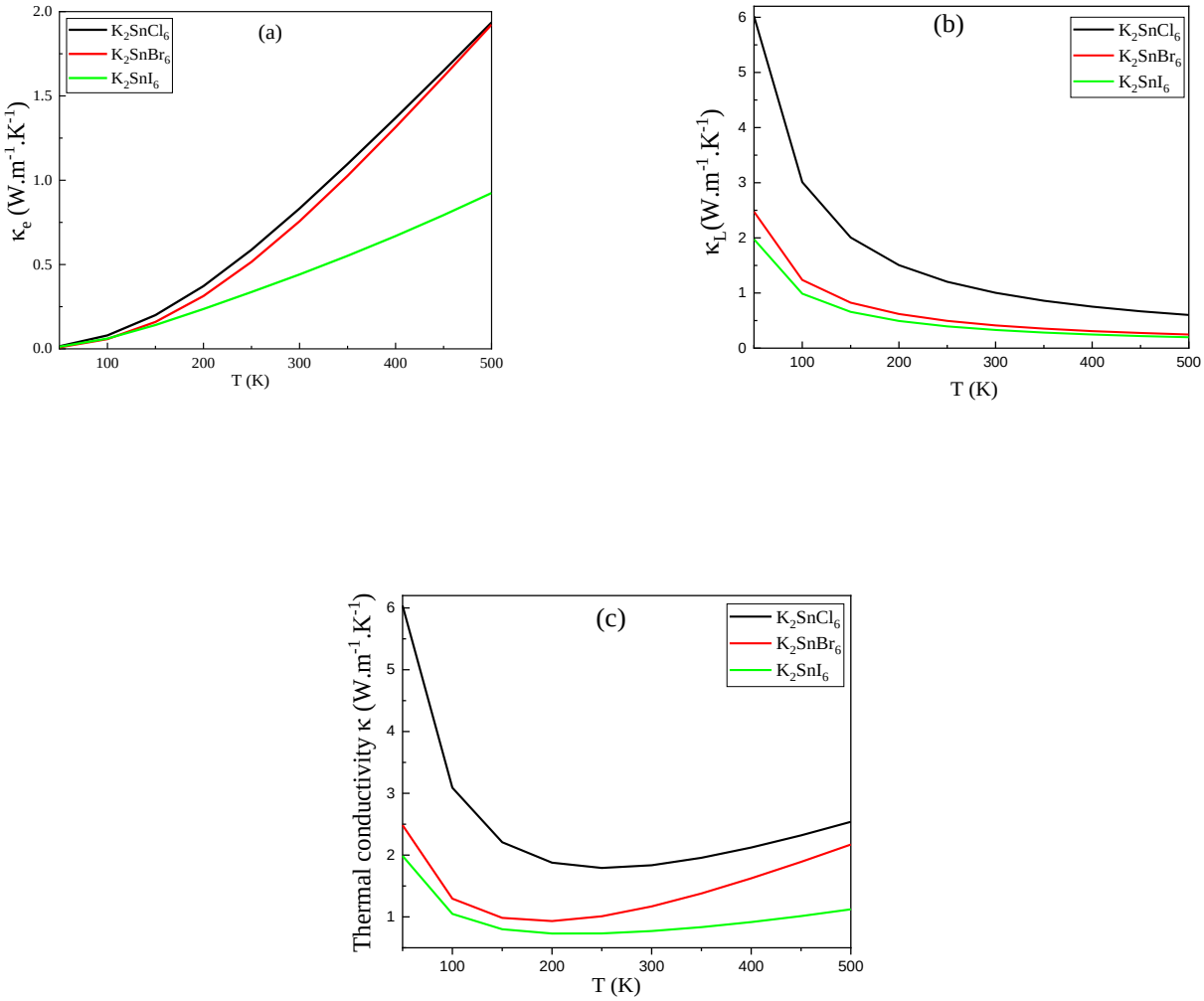

Figure. IV. 17: Representation of: (a) The electrons contribution to thermal conductivity (κ_e), (b) The lattice contribution to thermal conductivity (κ_L), and (c) The total thermal conductivity (κ) in terms of temperature for K_2SnCl_6, K_2SnBr_6, and K_2SnI_6.

IV.6.4. Seebeck coefficient

The Seebeck coefficient (S) quantifies the voltage generated by a material when exposed to a temperature gradient. **Figure. IV. 18** illustrates the Seebeck coefficient (S) for K_2SnX_6 (X = Cl, Br, I) compounds over the temperature range of 100-500 K. Throughout this range, the Seebeck coefficient (S) values for these compounds remain positive, indicating p-type conductivity. Furthermore, the Seebeck coefficient (S)decreases as the temperature rises from 150 K onwards, which is consistent with the behavior observed in other semiconductors **[26]**, **[27]**. Its values in this range of temperature varies from $2.33.10^{-4}$, $2.50.10^{-4}$, and $2.27.10^{-4}$ (V/K)

at 150 K to $1.97.10^{-4}$, $2.11.10^{-4}$, and $1.82.10^{-4}$ (V/K) at 500 K for K_2SnCl_6, K_2SnBr_6, and K_2SnI_6, respectively. We notice that Seebeck coefficient of our compounds is relatively high **[28,29]**.

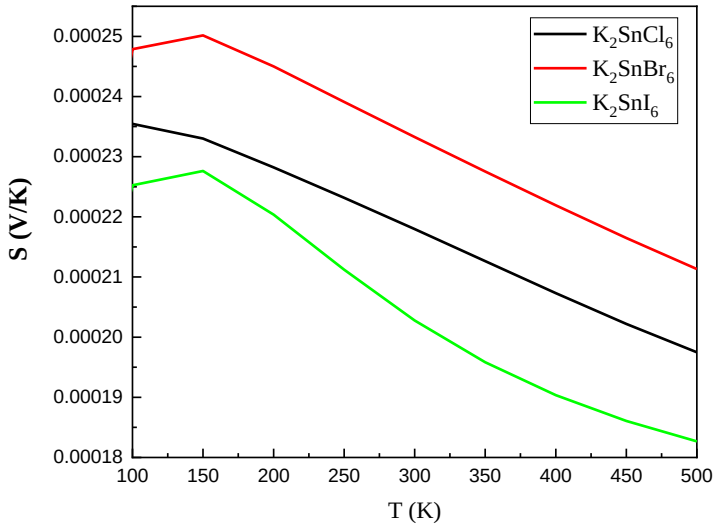

Figure. IV. 18: The computed Seebeck coefficient (S) as a function of temperature for K_2SnCl_6, K_2SnBr_6, and K_2SnI_6..

IV.6.5. Power factor coefficient

The thermoelectric strength is measured by the σ and S^2 whose combination is illustrated by σS^2 termed as power factor (PF = σS^2). **Figure. IV. 19** depicts how it changes with temperature for th compounds K_2SnX_6 (X= Cl, Br, or I). PF increases from ~2.04×10^{-4} W/mK^2 (at 50 K) to ~3×10^{-3} W/mK^2 (at 500 K) for K_2SnCl_6, from ~9.7×10^{-5} W/mK^2 (at 50 K) to ~3×10^{-3} W/mK^2 (at 500 K) for K_2SnBr_6, and from~1.7×10^{-4} W/mK^2 (at 50 K) to 1.5×10^{-3} W/mK^2 (at 500 K) for K_2SnI_6. The calculated PF values assure their overall potential as effective thermoelectric materials **[26-29]**.

At temperatures exceeding 150 K, the power factor values for K_2SnI_6 are significantly lower than those observed for K_2SnCl_6 and K_2SnBr_6. However, at temperatures below 150 K, the power factor values for all three compounds are comparable. It is notable that this trend is similar to the electrical conductivity versus temperature trend.

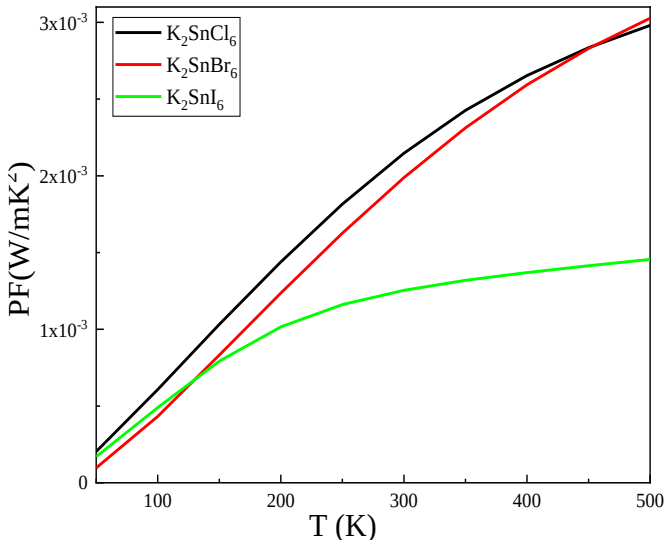

Figure. IV. 19: The computed Power Factor coefficient PF as a function of of temperature for K_2SnCl_6, K_2SnBr_6, and K_2SnI_6..

IV.6.6. Figure of merit

The calculations presented in **Figure. IV. 20** depict the Figure of merit (ZT) variation in terms of temperature for the compounds K_2SnX_6 (X=Cl, Br, I) in monoclinic phase. It is observed that, for all studied compounds, ZT increases reasonably until reaching a maximum. This trend is a result of the reduction of κ and the increase of power factor ,simultaneously, with increasing T.

At 500 K the maximum ZT values for, K_2SnCl_6, K_2SnBr_6, and K_2SnI_6 are 0.58, 0.69, and 0.65, respectively. These values are notably higher compared to those of metal and lead halide perovskites **[43]**. This indicates that the materials being studied are particularly effective for thermoelectric applications at elevated temperatures.It is also notable that K_2SnBr_6 exhibits the highest ZT value among the three compounds at high temperatures.

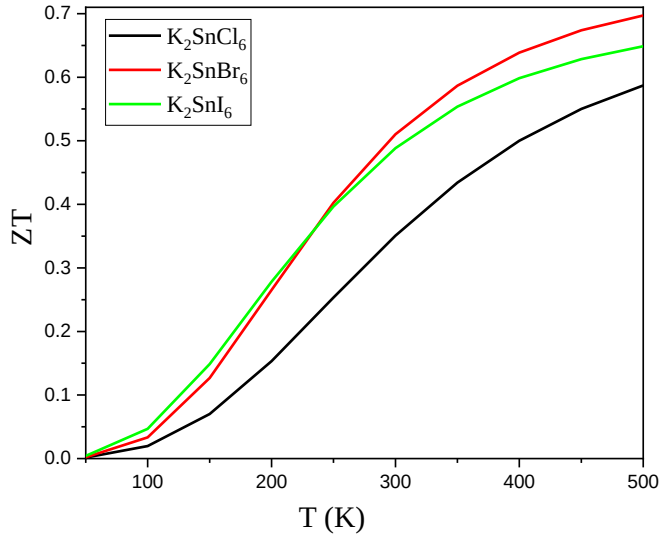

Figure. IV. 20: The computed Figure of merit ZT as a function of temperature, for K_2SnCl_6, K_2SnBr_6, and K_2SnI_6..

.

IV.6.7. Conclusion

The Seebeck coefficient (S) confirmed p-type conductivity for all compounds, and its positive values decreased with rising temperature, consistent with semiconductor behavior. The power factor (PF), a measure of thermoelectric strength, demonstrated an overall potential for effective thermoelectric materials, reaching significant values at elevated temperatures. However, K_2SnI_6 exhibited lower power factor values compared to K_2SnCl_6 and K_2SnBr_6 at temperatures exceeding 150 K.

The figure of merit (ZT), a crucial parameter for assessing thermoelectric efficiency, exhibited a reasonable increase with temperature for all compounds, reaching maximum values at 500 K. Notably, K_2SnBr_6 displayed the highest ZT value among the three compounds at high temperatures.

In summary, the investigated K_2SnX_6 compounds present promising thermoelectric properties, especially at elevated temperatures, making them potential candidates for thermoelectric applications. The systematic analysis of their electrical and thermal behaviors provides a foundation for further exploration and optimization of these materials for practical thermoelectric devices.

IV.7. Thermodynamic properties

The determination of thermodynamic properties has a dual role: firstly, it aids in enhancing our comprehension and forecasting of the characteristics of established or novel materials, including their chemical and thermal stability, mechanical properties, phases, and microstructures. Secondly, it supplies crucial information for refining the manufacturing processes of these materials and evaluating how they will perform in their intended surroundings. The calculations conducted in this work were executed using an approach rooted in the formalism of density functional theory.

The impact of pressure is addressed by a straightforward addition of a (pV) term to the energy equation, whereas the influence of temperature necessitates the utilization of a thermal model that incorporates the crystal's degrees of freedom into the free energy. To compute the thermodynamic properties of materials and consider the temperature-related effects overlooked by the Born-Oppenheimer approximation, we applied the quasi-harmonic Debye model , which is integrated into the Gibbs2 software **[30]**. This software was developed by Blanco and his collaborators **[25,31].** The calculation methodology employed in Gibbs2 is thoroughly detailed in reference **[25]**. The only data essential for conducting computations with this software are the outcomes derived from ab-initio calculations, specifically the energy as a function of volume $E(V)$.

IV.7.1. The quasi-harmonic Debye model

Utilizing the energy of a solid (E) as a function of molar volume (V), the Gibbs2 program employs the quasi-harmonic Debye model to calculate the Debye temperature (θ_D), and then derives the out-of-equilibrium Gibbs function $G^*(x, V;\ p, T)$. Minimizing G^* results in the determination of the thermal equation of state (EOS) $V(p, T)$, and the chemical potential $G(p, T)$ for the corresponding phase. Additionally, various other macroscopic properties are obtained as functions of p and T through classical thermodynamic relations.

The out-of-equilibrium Gibbs function $G^*(x, V, p, T)$. is given in the following form **[30,31]**:

$$G^*(x, V; p, T) = E_{sta}(x, V) + pV + F^*_{vib}(x, V; T) + F^*_{el}(x, V; T) + \cdots \qquad \text{(IV-43)}$$

Where:

- $E_{sta}(x, V)$ represents the static energy determined through ab initio calculations.

- pV corresponds to the hydrostatic condition.
- $F^*_{vib}(x,V;T)$ and $F^*_{el}(x,V;T)$ are the out-of-equilibrium vibrational and electronic free energies, respectively.

As per standard thermodynamics, when a system is maintained at a constant temperature *T* while experiencing unchanging hydrostatic pressure *p*, the equilibrium state minimizes the out-of-equilibrium Gibbs energy of the respective phase **[32]**.

$$G^*(p,V) = min_{x,V} G^*(x,V;p,T) \quad \text{(IV-44)}$$

Hence, the Gibbs function $G^*(V;\ p,\ T)$ can be minimized concerning the volume *V*, and this minimization is expressed as:

$$\frac{\partial G^*}{\partial V} = 0 = -p_{sta} + p + p_{th} \quad \text{(IV-45)}$$

Where:

- $p_{sta} = \frac{\partial E_{sta}}{\partial V}$ signifies the static pressure.
- $p_{th} = \frac{\partial F^*_{vib}}{\partial V}$ represents the thermal pressure.
- p is the externally applied pressure.

Solving equation (IV-45) provides the thermal equation of state (*EOS*).

The vibrational energy $F^*_{vib}(x,V;T)$ is given in the quasi-harmonic approximation in terms of the phonon density of states (or vibrational density of states) $g(\omega)$.

$$F^*_{vib}(x,V;T) = \int_0^{+\infty} \left[\frac{\omega}{2} + k_B T ln\left(1 - e^{-\omega/k_B T}\right)\right] g(\omega)\partial\omega \quad \text{(IV-46)}$$

The Debye model **[33]** is a commonly used approximation for the phonon spectrum, which simplifies the representation of phonons. This model treats the solid as an isotropic and continuous elastic medium, disregarding its discrete particle nature. In this medium, acoustic waves propagate without dispersion, and the frequencies are directly proportional to the wave vector. Instead of the *3n* phonon branches, the Debye model uses three acoustic branches, with frequencies following the relationship:

$\omega_D = Ck_D$. In this equation, C is the speed of sound in the given solid.

To ensure that the total number of vibration modes equals *3n*, a limited wave vector, k representing the radius of a sphere containing *n* wave vectors, is imposed. The phonons density of states is then described by a quadratic form:

$$g_{Debye} = \begin{cases} \frac{9n\omega^2}{\omega_D^3} & si \ \ \omega < \omega_D \\ 0 & si \ \ \omega \geq \omega_D \end{cases} \quad \text{(IV-47)}$$

Here, ω_D is the Debye frequency, which is closely tied to the Debye temperature:

$$\theta_D = \frac{\omega_D}{k_B} = \frac{1}{k_B}\left(\frac{6\pi^2 n}{V}\right)^{\frac{1}{3}}.V_0 \quad \text{(IV-48)}$$

In the quasi-harmonic Debye model, θ_D is dependent on volume, and the Grüneisen coefficient:

$$\gamma_D = -\frac{\partial ln\theta_D}{\partial lnV} \quad \text{(IV-49)}$$

When incorporating g_{Debye} into the quasi-harmonic expressions, the thermodynamic properties can be expressed as follows:

Gibbs free energy of Helmotz (*F*)

, $$F = E_{sta}(x,V) + \frac{9}{8}nk_B\theta_D + 3nk_BTln\left(1 - e^{-\theta_D/T}\right) - nk_BTD\left(\frac{\theta_D}{T}\right) \quad \text{(IV-50)}$$

Entropy (*S*)

$$S = -3nk_BTln\left(1 - e^{-\theta_D/T}\right) + 4nk_BD\left(\frac{\theta_D}{T}\right) \quad \text{(IV-51)}$$

Heat capacity at constant volume (C_V),

$$C_V = 12nk_BD\left(\frac{\theta_D}{T}\right) - \frac{9nk_B\theta_D/T}{e^{\theta_D/T-1}} \quad \text{(IV-52)}$$

B_T represents the isothermal compressibility modulus

$$B_T = -V\left(\frac{\partial p}{\partial V}\right)_T = V\left(\frac{\partial^2 F}{\partial V^2}\right)_T \quad \text{(IV-53)}$$

D represents the Debye integral

$$D(x) = \frac{3}{x^3}\int_0^x \frac{y^3 e^{-y}}{1-e^{-y}} dy \quad \text{(IV-54)}$$

Thermal expansion coefficient (α))

$$\alpha = -\frac{1}{V}\left(\frac{\partial V}{\partial T}\right)_P = \frac{\gamma_D C_V}{B_T V} \quad \text{(IV-55)}$$

Heat capacity at constant pressure (C_p),

$$C_p = \left(\frac{\partial H}{\partial T}\right)_p = C_V(1 + \gamma_D \alpha T) \quad \text{(IV-56)}$$

The static compressibility

$$B_s = -V\left(\frac{\partial p}{\partial V}\right)_s = V\left(\frac{\partial^2 U}{\partial V^2}\right)_s = B_T(1 + \gamma_D \alpha T) \quad \text{(IV-57)}$$

In the expressions above, *n* denotes the number of atoms per unit cell.

IV.7.2. Temperature and pressure effect

In this section, the thermodynamic properties are calculated as functions of pressure and temperature for the compounds K_2SnX_6 (X= Cl, Br, I), using the quasi-harmonic Debye model implemented in Gibbs2 program. This model relies on the input data $E(V)$ (total energy E and volume V of the primitive cell, obtained from the Wien2k code within the framework of the GGA approximation.

IV.7.2.1. Lattice volume and compressibility modulus.

The variation of the lattice volume with temperature at different pressures for the compounds K_2SnX_6 (X= Cl, Br, I) is illustrated in **Figure. IV. 21**. It is observed that the lattice volume slightly increases as the temperature rises at a given pressure. On the other hand, when the pressure increases, the volume decreases, meaning that the lattice volume decreases at a given temperature. Consequently, the rate of increase in lattice volume with temperature decreases with increasing pressure. Temperature cause expansion, and pressure suppress this effect.

The calculated values of the lattice volume for the K_2SnX_6 (X= Cl, Br, I) compounds at T=300 K and P=0 GPa are equal to 3459.61 Bohr³, 4137.31 Bohr³, and 5453.90 Bohr³, respectively.

The compressibility modulus is a property that defines the resistance to volume change when compressed. The evolution of the compressibility modulus as a function of temperature and pressure is shown in **Figure. IV. 22**.

In **Figure. IV. 22 (a)**, the compressibility modulus significantly decreases as the temperature rises. The effects of temperature on the compressibility modulus are evident at various pressure values. According to **Figure. IV. 22 (b),** it can be observed that the compressibility modulus increases almost linearly with pressure for all studied temperatures. The calculated values of the compressibility modulus at T = 300 K and P = 0 GPa for K_2SnCl_6, K_2SnBr_6 , and K_2SnI_6 are 30.30 GPa, 20.50 GPa, and 16.03 GPa, respectively.

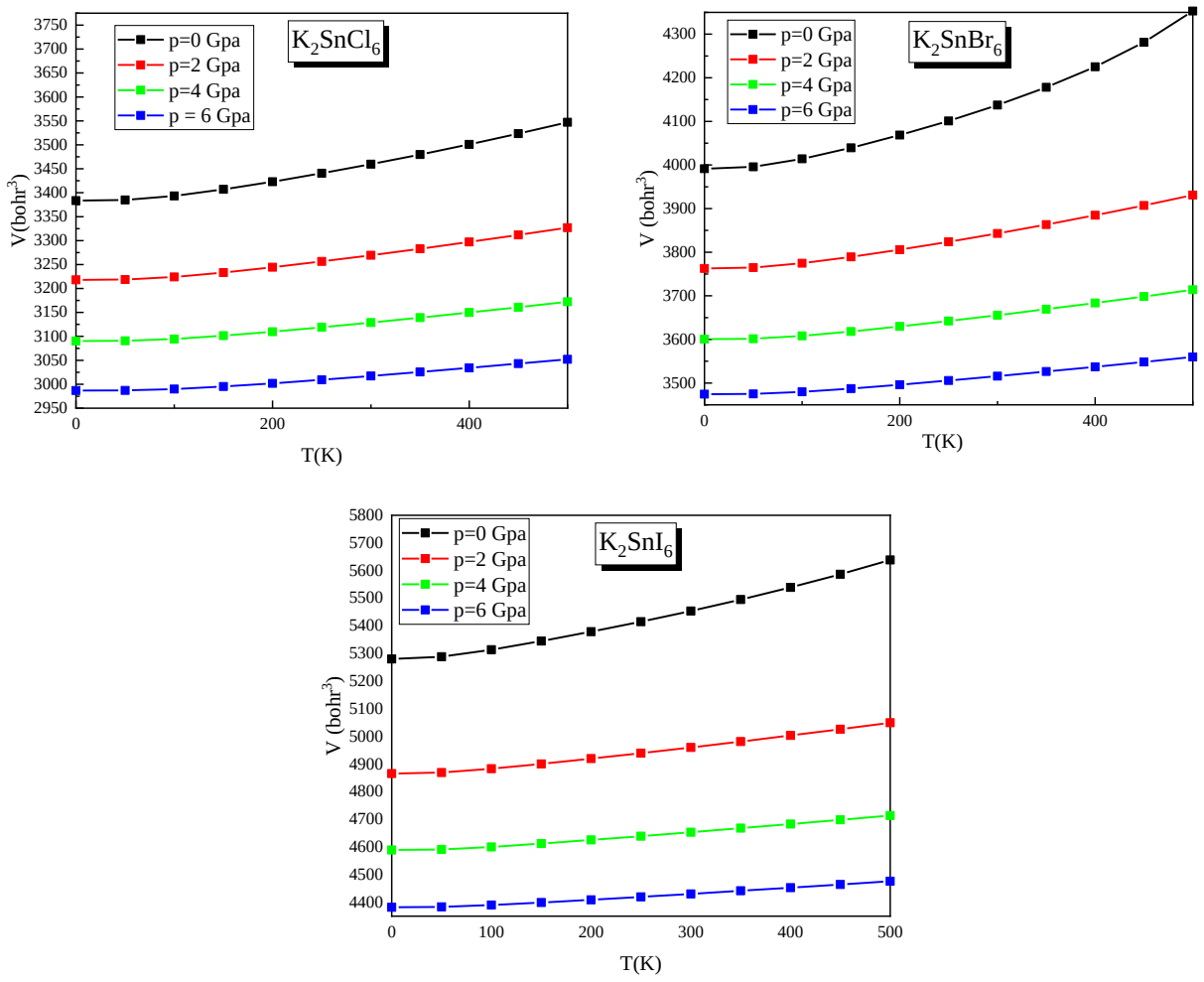

Figure. IV. 21: The lattice volume variation in terms of temperature at different pressures for K_2SnX_6 (X= Cl, Br, I) using GGA.

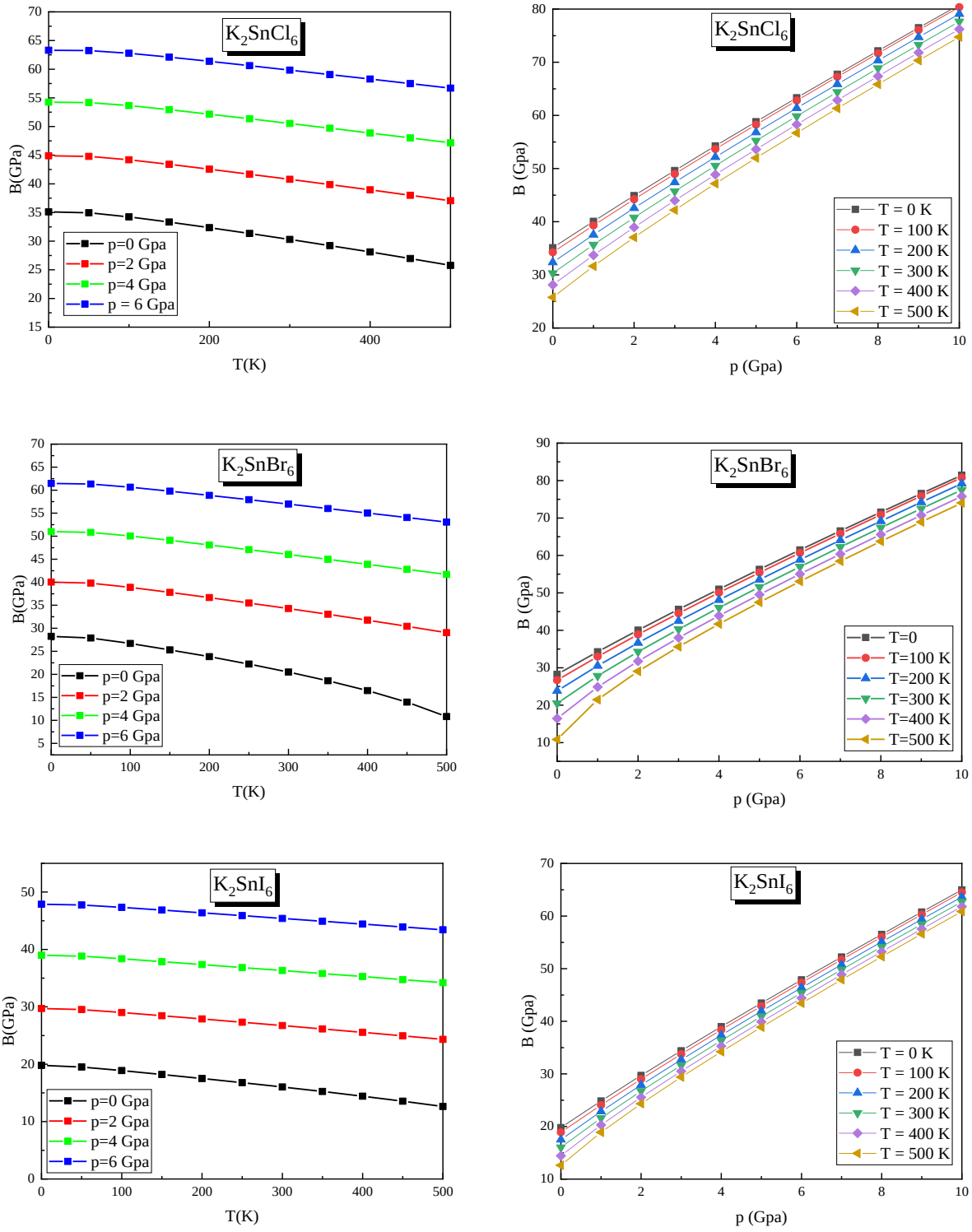

Figure. IV. 22: The compressibility modulus variation in terms of temperature (a) and pressure (b) for K_2SnX_6 (X= Cl, Br, I) using GGA.

IV.7.2.2. The thermal expansion coefficient α

The thermal expansion coefficient reflects the relationship between temperature and volume. **Figure. IV. 23** illustrates the variation of the thermal expansion coefficient as a function of temperature at different pressures for the compounds K_2SnX_6 (X= Cl, Br, I). According to this figure, at a given pressure, thermal expansion abruptly increases with temperature up to 200 K. from 200 K to 400 K, thermal expansion increases moderately with the increase of temperature. However, beyond T>400K thermal expansion rises rapidly because temperatures approaches the melting point (536 K for K_2SnCl_6 and 590 K for K_2SnBr_6). It is also noted that thermal expansion is sensitive to the increase in temperature at P = 0 GPa for all studied compounds. In the other hand, at a given temperature, the thermal expansion coefficient decreases with increasing pressure.

The calculated values of the thermal expansion coefficient for K_2SnX_6 (X= Cl, Br, I). compounds at T = 300 K and P = 0 GPa are 11.27 x 10^{-5} K^{-1}, 18.55 x 10^{-5} K^{-1}, and 14.63 x 10^{-5} K^{-1}, respectively.

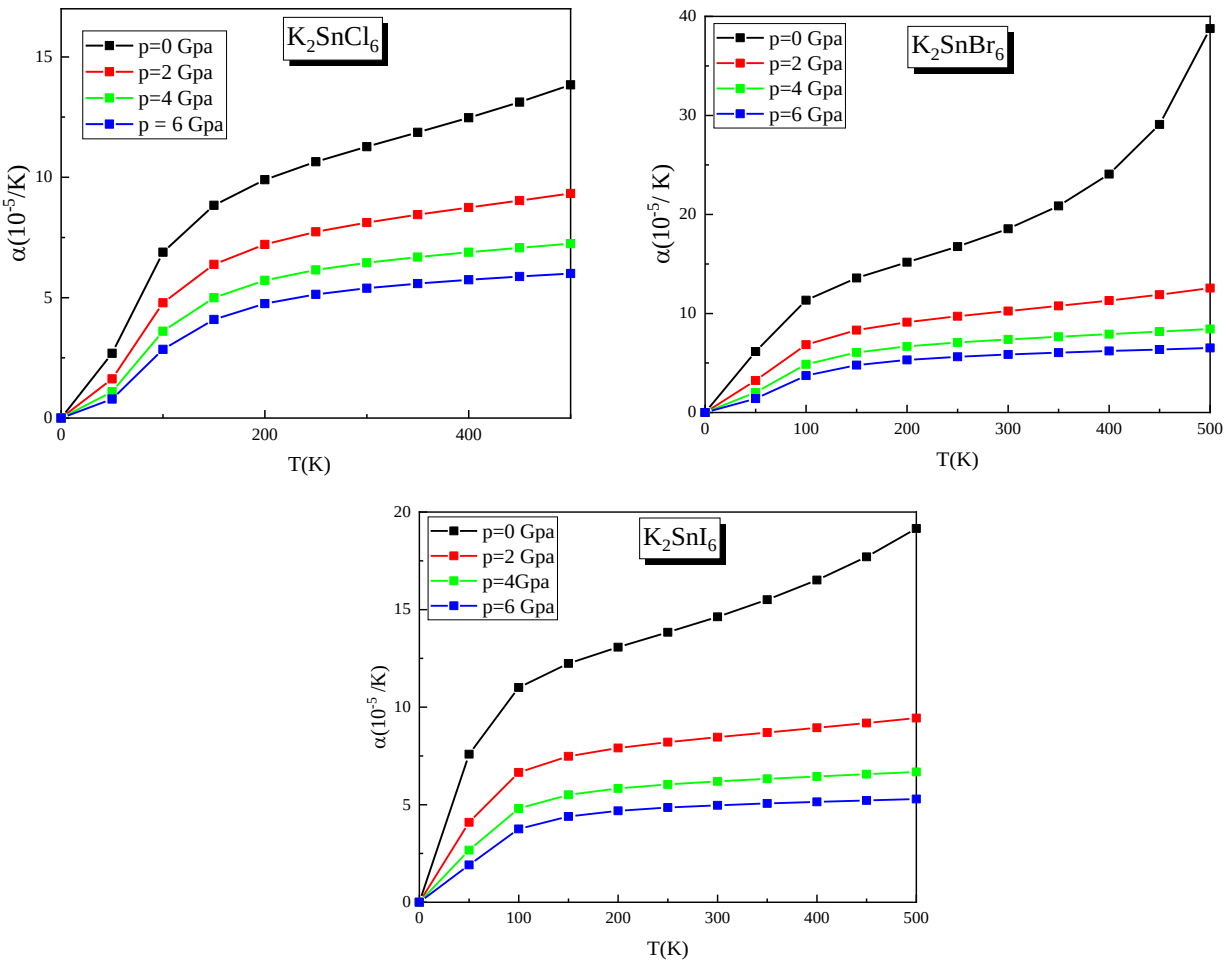

Figure. IV. 23: The coefficient of thermal expansion variation in terms of temperature at different pressures for K_2SnX_6 (X= Cl, Br, I) using GGA.

IV.7.2.3. Constant volume heat capacity (C_V) and constant pressure heat capacity (C_p)

The heat capacity of a substance provides essential insights into its vibrational properties and is a crucial parameter for many applications. It is one of the most important thermal properties. The evolution of the heat capacity at constant volume (C_V) with temperature at different pressures for the compound K_2SnX_6 (X= Cl, Br, I) is illustrated in **Figure. IV. 24**.

As the temperature increases, the values of the heat capacity increase rapidly at low temperatures and then increase slowly before getting constant at high temperatures. At high temperatures, the constant volume heat capacity C_V approaches the classical Dulong and Petit

limit. It is also observed that at a given temperature, the heat capacity decreases with the increase in applied pressure.

The calculated values of the constant volume heat capacity C_V at T = 300 K and P = 0 GPa for K_2SnCl_6, K_2SnBr_6, and K_2SnI_6 compounds are 429.42, 439.81, and 443.64 J $mol^{-1}K^{-1}$, respectively.

The variation of the heat capacity at constant pressure (C_P) with temperature for K_2SnX_6 (X= Cl, Br, I) is illustrated in **Figure. IV. 25**. This variation of C_P for the studied compounds exhibits similar characteristics. Increasing the temperature, the behavior of C_P values at lower temperatures is similar to that of C_V. However, in the high-temperature range, C_P increases with the temperature. At a given temperature, the value of C_P decreases with increasing pressure.

The calculated values of the constant pressure heat capacity CP at T = 300 K and P = 0 GPa for K_2SnCl_6, K_2SnBr_6, and K_2SnI_6 compounds are 465.07, 517.99, and 493.7408 J $mol^{-1}K^{-1}$, respectively.

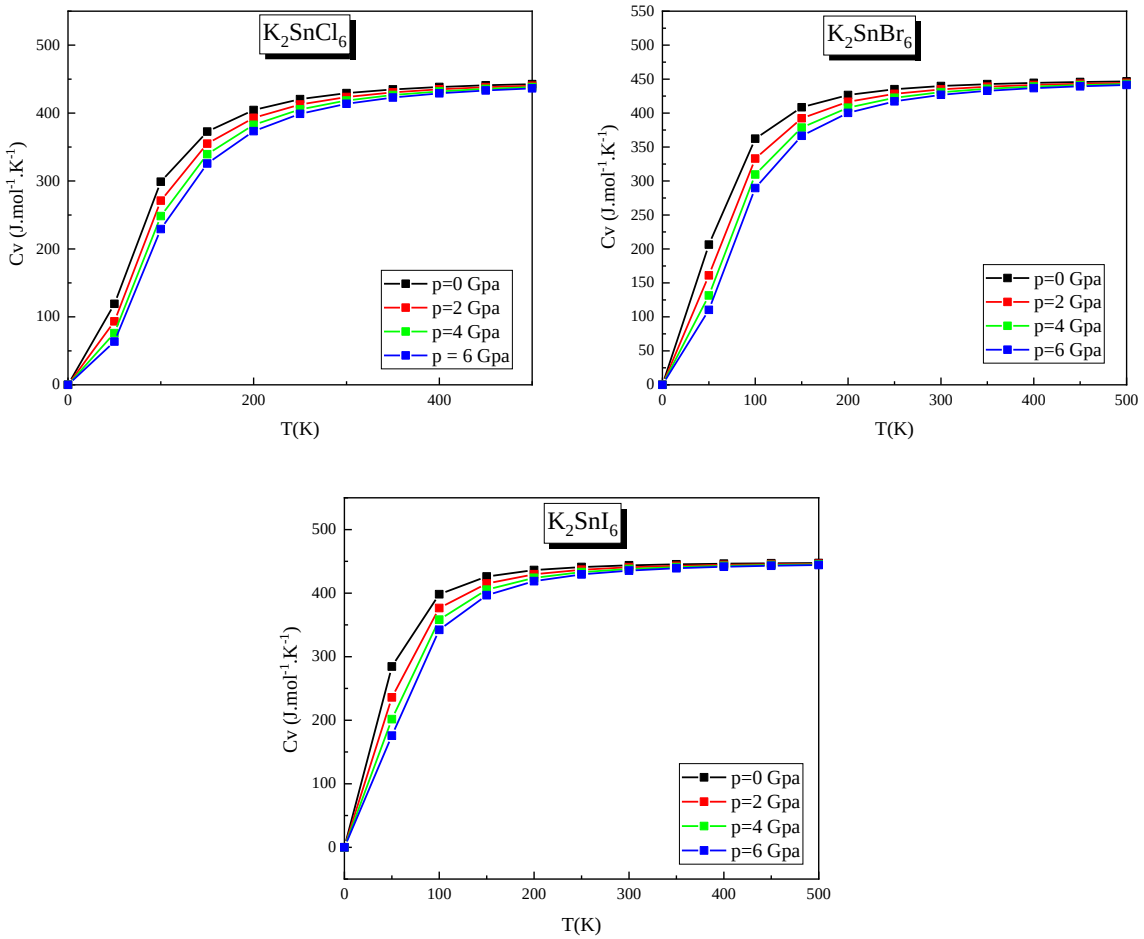

Figure. IV. 24 : The specific heat at constant volume variation in terms of temperature at different pressures for K_2SnX_6 (X= Cl, Br, I) using GGA.

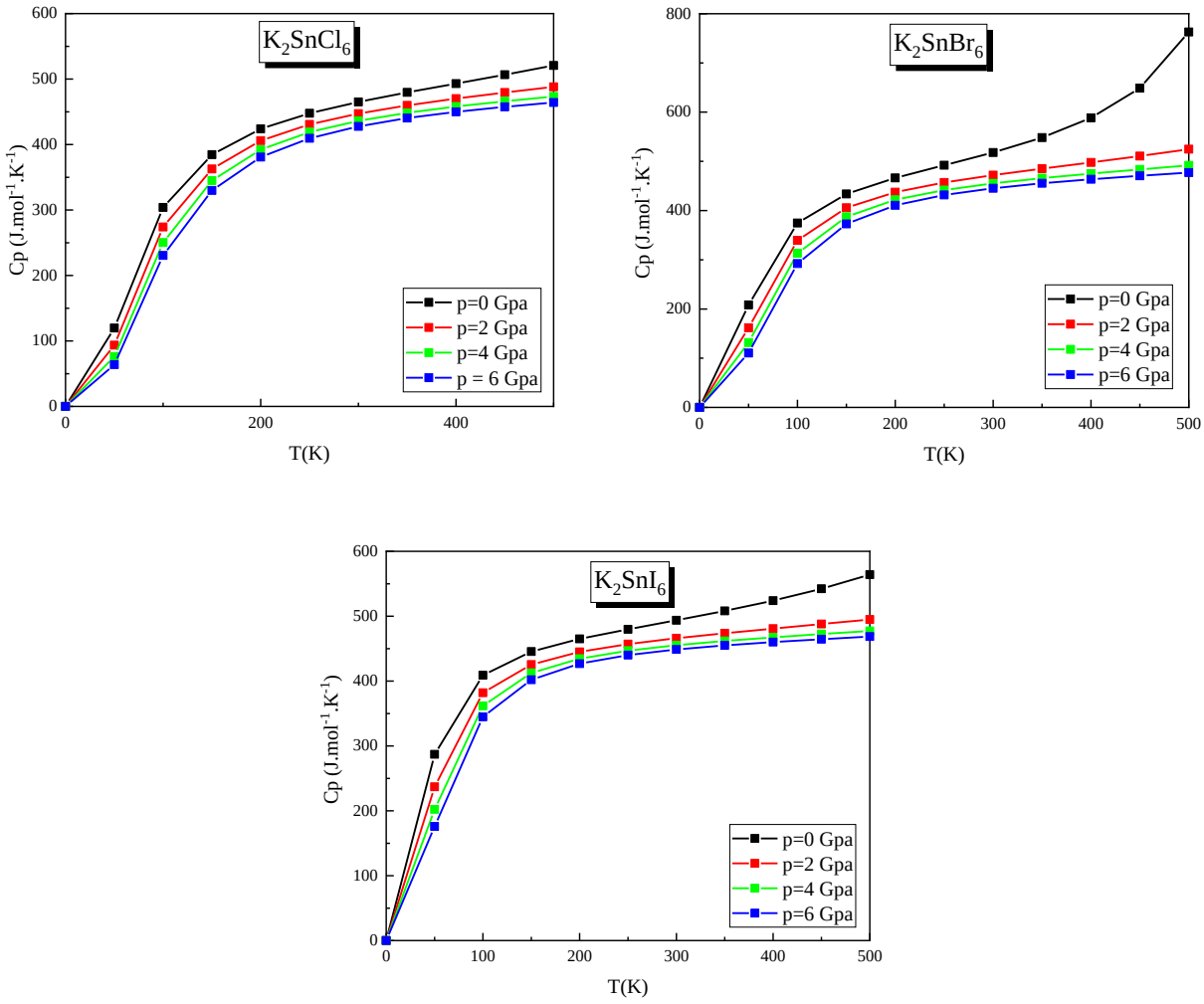

Figure. IV. 25: The specific heat at constant pressure variation in of temperature at different pressures for K_2SnX_6 (X= Cl, Br, I) using GGA.

IV.7.2.4. System entropy (S).

Designated by the symbol S on a microscopic scale, the entropy can be defined as a measure of the disorder of a system. The calculated results of entropy as a function of temperature at different pressures for the compounds K_2SnX_6 (X= Cl, Br, I) are illustrated in **Figure. IV. 26**. It is observed that the entropy increases almost linearly with the temperature and decreases when the pressure value increases. The calculated values of entropy at T = 300 K and P = 0 GPa for K_2SnCl_6, K_2SnBr_6, and K_2SnI_6 compounds are 632.33, 801.01, and 921.64 $J.mol^{-1}.K^{-1}$, respectively.

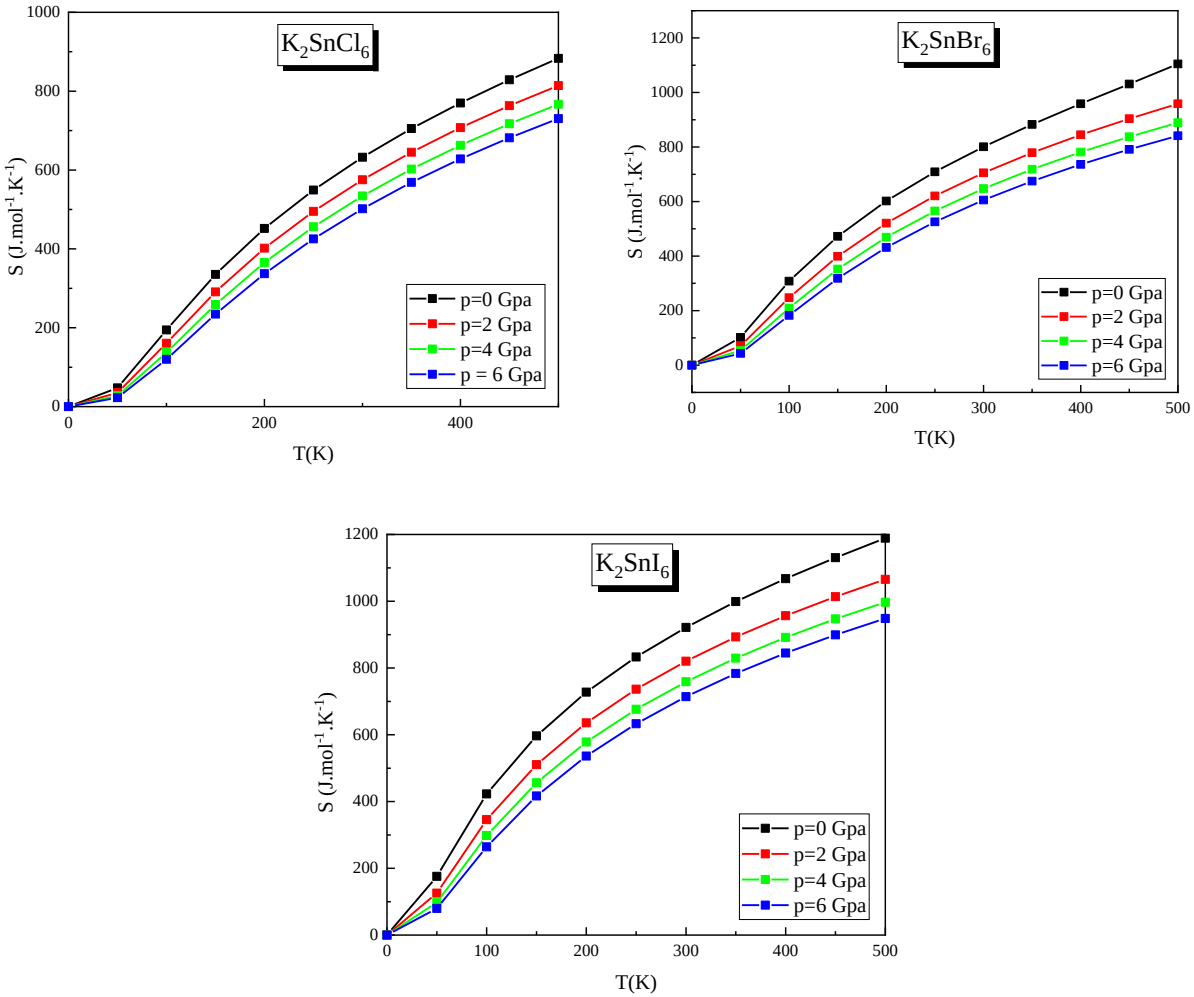

Figure. IV. 26 : The entropy variation in terms of temperature at different pressures for K_2SnX_6 (X= Cl, Br, I) using GGA.

IV.7.2.5. . Debye température (θ_D)

Debye temperature (θ_D) represents the temperature at which the highest normal mode of vibration occurs in a crystal. It establishes a connection between elastic properties and thermodynamic characteristics, including phonons, thermal expansion, thermal conductivity, specific heat, and lattice enthalpy.

The physical meaning of the Debye temperature is to distinguish between high and low frequencies. Beyond a certain limit frequency (towards low frequencies), quantum properties begin to influence. For frequencies higher than the limit frequency, physical properties are explained by classical theory. The Debye temperature is generally associated with the strength of chemical bonds and is proportional to the speed of sound, which increases with the hardness

of the material. The value of θ_D can vary significantly from one material to another, primarily depending on the type of bond. The more rigid the chemical bond, the higher the θ_D will be.

As indicated in **Figure. IV. 27 (a)**, the Debye temperature for for K_2SnX_6 (X= Cl, Br, I) compounds remains relatively stable in the range of 0 to 100 K and exhibits a linear decline as the temperature exceeds 100 K. It is also illustrated in **Figure. IV. 27 (b)**, that there is a linear ascent in the Debye temperature with increasing pressure, and at a given pressure, the Debye temperature decreases as the temperature rises. This behavior was observed in the evolution of the compressibility modulus as a function of temperature and pressure.

The computed Debye temperature values at T = 300 K and P = 0 GPa for the compounds K_2SnCl_6, K_2SnBr_6, and K_2SnI_6 are 284.54, 193.13, and 146.99 K, respectively.

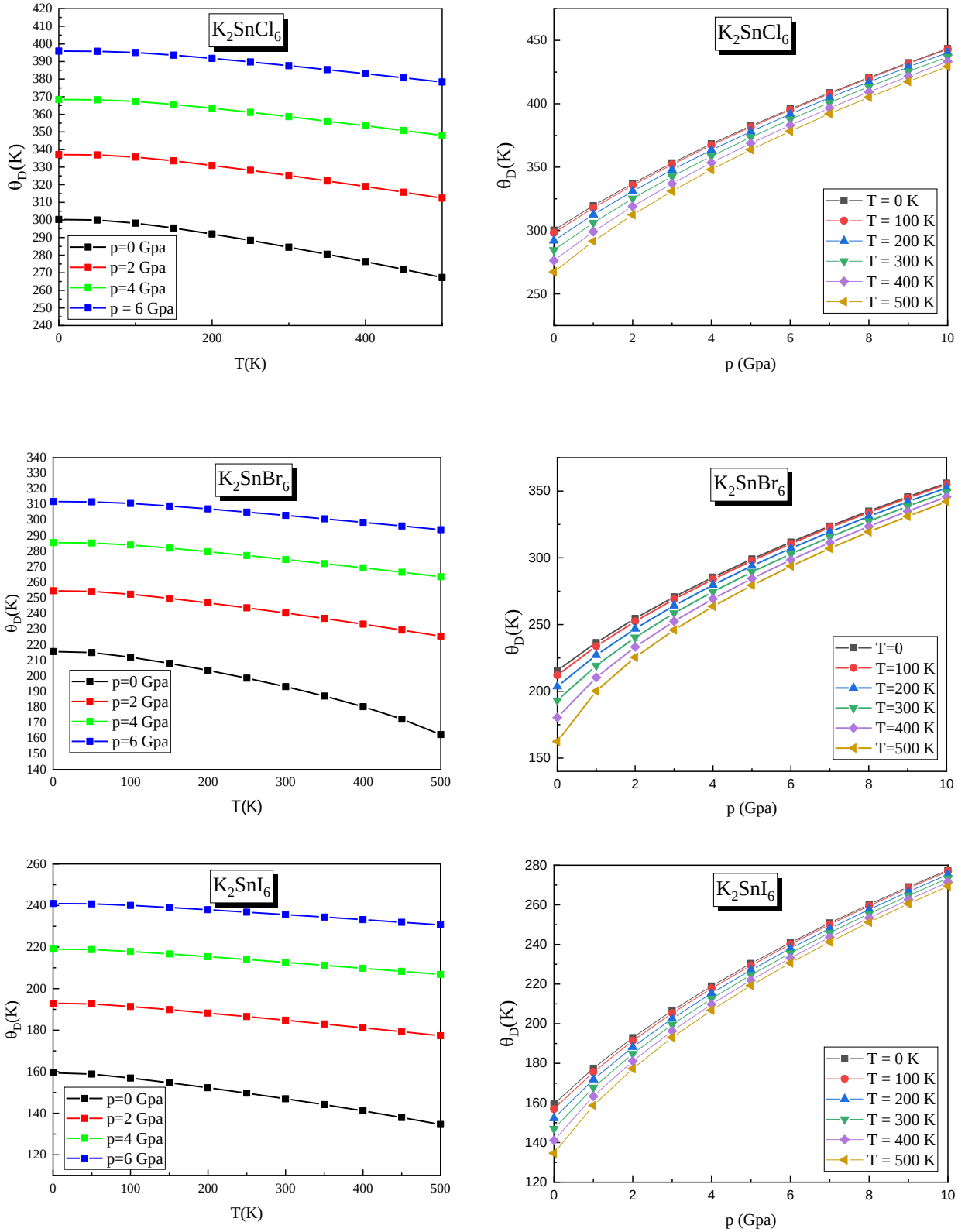

Figure. IV. 27: Debye temperature variation in terms of temperature (a) and pressure (b) for K_2SnX_6 (X= Cl, Br, I) using GGA.

References

[1] K. Schwarz, P. Blaha, and G. K. H. Madsen, "Electronic structure calculations of solids using the WIEN2k package for material sciences," *Computer Physics Communications*, vol. 147, no. 1–2, pp. 71–76, Aug. 2002, doi: 10.1016/S0010-4655(02)00206-0.

[2] J. P. Perdew, K. Burke, and M. Ernzerhof, "Generalized Gradient Approximation Made Simple," *Phys. Rev. Lett.*, vol. 77, no. 18, pp. 3865–3868, Oct. 1996, doi: 10.1103/PhysRevLett.77.3865.

[3] J. P. Perdew *et al.*, "Restoring the Density-Gradient Expansion for Exchange in Solids and Surfaces," *Phys. Rev. Lett.*, vol. 100, no. 13, p. 136406, Apr. 2008, doi: 10.1103/PhysRevLett.100.136406.

[4] A. D. Becke and E. R. Johnson, "A simple effective potential for exchange," *The Journal of Chemical Physics*, vol. 124, no. 22, p. 221101, Jun. 2006, doi: 10.1063/1.2213970.

[5] G. K. H. Madsen and D. J. Singh, "BoltzTraP. A code for calculating band-structure dependent quantities," *Computer Physics Communications*, vol. 175, no. 1, pp. 67–71, Jul. 2006, doi: 10.1016/j.cpc.2006.03.007.

[6] T. Higashi, S. Syoyama, and K. Osaki, "Structure of potassium hexabromostannate(IV) at room temperature," *Acta Crystallogr B Struct Sci*, vol. 35, no. 1, pp. 144–146, Jan. 1979, doi: 10.1107/S0567740879002776.

[7] H. Boysen and A. W. Hewat, "A neutron powder investigation of the structural changes in K_2SnCl_6," *Acta Crystallogr B Struct Sci*, vol. 34, no. 5, pp. 1412–1418, May 1978, doi: 10.1107/S0567740878005816.

[8] F. D. Murnaghan, "The Compressibility of Media under Extreme Pressures," *Proc. Natl. Acad. Sci. U.S.A.*, vol. 30, no. 9, pp. 244–247, Sep. 1944, doi: 10.1073/pnas.30.9.244.

[9] U.-G. Jong, C.-J. Yu, and Y.-H. Kye, "Computational prediction of structural, electronic, and optical properties and phase stability of double perovskites K_2SnX_6 (X = I, Br, Cl)," *RSC Adv.*, vol. 10, no. 1, pp. 201–209, 2020, doi: 10.1039/C9RA09232C.

[10] M. Fox, *Optical properties of solids*, 2 ed., (With corr.). in Oxford master series in physics Condensed matter physics, no. 3. Oxford: Oxford Univ. Press, 2012.

[11] B. P. Rand, J. Genoe, P. Heremans, and J. Poortmans, "Solar cells utilizing small molecular weight organic semiconductors," *Progress in Photovoltaics*, vol. 15, no. 8, pp. 659–676, Dec. 2007, doi: 10.1002/pip.788.

[12] C. Cohen-Tannoudji, B. Diu, and F. Laloë, Mécanique quantique. *in Collection Enseignement des sciences*, no. 16. Paris: Hermann, 1973.

[13] R. Khenata, A. Bouhemadou, M. Sahnoun, Ali. H. Reshak, H. Baltache, and M. Rabah, "Elastic, electronic and optical properties of ZnS, ZnSe and ZnTe under pressure," *Computational Materials Science*, vol. 38, no. 1, pp. 29–38, Nov. 2006, doi: 10.1016/j.commatsci.2006.01.013.

[14] J. L. Erskine and E. A. Stern, "Calculation of the M 23 magneto-optical absorption spectrum of ferromagnetic nickel," *Phys. Rev. B*, vol. 12, no. 11, pp. 5016–5024, Dec. 1975, doi: 10.1103/PhysRevB.12.5016.

[15] G. Murtaza, B. Amin, S. Arif, M. Maqbool, I. Ahmad, A. Afaq, S. Nazir, M. Imran, M. Haneef, "Structural, electronic and optical properties of CaxCd1−xO and its conversion from semimetal to wide bandgap semiconductor," *Computational Materials Science*, vol. 58, pp. 71–76, Jun. 2012, doi: 10.1016/j.commatsci.2012.01.020.

[16] Yanzhong Pei , Aaron D. LaLonde , Nicholas A. Heinz , Xiaoya Shi , Shiho Iwanaga , Heng Wang , Lidong Chen , and G. Jeffrey Snyder, "Stabilizing the Optimal Carrier Concentration for High Thermoelectric Efficiency," *Advanced Materials*, vol. 23, no. 47, pp. 5674–5678, Dec. 2011, doi: 10.1002/adma.201103153.

[17] Kanishka Biswas, Jiaqing He, Ivan D. Blum , Chun-I Wu, Timothy P. Hogan, David N. Seidman, Vinayak P. Dravid & Mercouri G. Kanatzidis, "High-performance bulk thermoelectrics with all-scale hierarchical architectures," *Nature*, vol. 489, no. 7416, pp. 414–418, Sep. 2012, doi: 10.1038/nature11439.

[18] B. M. Askerov, *Electron Transport Phenomena in Semiconductors*. WORLD SCIENTIFIC, 1994. doi: 10.1142/1926.

[19] C. Hamaguchi, *Basic semiconductor physics*, 2. ed. Berlin Heidelberg: Springer, 2010.

[20] M. Kaviany, *Heat Transfer Physics*, 2nd ed. Cambridge University Press, 2014. doi: 10.1017/CBO9781107300828.

[21] G. K. H. Madsen, "Automated Search for New Thermoelectric Materials: The Case of LiZnSb," *J. Am. Chem. Soc.*, vol. 128, no. 37, pp. 12140–12146, Sep. 2006, doi: 10.1021/ja062526a.

[22] C. L. Julian, "Theory of Heat Conduction in Rare-Gas Crystals," *Phys. Rev.*, vol. 137, no. 1A, pp. A128–A137, Jan. 1965, doi: 10.1103/PhysRev.137.A128.

[23] G. A. Slack, "Nonmetallic crystals with high thermal conductivity," *Journal of Physics and Chemistry of Solids*, vol. 34, no. 2, pp. 321–335, Jan. 1973, doi: 10.1016/0022-3697(73)90092-9.

[24] A. Otero-de-la-Roza and V. Luaña, "Gibbs2: A new version of the quasi-harmonic model code. I. Robust treatment of the static data," *Computer Physics Communications*, vol. 182, no. 8, pp. 1708–1720, Aug. 2011, doi: 10.1016/j.cpc.2011.04.016.

[25] A. Otero-de-la-Roza, D. Abbasi-Pérez, and V. Luaña, "Gibbs2: A new version of the quasiharmonic model code. II. Models for solid-state thermodynamics, features and implementation," *Computer Physics Communications*, vol. 182, no. 10, pp. 2232–2248, Oct. 2011, doi: 10.1016/j.cpc.2011.05.009.

[26] Q. Mahmood, T. Ghrib, A. Rached, A. Laref, and M. A. Kamran, "Probing of mechanical, optical and thermoelectric characteristics of double perovskites Cs2GeCl/Br6 by DFT method," *Materials Science in Semiconductor Processing*, vol. 112, p. 105009, Jun. 2020, doi: 10.1016/j.mssp.2020.105009.

[27] Muniba Huma, Muhammad Rashid, Q. Mahmood, Eman Algrafy , Nessrin A. Kattan , A. Laref , A.S. Bhatti., "Physical properties of lead-free double perovskites A2SnI6 (A= Cs, Rb) using ab-initio calculations for solar cell applications," *Materials Science in Semiconductor Processing*, vol. 121, p. 105313, Jan. 2021, doi: 10.1016/j.mssp.2020.105313.

[28] R. Ullah, M. A. Ali, G. Murtaza, A. Khan, and A. Mahmood, "Ab initio study for the structural, electronic, magnetic, optical, and thermoelectric properties of K_2OsX_6 (X = Cl, Br) compounds," *Int J Energy Res*, vol. 44, no. 11, pp. 9035–9049, Sep. 2020, doi: 10.1002/er.5613.

[29] R. Ullah, M. A. Ali, G. Murtaza, A. Mahmood, and S. M. Ramay, "The significance of anti-fluorite Cs_2NBI_6 via its structural, electronic, magnetic, optical and thermoelectric properties," *Int J Energy Res*, vol. 44, no. 13, pp. 10179–10191, Oct. 2020, doi: 10.1002/er.5638.

[30] M. A. Blanco, E. Francisco, and V. Luaña, "GIBBS: isothermal-isobaric thermodynamics of solids from energy curves using a quasi-harmonic Debye model," *Computer Physics Communications*, vol. 158, no. 1, pp. 57–72, Mar. 2004, doi: 10.1016/j.comphy.2003.12.001.

[31] A. Otero-de-la-Roza and V. Luaña, "Gibbs2: A new version of the quasi-harmonic model code. I. Robust treatment of the static data," *Computer Physics Communications*, vol. 182, no. 8, pp. 1708–1720, Aug. 2011, doi: 10.1016/j.cpc.2011.04.016.

[32] A. A. Maradudin, Ed., *Theory of lattice dynamics in the harmonic approximation*, 2. ed. in Solid state physics Supplement, no. 3. New York, NY: Acad. Press, 1971.

[33] L. A. Girifalco, *Statistical mechanics of solids*. Oxford: Oxford University Press, 2003.

[34] B. N. BRAHMI, Doctorat thesis, Universite Abou Bakr Belkaid – Tlemcen ,2013.

[35] G. Leibfried, E. Schl¨omann, Nachr. Akad. Wiss. Göttingen II a(4), 71, 1954.

[36] R. Berman, *Thermal Conduction in Solids*, Clarendon Press, Oxford, 1976.

[37] B. R. Nag, *Electron Transport in Compound Semiconductors*, Springer Verlag, Berlin, 1980, doi: 10.1007/978-3-642-81416-7.

[38] T.J. Scheidemantel, C. Ambrosch-Draxl, T. Thonhauser, J.V. Badding, J.O. Sofo, Transport coefficients from first-principles calculations, *Phys. Rev. B* 68, 2003, doi: 10.1103/PhysRevB.68.125210.

[39] L. Jodin, J. Tobola, P. P echeur, H. Scherrer and S. Kaprzyk, Effect of substitutions and defects in half-Heusler FeVSb studied by electron transport measurements and KKR-CPA electronic structure calculations, *Phys. Rev. B*,70, (2004) 184207.

[40] K. P. Ong, D. J. Singh and P. Wu, Analysis of the thermoelectric properties of n-type ZnO, *Phys. Rev. B*, 83, 2011, doi.org/10.1103/PhysRevB.83.115110

[41] D. Parker and D. J. Singh, High-temperature thermoelectric performance of heavily doped PbSe, *Phys. Rev. B*, 82, 2010, 10.1103/PhysRevB.82.035204.

[42] L. Chaput, P. Pecheur, J. Tobola and H. Scherrer, Transport in doped skutterudites: Ab initio electronic structure calculations, *Phys. Rev. B*, 72, (2005) 085126.
doi: 10.1103/PhysRevB.72.085126

[43] Y. Zhou, J. Wang, D. Luo, D. Hu, Y. Min, and Q. Xue, "Recent progress of halide perovskites for thermoelectric application," *Nano Energy*, vol. 94, p. 106949, Apr. 2022, doi: 10.1016/j.nanoen.2022.106949.

[44] Ambrosch-Draxl, C., Soto, J.O., 2006. Linear optical properties of solids within the full-potential linearized augmented planewave method. *Comput. Phys. Commun*. 175, 1–14, doi: 10.1016/j.cpc.2006.03.005

[45] M. Azadparvar, H.A. Rahnamaye Aliabad, E. Rezaei-Seresht, M. Mirzaei, "Effect of fluorine substitution on the photobiological and electronic properties of resveratrol crystal structure: A first- principles study", *Journal of Photochemistry & Photobiology, A: Chemistry*, pp. 429, Mar.2022, doi: 10.1016/j.jphotochem.2022.113941.

[46] F. Goubin, Doctorat thesis. Université de Nantes, 2003.

General conclusion

General conclusion

This research endeavors to comprehensively investigate the structural, optoelectronic, thermoelectric, and thermodynamic attributes of potassium tin halide vacancy-ordered double perovskites, specifically focusing on K_2SnX_6, where X represents chlorine (Cl), bromine (Br), and iodine (I), employing advanced first-principles computations. The study delves into various facets of these materials in their monoclinic phase, utilizing density functional theory (DFT) and Boltzmann transport theory implemented in the wien2k code.

Concerning electronic properties, the computed band gaps, employing the modified Becke-Johnson (mBJ) potential, exhibit a discernible ascending pattern: 1.707 eV for K_2SnI_6, 2.581 eV for K_2SnBr_6, and 4.126 eV for K_2SnCl_6. These band gap values hold particular significance for future research due to their alignment with theoretical predictions. In addition, it is worth noting that all the compounds under investigation demonstrate direct band gaps except for K_2SnI_6 which shows an indirect band gap.

This study evaluates the optical properties of K_2SnX_6 (X = Cl, Br, I) vacancy-ordered double perovskites. The results show an almost isotropic behaviour. Furthermore, the investigation of the compounds' optical characteristics reveals that the calculated optical band gaps align with the theoretically computed values obtained from the band structure computations. Additionnally, a notable absorptive activity is demonstrated, particularly in K_2SnI_6 and K_2SnBr_6, which exhibit higher imaginary part of dielectric function in the visible spectrum due to their narrower bandgap. This fact renders them more appropriate for utilisation in solar cell technologies as compared to K_2SnCl_6. Whereas, all investigated compounds in the current study exhibit a low level of reflection.

Turning to an analysis of thermoelectric qualities, substituting iodine with either bromine or chlorine induces the formation of wider band gaps. Electrical Conductivity increases with temperature due to rising carrier concentration, with K_2SnI_6 showing lower conductivity above 200 K due to higher ion scattering. conductivity. The thermal conductivity resulting from phonons

witnesses a decline with increasing temperature, signifying a reduction in heat transport by phonons. The confirmation of p-type conductivity is evident from the positive sign of the Seebeck coefficient. Furthermore, the Power Factor shows a positive correlation with temperature, with values approaching 3×10^{-3} W/mK^2 for K_2SnCl_6 and K_2SnBr_6, and 1.5×10^{-3} W/mK^2 for K_2SnI_6 at 500 K. At this temperature, the compounds exhibit peak values of the figure of merit (ZT) at 0.58, 0.69, and 0.65 for K_2SnCl_6, K_2SnBr_6, and K_2SnI_6, respectively. These detailed findings underscore the potential utility of these compounds as highly efficacious materials for various thermoelectric applications, offering a wealth of opportunities for further exploration and application in sustainable energy technologies.

The investigation of thermodynamic properties in K_2SnX_6 (X= Cl, Br, I) compounds reveals nuanced effects of temperature and pressure. Lattice volume responds to opposing influences of temperature-induced expansion and pressure-induced contraction. The compressibility modulus decreases with temperature but increases linearly with pressure. Thermal expansion coefficient shows a nonlinear increase with temperature. Both constant volume heat capacity (Cv) and constant pressure heat capacity (Cp) increase with temperature but decrease with pressure. The Debye temperature (θ_D) remains stable at low temperatures, decreasing linearly as temperature exceeds 100 K, while increasing almost linearly with pressure. These findings contribute to a comprehensive understanding of thermodynamic behavior, providing insights for further research and potential industrial applications.